ISSN 1590-8844
Vol. 06 No 02
2005

International Journal of Mechanics and Control

Honorary Editor: Guido Belforte

Editor: Andrea Manuello Bertetto

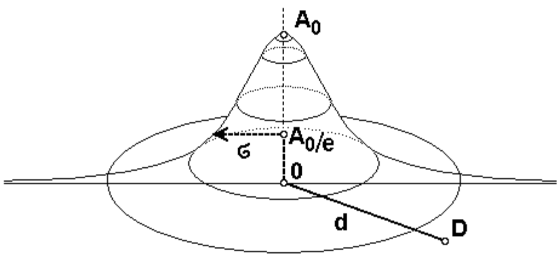

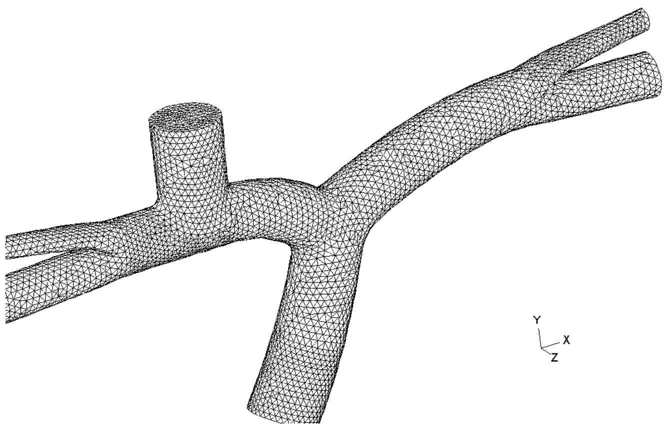

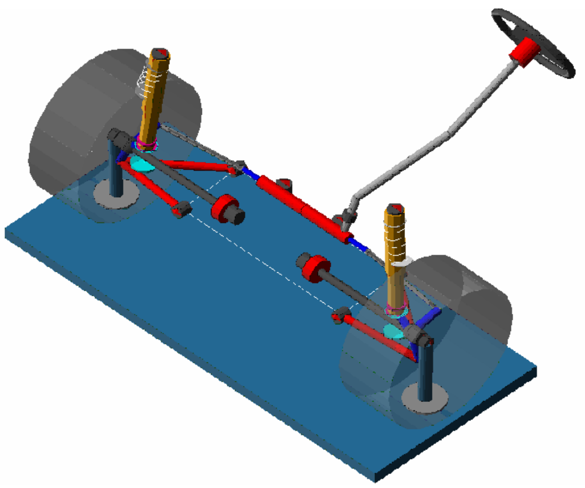

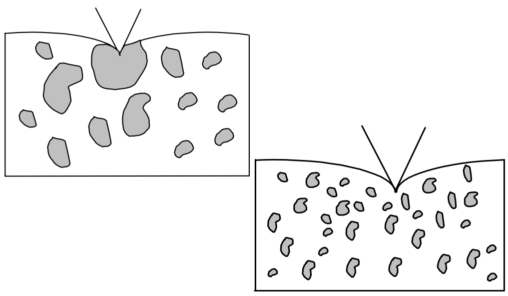

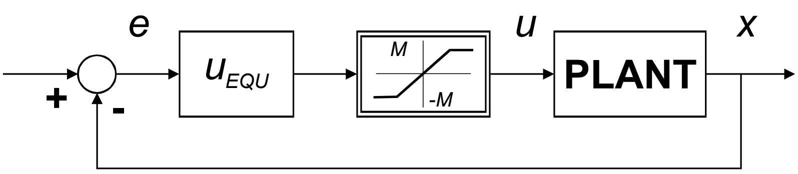

LIBRERIA EDITRICE UNIVERSITARIA
LEVROTTO & BELLA
TORINO

Editorial Board of the

International Journal of Mechanics and Control

Published by Levrotto&Bella – Torino – Italy E.C.

Honorary editor: **Guido Belforte**
Editor: **Andrea Manuello Bertetto**
General Secretariat: **Elvio Bonisoli**

Anindya Ghoshal
Arizona State University
Tempe – Arizona - USA

Domenico Appendino
Doctor Engineer
Marketing Director
Prima Industrie
Torino – Italy

Kenji Araki
Saitama University
Shimo Okubo, Urawa
Saitama – Japan

Bruno A. Boley
Columbia University,
New York - USA

Amalia Ercoli Finzi
Technical University - Politecnico di Milano
Milano – Italy

Carlo Ferraresi
Technical University - Politecnico di Torino
Torino – Italy

Nunziatino Gualtieri
Space System Group
Alenia Spazio
Torino – Italy

Giovanni Jacazio
Technical University - Politecnico di Torino
Torino – Italy

Andrea Manuello Bertetto
University of Cagliari
Cagliari – Italy

Stamos Papastergiou
Doctor
Group Leader Chief Engineer's Unit
Jet Joint Undertaking
Abingdon – United Kingdom

Mihailo Ristic
Doctor
Senior Lecturer
Imperial College
London – United Kingdom

Jànos Somlò
Technical University of Budapast
Budapest – Ungary

Jozef Suchy
Faculty of Natural Science
Banska Bystrica - Slovakia

Lubomir Uher
Institute of Control Theory and Robotics
Bratislava – Slovakia

Furio Vatta
Technical University - Politecnico di Torino
Torino – Italy

Kazuo Yamafuji
University of Electro-Communications
Tokyo – Japan

Official Torino Italy Court Registration
n.5390, 5th May 2000

Deposito presso il Tribunale di Torino
numero 5390 del 5 maggio 2000
Direttore responsabile:
Andrea Manuello Bertetto

International Journal of Mechanics and Control

Editor: **Andrea Manuello Bertetto**

Honorary editor: **Guido Belforte** ***General Secretariat:*** **Elvio Bonisoli**

The Journal is addressed to scientists and engineers who work in the fields of mechanics (mechanics, machines, systems, control, structures). It is edited in Turin (Northern Italy) by Levrotto&Bella Co., with an international board of editors. It will have not advertising.
Turin has a great and long tradition in mechanics and automation of mechanical systems. The journal would will to satisfy the needs of young research workers of having their work published on a qualified paper in a short time, and of the public need to read the results of researches as fast as possible.
Interested parties will be University Departments, Private or Public Research Centres, Innovative Industries.

Aims and scope

The *International Journal of Mechanics and Control* publishes as rapidly as possible manuscripts of high standards. It aims at providing a fast means of exchange of ideas among workers in Mechanics, at offering an effective method of bringing new results quickly to the public and at establishing an informal vehicle for the discussion of ideas that may still in the formative stages.

Language: English

International Journal of Mechanics and Control will publish both scientific and applied contributions. The scope of the journal includes theoretical and computational methods, their applications and experimental procedures used to validate the theoretical foundations. The research reported in the journal will address the issues of new formulations, solution, algorithms, computational efficiency, analytical and computational kinematics synthesis, system dynamics, structures, flexibility effects, control, optimisation, real-time simulation, reliability and durability. Fields such as vehicle dynamics, aerospace technology, robotics and mechatronics, machine dynamics, crashworthiness, biomechanics, computer graphics, or system identification are also covered by the journal.

Please address contributions to

Prof. Guido Belforte
Prof. Andrea Manuello Bertetto
PhD Eng. Elvio Bonisoli

Dept. of Mechanics
Technical University - Politecnico di Torino
C.so Duca degli Abruzzi, 24.
10129 - Torino - Italy - E.C.

e_mail: jomac@polito.it

Subscription information

Subscription order must be sent to
the publisher:

Libreria Editrice Universitaria
Levrotto&Bella
2/E via Pigafetta – 10129 Torino – Italy

www.levrotto-bella.net
e_mail: info@levrotto-bella.net
tel. +39.011.5097367
+39.011.5083690
fax +39.011.504025

ISSN 1590-8844
International Journal of Mechanics and Control, Vol. 06, No. 02, 2005

DATA FUSION FROM CCD CAMERA AND ULTRASOUND SCANNING LOCATOR

Danica Janglová, Ivan Kello, Ivo Považan, Lubomír Uher, Svatopluk Vagner

Institute of Informatics, Slovak Academy of Sciences, Bratislava, Slovak republic

ABSTRACT

The method of data fusion was developed applicable to an autonomous mobile robot moving in a known or partially known environment. The evaluation of data from ultrasound range finder and CCD camera, which is always sparse, requires a fusion of the data acquired from both sources. More complex information is unified in the Map in the resulting invariant rectangular representation. The information from ultrasound range finder is more reliable and therefore it is used as basis information. The data from CCD images is matched to previous data giving rise to more complex invariant Map. In a case of known environment the Map is a'priori known and recognition of object should be a result of the whole process.

Keywords: Ultrasound range finder, CCD camera, Cluster analysis, Matching problem

1 INTRODUCTION

In autonomous mobile vehicle (amv) one of crucial tasks is updating a map of environment in accordance with the recent data acquired from a CCD camera. In our case we decided to integrate information from a CCD camera with depth information obtained from ultrasound overview range finder (rf). The obstacles as seen by the camera are identified with objects reached by ultrasound rf The limited maximum reach of ultrasound rf serves for advantage in this case, as it can serve for discrimination criterion for distinguishing between close and distant objects. Both the information from CCD camera and from rf are integrated together to serve for environment map updating. Of course, the positions of objects obtained from camera snap evaluation must be preprocessed using transformation of eikonal equations [1] from spherical to rectangular Euclidean representation of the Map, and the data acquired by the rf are transformed from polar to the rectangular coordinates. At the given time instant the both data must obey the scaling conditions in order to obtain the representations of the objects in a same map scale.

Contact author: Danica Janglová

Institute of Informatics Slovak Academy of Science,
Dúbravská cesta 9, 842 37 Bratislava, Slovakia
E-mail: utrrjang@savba.sk

For calibration purposes we used some known objects in preprocessing step and the results of calibration are applied to data in transformation steps.

2 THE PROPOSED ALGORITHM

The whole process of data fusion runs according to the scheme depicted in the Figure 1 and it use these assumptions:

- All sensor data is supposed to be sparse data.
- The raw data is first transformed into an invariant frame of reference.
- Then calibration unifies the scales for different sensors aiming the data represented in a common unified scale.
- Data from each sensor is written into its own set. The set U and set V are the labels for ultrasound and camera data respectively.
- Cross-matching data from different sources U and V enables more reliable identification of objects comparing their positions from different data sources.
- In a known environment all acquired data is attached to known objects any case confirming or denying the hypothesis of a most probable object's identity with some of the object on the Map of environment.
- In an unknown environment only the mutual matching of the data acquired from all accessible sensors is possible, also confirming or denying the hypothesis of identity of a but randomly chosen object. The more reliable information from ultrasound range finder is

used as primary information and the data from CCD images is matched to previous data giving rise to more complex invariant Map. At first sight it is obvious, that the matching problem is sick posed problem in the later case giving no unambiguous solution to the object recognition in general.

- The recognition of closest-to-amv objects should be a result of the whole process.

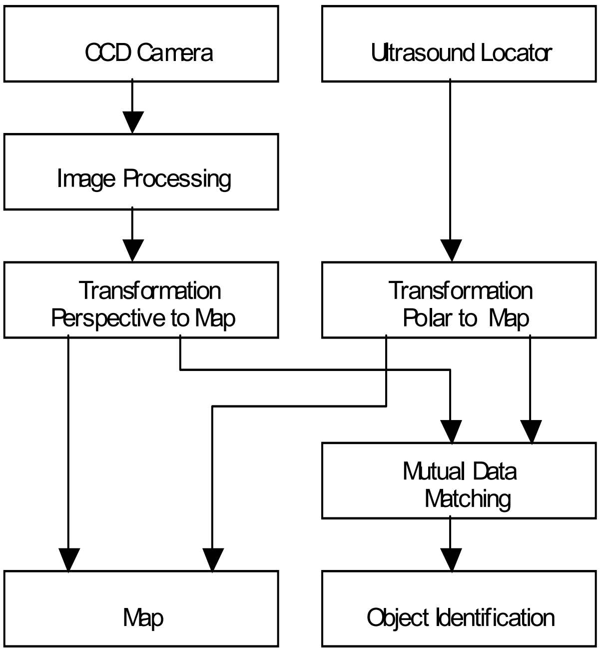

Figure 1 Block scheme of the algorithm.

3 THE ALGORITHM OF DATA FUSION

3.1 TRANSFORMATION OF RANGE FINDER DATA

There are two different problems to be solved: The rf operates as overview radar, i.e. its antenna rotates stepwise in a horizontal plane by constant angular increments $\Delta\alpha$ of azimuth α. For every azimuth value α the measurement of all distances of the obstacles situated along the direction α is performed. Up to 16 obstacles may be recorded in one measurement. The corresponding data is recorded as a packet. The azimuth values span from -170 to +170 angular degrees, the leaved 20 degrees of a blind space serve for fixation purposes of the origin of angle measurement. After each all-round turn of the antenna the position of the origin is re-fixed. There is $340/\Delta\alpha$ data packets acquired in a single overview run of the rf, which are summarised into one file, corresponding to a current amv's position. The azimuth α is measured respective to the forwardly directed axis of the mobile amv. In order to obtain the invariant representation of the Map there is inevitable to transform the data of each position file into rectangular Map, invariant to the current amv's position. The need for this transformation follows from the fact, that the mobile amv moves with three degrees of freedom, within the space (x, y, φ), but the results of the range measurements inevitably must be saved in a form independent of the position (x, y) and orientation φ of the amv.

3.2 TRANSFORMATIONS OF CCD CAMERA DATA

Here the problem is not so easy and transparent as in the previous case. First, the important features must be extracted from each camera snap. The solution to the problem was divided into following steps. One camera snap is performed for each value of the α. From each snap objects are isolated using separation methods. Thresholding, colour discrimination, cluster analysis, separation and matching methods were checked to identify the objects closest to the amv at its instant position. Descriptors are extracted for different objects. Finally, the important features representing selected objects are transformed from perspective to rectangular representation of the Map. Calibration using some known objects is performed in preprocessing step.

3.3 COMPARISON OF THE DATA

Comparison of the data acquired from two different sensors matching procedure of two images presented in the two different scales. This is the fundamental problem solved in the presented paper.

- The both scales are fixed using some known calibrating objects at known distances.
- The unification of scales with the Map scale.
- Weighted matching procedure.
- Returning to object space.
- Results replace old data in the Map with the weights proportional to the magnitude of weight coefficient.

4 EXPERIMENTAL PART

4.1 LABORATORY TESTS

The described algorithm was tested in laboratory conditions, resembling the situation in all supposed possible applications.

Figure 2 Laboratory situation from CCD camera

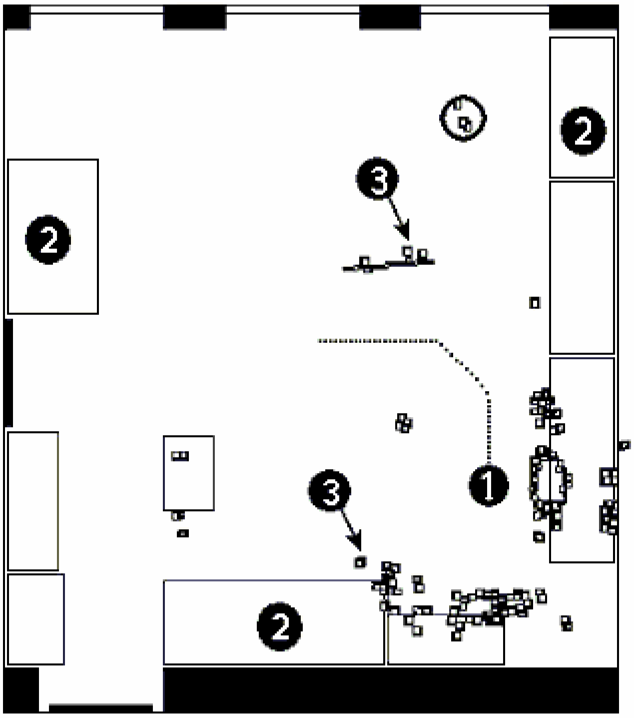

Figure 3 Ultrasound locator data.

One example of the CCD camera view from laboratory environment is shown on the Figure 2. The Figure 3 shows the ultrasound locator data plotted by PC into a hand made map of laboratory: rectangles **2** represent the furniture, **1** labels the actual instant position of the ultrasound locator, a dotted line represents a planned path for the amv. Small squares **3** show positions of obstacles as found by ultrasound locator.

The ultrasound locator data are transformed from locator polar coordinates to rectangular coordinate system of the Map(x, y):

$$
\begin{aligned}
x &= r \cdot \sin\vartheta \cdot \cos\varphi \\
y &= r \cdot \sin\vartheta \cdot \sin\varphi \\
z &= r \cdot \cos\vartheta
\end{aligned} \tag{1}
$$

The angle $\vartheta =$ const defines one plane of scanning of the environment, the $\vartheta = \pi/2$ correspond to scanning in a horizontal plane.

Similarly, the data read from a camera snap is transformed using principal equations of geometric optics [1]. We use a reduced colours representation of laboratory (see Figure 4) because simplifies image analysis. Here only grey scale was used.

Reduced colours have following advantages: maintains colour information, but reduces the number of colours simplifying the analysis. Some of objects may differ in colour so they are easily distinguished from other differently coloured objects.

Figure 4 Reduced colours representation of laboratory.

In fact, the „colour analysis“ operates with „colour windows“ instead of exactly defined monochrome colours. In a 24-bit CCD camera image each coloured patch does not appear as monochrome but it is built up from pixels slightly differing from each other. The building of „colour windows“ is based on three histograms for R, G, B components. A window is then defined as a combination of ΔR, ΔG, ΔB where $\Delta R = (R_{upp} - R_{low})$ and the both right-hand side values are taken from A_0 / e points of the maximum peak in the R colour histogram, defined similarly as shown in Figure 10. Then two extra windows are obtained, first containing all the colours under the R_{low} value and the second one from the colours above the R_{upp} value. Similarly ΔG, ΔB are defined.

A cluster analysis was applied to the Figure 4, resulting in very simplified image of the edges of objects placed on the scene (see Figure 5).

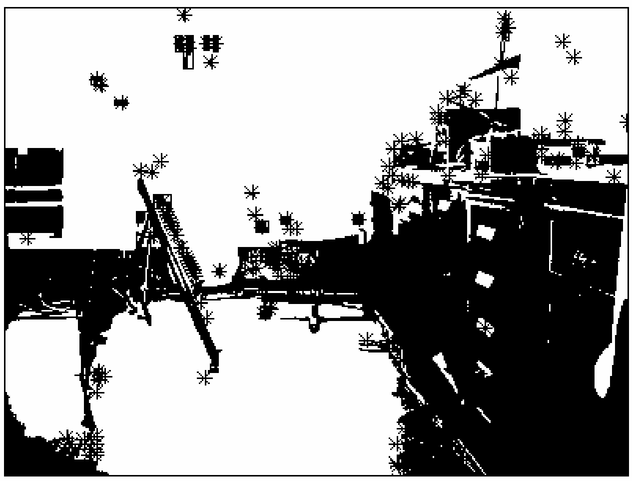

Figure 5 Asterisks labelling the points found by cluster analysis drawn into a camera view.

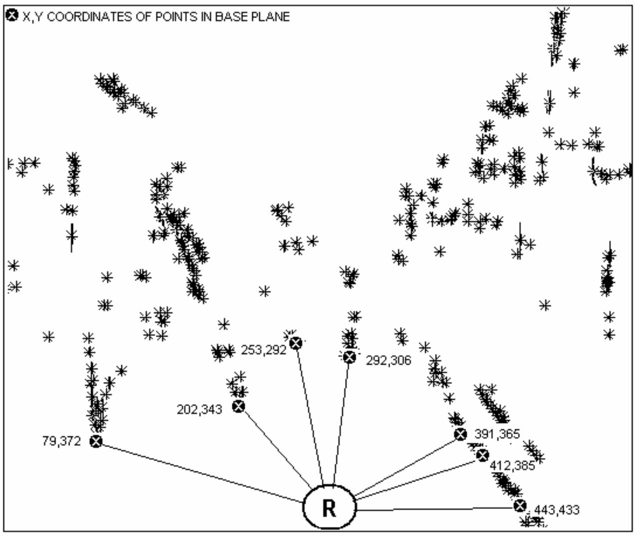

Figure 6 Cluster analysis extracted objects.

The Figure 6 offers a possibility of direct reading the depth of lowest edge points, making use of transformation from perspective to rectangular Map, showing objects extracted by cluster analysis as they are seen from the standpoint of amv *R*. Depicted crossed circles are closest points to *R*, lying in the base plane Each position within the Map corresponds uniquely to a position in the perspective-image of the scene.

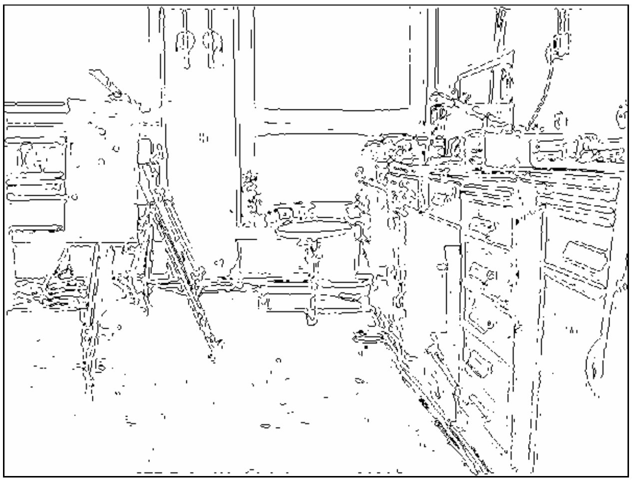

Figure 7 Vertical edges were enhanced using vertical Sobel operator.

The transform depicted in the Figure 8 but concerns the points (in a regular rectangular square grid) placed in the base plane of the scene for them $y = 0$. The asterisks represent the perspective images of the nodes of a regular rectangular square grid, the crosses represent the same nodes after the transformation to the rectangular map.
Many of human made and indoor situated artefacts have prevailing vertical lines features. Those objects may be found using vertical Sobel operator as is shown in Figure 7.

The vertical edges of objects very often end on the ground plane and the lowest ends of vertical edges are easily recognized finding the nearest points from the supposed standpoint of the camera. These lowest points are labelled as crosses in black circles in the Figure 6, which shows simple features figure of the scene with down-ends of vertical edges.

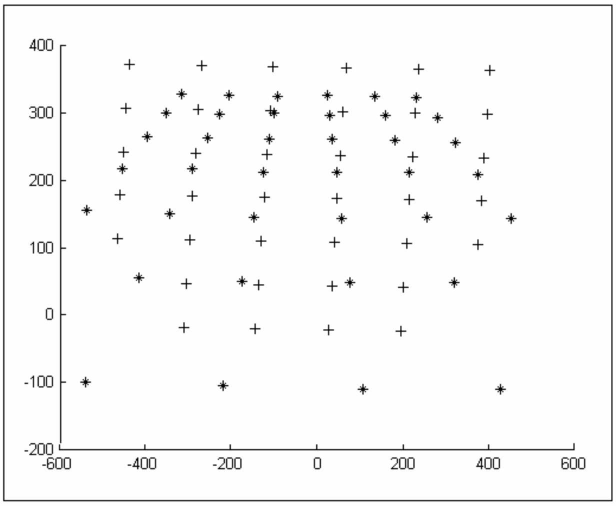

Figure 8 Nodes of the regular rectangular square grid.

4.2 THE PERSPECTIVE TRANSFORMATION

The perspective transformation may be described by simple equations [1]

$$
\begin{aligned}
x &= -x' \cdot \frac{a}{c \cdot z'} \\
y &= -y' \cdot \frac{b}{c \cdot z'}
\end{aligned}
\tag{2}
$$

The *z*-axis is identical with the optical axis of the camera lens. The *x* and *y* are transversal axes, *x'*, *y'* are transversal axes in perspective view. The *z*-axis direction is anti-invariant to the transformation. The coefficients *a*, *b*, *c* are found from an image of a known object at a known position.
The motion of the amv *R* is plotted into the rectangular Map. As the amv moves along arbitrary path, the path elements of any curved path may be always represented by sections of a circle. The current actual arc section of the amv's path Δ has its own centre *C* of curvature representing a fixed point from the point of view of the amv's camera (see Figure 9, where is shown virtual movement of environment points in a amv's frame of reference as a result when amv was moving along a circular path element Δ centred in *C*). Here the camera is placed at the top of the arrow and the time interval corresponds to the time interval which run when movement of the amv along the path element Δ were performed.

Correlation coefficient were found testing whether the picture of *P'* rotated object corresponds really to the original picture of the object *P*.

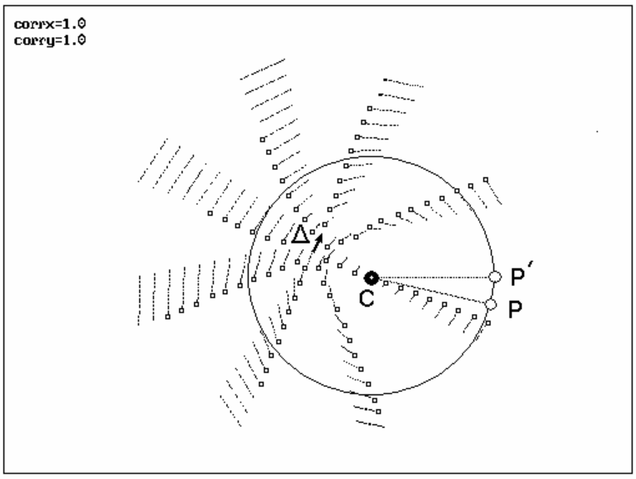

Figure 9 Virtual movement of environment points.

For small increments Δx, Δy a total path increment in xy plane is $\Delta = \sqrt{((\Delta x)^2 + (\Delta y)^2)}$, $\Delta z = 0$.

The complete transformation including both rotation and translation motions may be written down in homogenous coordinates

$$\begin{Bmatrix} x \\ y \\ z \\ t \end{Bmatrix} = \begin{Bmatrix} \cos\varphi & \sin\varphi & 0 & \Delta x' \\ -\sin\varphi & \cos\varphi & 0 & \Delta y' \\ 0 & 0 & m & \Delta z' \\ 0 & 0 & 0 & 1 \end{Bmatrix} \cdot \begin{Bmatrix} x' \\ y' \\ z' \\ 1 \end{Bmatrix} \tag{3}$$

where

$$\begin{aligned} \Delta x &= -\Delta x' \cdot \frac{f}{d} \\ \Delta y &= -\Delta y' \cdot \frac{f}{d} \end{aligned} \tag{4}$$

where d is a distance of transformed point along the z-axis, f is a focal distance of the camera lens and t represents a fourth, homogeneous coordinate.

Setting $x = x'$, $y = y'$, $z = 0$ the coordinates of the point C are found. The point C is invariant under the transformation. The m stands for magnification coefficient. In the Figure 9 the fixed point is labelled by the circle C, the arrow shows the current path increment Δ, passed by the amv. Short straight line sections correspond to the virtual motion of the corresponding environment points. The motion is relative to amv, stressed points on their ends represent virtual end positions. That means, when amv moves along the arrow by the increment of the path Δ, the arbitrary point P of the environment shifts virtually to the position *P'* along the circle centred in C.

5 THE MATCHING PROBLEM

5.1 THE WEIGHTED MATCHING

Let us have two different sensors collecting range data into two corresponding but independent sets, say U, V. Taking randomly one value U_i from the first set and V_j value from the second one, we form a couple $q(Ui, V_j)$ with the Euclidean distance $E(q)$ between its members

$$d_{i,j} = Q(U_i, V_j) = E(q(U_i, V_j)) \tag{5}$$

The data from the sets U and V can be matched if an Euclidean distance $d_{i,j}$ fall into a region of importance which has a width 2σ. The region is defined by the matching weight function. The weight value is attached to each couple of data.

The weight function $W(d)$ is defined as a two dimensional, rotation symmetric Gaussian function $G(A_0, \sigma, d)$

$$W(d) = G(A_0, \sigma, d) = A_0 \cdot e^{-\frac{d^2}{2\sigma^2}} , \tag{6}$$

see Figure 10, expressing the amplitude of the matching weight A decreasing with Euclidean distance d as defined above. The nearer are the members of the couple to each other, the greater is the weight assigned to the current couple of data, no matter of the direction. Here the σ represents mean "sparse" dispersion value of ultrasound measurements.

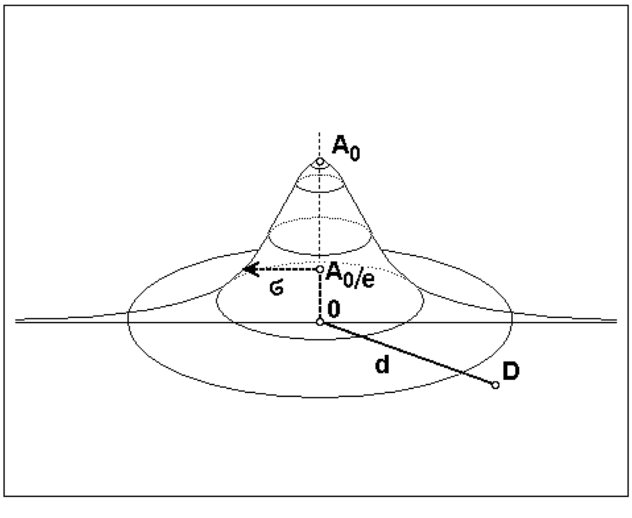

Figure 10 The matching weight function.

5.2 SPARSE DATA

Sparse data is obtained when range and position of any object are independently of the used sensor and method of measurement. Let us illustrate the problem using range finder scanning the environment using the ultrasound rf.

Sparse data are obtained measuring the range by the rf from a fixed position, see the R in a Figure 6. The data may be denser by repeating the measurement under the same conditions but from different positions of the amv. This method requires the movement of the range finder relative to the objects, which should be mapped. The updating of the environment map is then based on the range data, which was collected as the vehicle moves in short steps along the known path. At the end of each step the scanning of the environment was performed. The scanning yields information, which is always obtained in amv's frame of reference. The information must be transformed into the form invariant of the amv's position, that means into a map in the laboratory frame of reference. If the chart of environment is known, the matching of data acquired by rf. to the objects in the map may start.

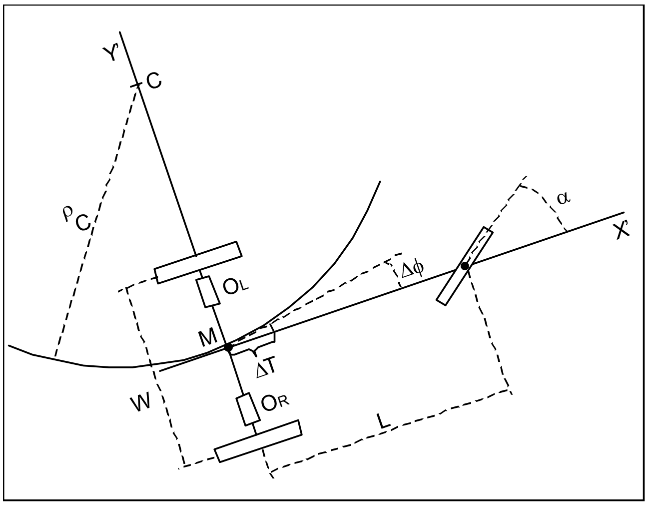

Figure 11 Vehicle's frame of reference.

5.3 THE MATCHING ALGORITHM

In short the matching algorithm may be summarized into following steps:

1. The path of the vehicle is defined by sequence of coordinates of reference points in laboratory frame of reference.
2. The full information of vehicle instant position must be corrected using odometry data together with range finder data. The supposed vehicle position in the scene is generally different from the real one. The odometry gives the information about the state variables of the vehicle without feedback to the environment. For this reason the position estimation based on another sensor principle is inevitable. We use the range finder data and matching algorithm [2] for it's processing. Simulation results from matching algorithm are shown in the Figure 12 a, b.
3. Range finder data are collected in the vehicle's frame of reference by scanning a space around the vehicle's instant position M and they are stored into a structured file.
4. The point C is fixed in both frames of reference. The coordinates of the point C are found in the laboratory frame of reference making use of the known position of this point in the vehicle's frame of reference. The steering angle α is related to ϕ by

$$1-\frac{\Delta T}{L}=\cos\Delta\phi-\sin\Delta\phi\cdot\arctan\alpha$$

see the Figure 11.
5. A transformation of all points, found by range finder, to laboratory coordinate system is performed and results are stored into the Map file.
6. Vehicle passes to new position taken from reference path. New position of the vehicle is calculated, the path is incremented and the process returns back to the step 2 until the end point of the path is reached.

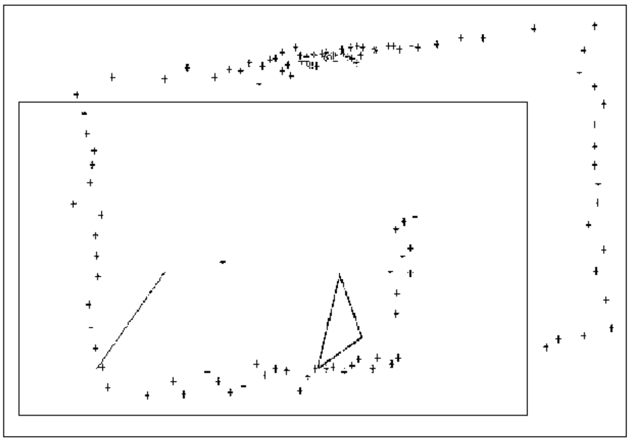

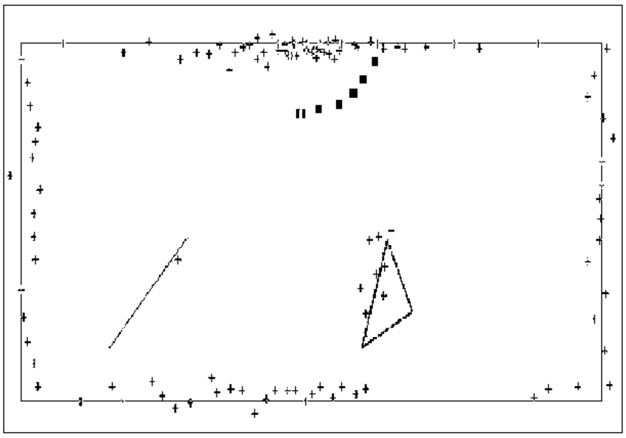

Figures 12a and 12b The range finder data before and after the matching algorithm were applied.

Within the vehicle's frame of reference coordinates of obstacle's point $P(X', Y')$ are

$$X'=r_p\cdot\cos(\gamma_p)$$
$$Y'=r_p\cdot\sin(\gamma_p) \tag{7}$$

where the azimuth angle γ_p is range finder beam direction within the vehicle's frame of reference, r_p is the range value equal to the distance of the obstacle in that direction. The point C is fixed in both frames of reference. The fixed point C is invariant with respect to local translation and rotation. In vehicle's coordinates it is always placed at the Y' axis perpendicular to the vehicle's longitudinal axis. If the position of the point M is known, the coordinates of the point C in the vehicle's frame of reference are

$$X' = 0, \quad Y' = \rho_c = \Delta T / \Delta\Phi, \quad \gamma_c = \pi / 2 . \tag{8}$$

In laboratory frame of reference it is always the centre of curvature of the local arc of path, i.e., the point C appears at the normal to the local path element. The angle is given by the sum of the angle measured by the range finder and the heading angle. The coordinates of the point C are

$$X_c = X_M - \rho_c \sin\Phi, \quad Y_c = Y_M + \rho_c \cos\Phi . \tag{9}$$

During the vehicle motion are identified all new realities that are serve for local map updating. Let P be a point on an obstacle found by the range finder from the n-the position. The distance D of the point P from the fixed point C, calculated from the range finder data, is

$$CP \equiv D_P = \left(\rho_c^2 + \rho_p^2 - 2\rho_c\rho_p \cos\left(\gamma_P - \frac{\pi}{2} \right) \right)^{\frac{1}{2}} , \tag{10}$$

where $\cos(\gamma_p - \pi/2) = \sin \gamma_p$ is found by range finder and then

$$\begin{aligned} D_P &= \left(\rho_c^2 + \rho_p^2 - 2\rho_c\rho_p \sin\gamma_p \right)^{\frac{1}{2}} \\ \sin\delta &= \left(\frac{\rho_p}{D_p} \right) \cdot \cos\gamma_p \end{aligned} . \tag{11}$$

Coordinates of the measured point P in the laboratory frame of reference are

$$\begin{aligned} x_p &= x_M + \rho_p \cos(\gamma_P + \Phi) = x_M + X'_P \\ y_p &= y_M + \rho_p \sin(\gamma_P + \Phi) = y_M + Y'_P \end{aligned} \tag{12}$$

The calculation of its coordinates by fixed point is given by

$$\begin{aligned} x_P &= x_C + D \sin\delta \cos\Phi = \\ &= x_C + \rho_p \cos\gamma_p \cos\Phi = \\ &= x_M - \rho_c \sin\Phi + \rho_p \cos\gamma_p \cos\Phi \\ y_P &= y_C - D \cos\delta \cos\Phi = \\ &= y_C - \rho_p \sin\gamma_p \cos\Phi = \\ &= y_M + \rho_c \cos\Phi - \rho_p \sin\gamma_p \cos\Phi \end{aligned} \tag{13}$$

This calculation is very simple and fast as the first two terms on the right hand side of (13) are calculated only once while the point C is fixed. The existence of the fixed point simplifies the transformation so that the positions of all points P_i (ρ, γ) measured by the range finder from one single point of view may be transformed to the laboratory frame of reference in a single step as follows

$$\begin{aligned} P_i(x,y) = T(X_c, Y_c) \cdot R^{-1}(-\Delta\Phi) \cdot T^{-1}(X_{c,} Y_c) \cdot \\ \cdot \{ P_i(\rho \cdot \cos\gamma, \rho \cdot \sin\gamma) \} \end{aligned} \tag{14}$$

i.e., translating the C point to the origin, rotating all the points P_i around the origin by the angle inverse to the last increment of vehicle's rotation and translating the coordinate system back to its original position.
The virtual displacement of the point P indicates where the range finder should find the point P in vehicle's coordinates after the ($n+1$)-th section of the path has been passed by the vehicle:

$$P_{n+1} = P_n + \Delta P_n = P_n + D \cdot \Delta\Phi_n . \tag{15}$$

The last equation may be also used for checking and testing the reliability of the range finder measurement. Making use of the odometric system [4] the vehicle always has evidence of the path it yet had passed.

6 CONCLUSION

Some of above formulated problems were solved, the rest of them is in work till now. Namely, the problem of identification of the objects within the Map was not yet solved satisfyingly. We elaborated some methods based on different ways of data filtration, transformations, correlation and cluster analysis. The problem is not in methods themselves but in the operation time of corresponding procedures, requiring extensive numerical processing. The work on identification of the objects is supposed to be continued.

ACKNOWLEDGEMENTS

The work has been supported by the grant agency VEGA MŠ SR a SAV grant No. 2/3129/25.

REFERENCES

[1] Born M., Wolf E., *Principles of Optics.* Pergamon Press, Oxford, Edinburgh, New York, Paris, Frankfurt, 1964.

[2] Varga M., Janglová D., Považan I., and Pomšár A., The Autonomous 3-wheel Mobile Robot A Project Survey. *Proc. of the ISMCR´93*, Torino, Italy, pp. Bm.II-15 -Bm.II-20, Sept. 1993.

[3] Považan I., Janglová D. and Uher L., Odometry in Determination of the Position of an Autonomous Mobile Vehicle. *Proc. of 4th Int. Symp. on ISMCR'95*, Smolenice, Slovakia, pp. 425-429, June 1995.

[4] Cox L., Blanche J., An Experiment in Guidance and Navigation of Autonomous Robot Vehicle, Work Project No.311401-2599, August 24, 1989.

[5] Tsai R. Y., A Versatile Camera Calibration Technique for High Accuracy 3D Machine Vision Metrology. *IEEE Journal of Robot. and Automation*, Vol. RA-3, No 4, August 1987.

[6] Elfes A., Multi-Source Spatial Data Fusion Using Bayesian Reasoning, Data Fusion in Robotics and Machine Intelligence, M.A. Abidi and R.C. Gonzales eds., Academic Press. Inc., 1992.

ISSN 1590-8844
International Journal of Mechanics and Control, Vol. 06, No. 02, 2005

FLOW NUMERICAL ANALYSIS IN CARDIOVASCULAR DISTRICTS

Cristiana Delprete, Raffaella Sesana

Politecnico di Torino, Dipartimento di Meccanica, Corso Duca degli Abruzzi 24, 10129 Torino, Italy

ABSTRACT

The application of simulations results of blood system 2D FE models to medical research can aid surgeons and cardiologists to better comprehend and foresee the phenomena related with blood circulation. As an example, a comparative and parametric analysis of factors influencing pressure, velocity profiles and blood distribution in Bi-directional Cavo-Pulmonary anastomosis (i.e. modified Glenn surgical intervention) has been developed by means of 2D and 3D computational fluid dynamic mathematical models of the Mean Pulmonary Artery bifurcation and of the Superior Vena Cava anastomosis to the Right Pulmonary Artery. The investigated parameters are: connection angle between Right Pulmonary Artery and Superior Vena Cava, Mean Pulmonary Artery and Superior Vena Cava flows. Simulations results agree with literature simulations and with clinical data. 2D model better adapts to parametric analysis of flow evolution phenomena.

Keywords: Finite Element Analysis (FEA), Computational Fluid Dynamics (CFD)

1 INTRODUCTION

Surgeons in general and cardiovascular surgeons in particular need models, diagrams and simulators easy to tare on individual patient data and with real time results able to help in pre-intervention evaluation. Surgeons experience is the main source of information but other can result from numerical models of circulating system. Engineering applied to medicine helped in learning how to simplify and model human system. Numerical and analytical more or less complex models of organic subsystems are well described in literature, modelling the behaviour of human locomotion system, circulatory system, response to drug administration, and so on.

Lumped parameters models have been developed to describe the circulation system behaviour [1, 2, 3, 4]. CFD has been widely applied in the investigation of flow in blood vessels since the ’80s. CFD models presented in bibliography [5-10] describe blood as a Newtonian fluid, stationary flows, rigid and no-compliant walls and other simplifications.

Contact author: Raffaella Sesana,

raffaella.sesana@polito.it

In the simulated flow ranges they do not seem to involve errors bigger than those coming out of individual anatomical and physiological variability [11-17].

The present paper describes the first step of a project dedicated to obtain an interactive whole blood system multi-scale simulator to help surgeons in pre-intervention patient tailored real time evaluations. The paper is dedicated to evaluate the quality of the numerical results obtained from a 2D numerical model compared with those of a 3D numerical model for a cardiovascular district. The presented Bi-directional Cavo-Pulmonary anastomosis (BCPA) 2D FEA is only an application example of the general methodology here proposed. The incidence of this particular surgical intervention justifies necessity to rapidly evaluate surgery impact and follow up. The main aim is then to investigate if a 2D model, in which blood vessels have been assumed to be coplanar, can correctly evaluate flow and pressure profiles in BCPA district.

In general 2D models can be easily used for parametric analysis which results can be organized to be helpful for medical applications. Thus the secondary aim is to investigate the influence of connection angle between Right Pulmonary Artery (RPA) and Superior Vena Cava (SVC), Mean Pulmonary Artery (MPA) and SVC flows and lung resistance on the efficacy of the BCPA procedure.

BCPA (also named modified Glenn surgical intervention) nowadays represents the obligatory first step in

"physiologic" correction of monoventricular hearts. It is an end-to-side anastomosis between SVC and RPA, meant to decrease the heart volume overload and to support or replace the right ventricle functionality. A laminar flow adequately distributed to both lungs is the goal of the BCPA procedure.
Since the '90s the Cavo-Pulmonary connection has been analysed by many research groups that developed *in vitro* [13-15] and *in vivo* [12] experimental flow investigations. At the same time many papers have been dedicated to 3D simulations of BCPA anastomosis area [1, 3, 5, 9, 10, 18, 19, 20-22]. In [5] an *in vitro* comparative investigation on two Fontan configurations with right ventricle by-pass (Atrio-Pulmonary connection APC, and total Cavo-Pulmonary connection TCPC) have been analysed. Experimental models have been developed with fixed connections, continuous flow, pressure measurements and calculation of total energy loss coefficients. These experimental results have been showed that TCPC has better efficiency than APC, especially for flow ranges of approximately 5 l/min. Pulsate flow models showed higher pressure levels than steady flow ones. CFD analysis [10] has been performed to investigate blood behaviour in TCPC by means of a 3D parametric model of the connection. Pulmonary circulation is simulated with a lumped parameters model. The 3D model has been used to simulate local blood fluid dynamics for connections with different geometry, to evaluate energy losses. Joining the FE model and the lumped parameters model in a multi-scale model, the results have been showed that energy losses can be reduced with a correct hydraulic configuration, which allows a proper distribution of blood flow between the two lungs. Lowest energy losses can be obtained with an angled SVC anastomosis but this flow distribution is far from physiologic ranges. A small pressure offset can attain a good flow distribution with limited local energy losses. The attention is focused on development of multi-scale models to properly describe initial and time varying boundary conditions of FE models to investigate fluid dynamic behaviour of specific circulating system areas. The initial and boundary conditions can be computed simulating the whole circulation system with exception of CFD model limited volumes in which local flow evolution is simulated. Lumped parameters models are obtained by applying hydraulic and electric analogies to blood districts; examples are reported in [1, 10, 18, 22, 23]. From the performed bibliographic analysis it is evident how CFD well adapts to blood flow investigation even if it is difficult to adequately simplify the physiological circulation in a numerical model.
In the present paper a 3D FE fluid dynamic model has been built to compare the performed ADINA (ADINA R&D, Inc.) simulations with analogous simulations available in literature [18] with the same geometry, load and boundary conditions and with different numerical solvers. Then a 2D FE fluid dynamic model with the same geometry, load and boundary conditions has been developed to compare the flow system results obtained in 2D and 3D simulations, in different flow conditions, with the same software code ADINA. A parametric analysis on 2D model has been developed. The obtained 2D and 3D results in terms of flow and pressure profiles, flow distributions between Right and Left Pulmonary Artery (RPA and LPA) have then compared.

2 MATERIALS AND METHODS

Two CFD models (3D and 2D) of the same blood districts (MPA bifurcation into RPA and LPA, together with RPA and SVC anastomosis) have been developed.
Rhinoceros 2.0 software (Robert McNeel & Associates) has been used for geometric models; ADINA 7.3.2 fluid dynamic FE software has been used for pre-processing, solving mathematical Navier-Stokes fluid dynamic equations [11] and post-processing data.
Geometry and boundary conditions have been assumed from analogous studies available in literature [10, 18, 24]. Both the developed models have rigid walls, homogeneous incompressible and Newtonian fluid, and boundary slip is assumed null. Four different flow conditions (Tab. I, rows from A to D) have been applied to investigate flow range of patients undergoing BCPA. For both models velocity profiles on inlet sections are assumed parabolic, laminar and stationary in SVC, while they are assumed flat and pulsate in MPA (120 bpm, $t_{systole} = t_{diastole} = 0.25$ s). Pressure is assumed uniform on both outflow sections, with the same value on both sides. From flow conservation equation this value depends on the inlet flow [11].
The 3D FE model (Fig. 1a) has been built using 4 nodes isoparametric tetrahedron elements (62855 elements, 13059 nodes). Sensitivity analyses on mesh and node refining algorithm have been applied. 3D model simulation results have been validated with analogous simulations available in literature [18] with same geometry, load and boundary conditions.
The 2D FE model (Fig. 1b) has been built to compare the results obtained by 2D and 3D simulations in six flow conditions (Tab. I, flow id. from A to F). 2D FE model has been obtained from the median section of the 3D one, using 3 nodes triangular elements (6003 elements, 3294 nodes). Sensitivity analyses on mesh and node refining algorithm have been applied. 2D model has the same boundary and load conditions of the 3D one with two additional conditions (flow id. E and F of Tab. I). Comparisons of models results have been performed in terms of pressure and velocity profiles and flow distributions on sections R down/up and L down/up. In the parametric analysis performed to investigate lung resistance effect, RPA and LPA measuring sections have been shifted before the corresponding bifurcations and have been called RS and LS respectively (Fig. 1).

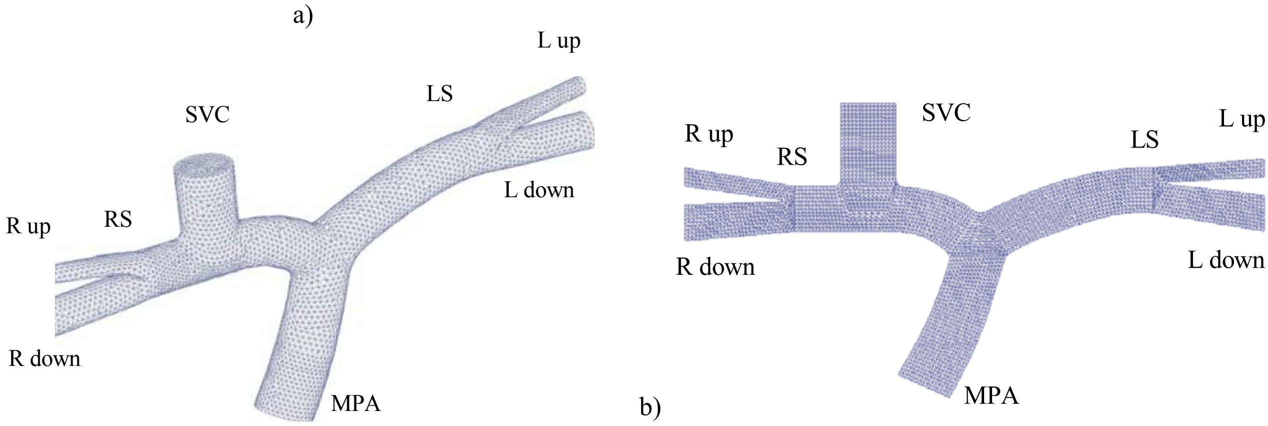

Figure 1 Models mesh and data measuring sections of a) 3D FE model, and b) 2D FE model. R down and R up, S down and S up are respectively the sections facing right and left lung, RS and LS the same sections before corresponding bifurcations, MPA and SVC the section facing ventricle and SVC.

Table I - Flow conditions numerically investigated.

Flow id.	MPA flow [l/min]	SVC flow [l/min]
A	1.80	1
B	1.35	1
C	0.90	1
D	0.45	1
E	0	1
F	0	2

Parametric analysis of the influence of SVC-RPA anastomosis angle, fluid dynamic factors and pulmonary resistance on velocity and pressure profiles and on flow distributions has been performed on the 2D FE model. Five different values of the SVC-RPA angle α ranging from 25° to –25° have been tested (Fig. 2).

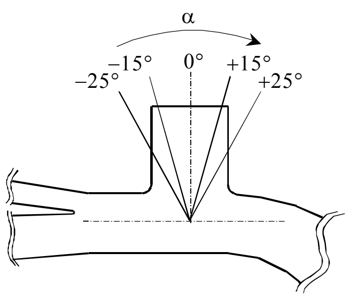

Figure 2 SVC-RPA anastomosis angles investigated with 2D FE model.

Two parameters have been defined to describe pulmonary resistance by means of left and right lung resistances:

$$\beta = \frac{R_L}{R_R}, \quad \gamma = \frac{1}{\beta} = \frac{R_R}{R_L} \tag{1}$$

where R_L and R_R are left and right lung resistances in mm_{Hg} respectively, β and γ are simply one the inverse of the other.

Actually β and γ are both used to describe system behaviour with the aim to allow a better comprehension of simulation results. When right lung pressure is fixed and left lung pressure varies, β is the reference parameter. Vice versa, when left lung pressure is fixed and right lung pressure varies, γ is the reference parameter. So it is easier to identify the non-symmetrical behaviour of systems in which lung blood districts are different and symmetrical variations of pressure values cause non-symmetrical variations of measured parameters. Seven different values of β and γ parameters ranging from 0.75 to 1.25 have been investigated keeping the first fixed and the second variable, or vice versa.

According to [18, 19, 25] from lumped parameter model of pulmonary circulation (Fig. 3) inlet and outlet left and right lung pressure have been computed, for each β and γ value, by means of flow balance equation in [11] and inlet left atrium pressure.

For each low condition, fluid dynamic efficiency η_E has been computed according to [10] as:

$$\eta_E = 1 - \frac{E_{lost}}{E_{in}} = 1 - \frac{E_{out} - E_{in}}{E_{in}} \tag{2}$$

Inlet energy E_{in} is the sum of static and kinetic energies, integrated on each inlet section. Dissipated energy E_{lost} takes into account all energy losses (static and dynamic due to friction, vortex, etc.); it is calculated as the difference between total incoming and outcoming (E_{out}) energies:

$$E_{in} = Q_{in} \cdot \left(p_{in} + \frac{1}{2}\rho v_{in}^2 \right), \quad E_{out} = Q_{out} \cdot \left(p_{out} + \frac{1}{2}\rho v_{out}^2 \right) \tag{3}$$

where Q_{in} and Q_{out} are flows (m^3/min) through inlet and outlet sections, p_{in} and p_{out} static pressures (Pa) on the same sections, ρ fluid density (kg/m^3), v_{in} and v_{out} mean fluid velocities (m/s).

3 RESULTS AND DISCUSSION

In Table II 3D model results are compared with bibliographic data [18] obtained with same geometry, boundary and load conditions. Mean, maximum and minimum values are computed during a complete cardiac cycle. MPA and SVC computed pressure profiles are almost overlapping; in the worst case difference is lower than 5% compared with [18]. The same happens for flow distributions (differences lower than 3%). Worse values (differences around 20%) are achieved only for the lowest values of pressure.

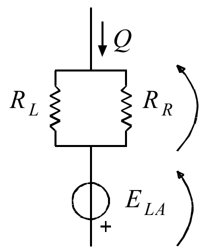

Figure 3 Lumped parameter model to compute pressure on outlet sections. R_L and R_R are left and right lung resistance, Q total flow from ventricle and SVC, E_{LA} left atrium pressure.

Figures 4 and 5 show mean, maximum and minimum pressure values in respectively, in different flow conditions. The 3D FE model here developed and simulated well fits bibliographic data. The 2D FE model simulation results and the corresponding 3D FE model results are compared in Table III. Worse values (around 20%) are achieved for the lowest values of pressure. This seems again to be due mainly to the numerical procedure. MPA and SVC pressure profiles versus time for 2D and 3D models in A flow condition (1.80 l/min in MPA and 1.00 l/min in SVC) are shown in Figure 6, as example. The profiles are almost overlapping.

2D model results have been also compared with bibliographic data [9, 18, 19] except for flow distribution between left and right lung. Flow distribution results from 2D simulations are closer to physiologic data [12] than to bibliographic data [18]. In particular it can be noted that, according to physiologic data, 2D simulations results show a preferential flow to right lung which has a higher volume than left one.This does not occur in 3D simulations. Flow distribution differences between 2D and 3D models, anyway, are lower than 10%. The comparison of the results of 2D and 3D FE models allows asserting that shape and MPA pressure trend are very similar. The main differences are obtained for maximum and minimum values of pressure at inlet and outlet sections.Parametric analysis on 2D FE model performed on SVC-RPA anastomosis angle (α) and lung resistance variations, in different flow conditions, and has requested 48 simulations. The obtained results (Fig. 7) point out that the best value for the angle between SVC and RPA is $\alpha = +25°$ as it allows the more physiological distribution of flows between lungs.

Forward flow in MPA shows to favour left perfusion. It is evident that increasing MPA flow left lung perfusion increases and right lung perfusion decreases, remaining however higher than left lung perfusion. It is also relevant that the influence of the angle between SVC and RPA appears less significant in presence of flow in MPA rather than when this flow is null, that is residual flow in MPA limits the effect of anastomosis angle variation on the flow distribution and profiles. This result confirms the necessity to surgically preserve forward flow from right ventricle, when possible.

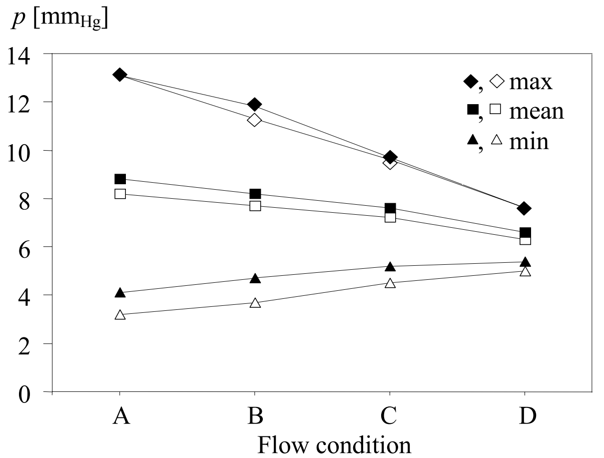

Figure 4 Pressure in MPA for different flow conditions; 3D FE model (black symbol) and data from [18] (white symbol).

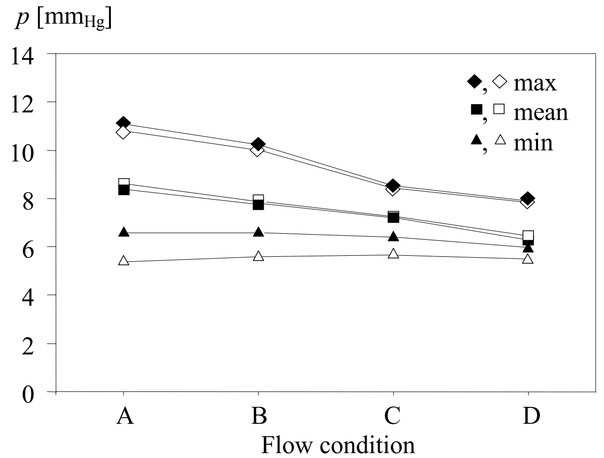

Figure 5 Pressure in SVC for different flow conditions; 3D FE model (black symbol) and data from [18] (white symbol).

Table II - Comparison between 3D FE simulation results and bibliographic data from [18] for different flow conditions.

Flow condition	A		B		C		D	
FE model	3D	[7]	3D	[7]	3D	[7]	3D	[7]
Mean MPA flow [l/min]	1.80	1.80	1.35	1.35	0.90	0.90	0.45	0.45
Mean SVC flow [l/min]	1.00	1.00	1.00	1,.00	1.00	1.00	1.00	1.00
Maximum MPA pressure [mm_{Hg}]	13.1	12.9	11.8	11.7	9.7	9.4	7.6	7.3
Mean MPA pressure [mm_{Hg}]	8.2	8.5	7.7	7.8	7.2	7.1	6.3	6.3
Minimum MPA pressure [mm_{Hg}]	3.2	4.1	3.7	4.7	4.5	5.6	5.0	5.4
Maximum SVC pressure [mm_{Hg}]	11.1	10.8	10.2	10.0	8.4	8.3	7.9	7.8
Mean SVC pressure [mm_{Hg}]	8.4	8.6	7.8	7.8	7.2	7.2	6.3	6.4
Minimum SVC pressure [mm_{Hg}]	5.5	6.6	5.7	6.6	5.8	6.4	5.6	6.0
Flow perfusion to left lung [%]	51.2	52.5	51.3	52.7	51.2	52.3	51.0	51.9
Flow perfusion to right lung [%]	48.8	47.5	48.7	47.3	48.8	47.7	49.0	48.1

Table III - Comparison between 2D and 3D FE model results for different flow conditions.

Flow condition	A		B		C		D	
FE model	2D	3D	2D	3D	2D	3D	2D	3D
Mean MPA flow [l/min]	1.80	1.80	1.35	1.35	0.90	0.90	0.45	0.45
Mean SVC flow [l/min]	1.00	1.00	1.00	1.00	1.00	1.00	1.00	1.00
Maximum MPA pressure [mm_{Hg}]	13.1	13.1	11.3	11.8	9.6	9.7	7.6	7.6
Mean MPA pressure [mm_{Hg}]	8.8	8.2	8.2	7.7	7.6	7.2	6.6	6.3
Minimum MPA pressure [mm_{Hg}]	4.1	3.2	4.7	3.7	5.2	4.5	5.4	5.0
Maximum SVC pressure [mm_{Hg}]	11.3	11.1	9.9	10.2	8.6	8.4	7.0	7.9
Mean SVC pressure [mm_{Hg}]	8.8	8.4	8.1	7.8	7.5	7.2	6.6	6.3
Minimum SVC pressure [mm_{Hg}]	6.4	5.5	6.4	5.7	6.4	5.8	6.0	5.6
Flow perfusion to left lung [%]	49.2	51.2	48.4	51.3	47.4	51.2	46.1	51.0
Flow perfusion to right lung [%]	50.8	48.8	51.6	48.7	52.6	48.8	53.9	49.0

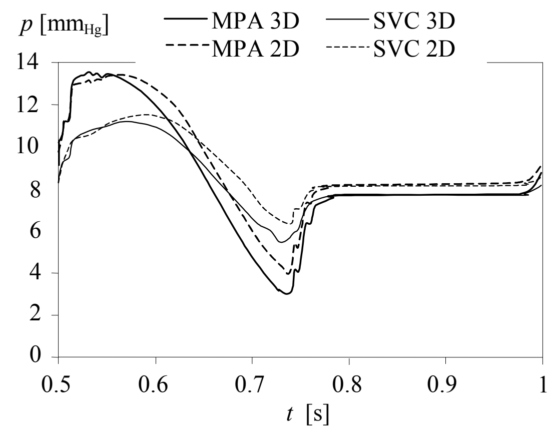

Figure 6 Pressure profiles in MPA and SVC for 3D and 2D FE models (flow condition A).

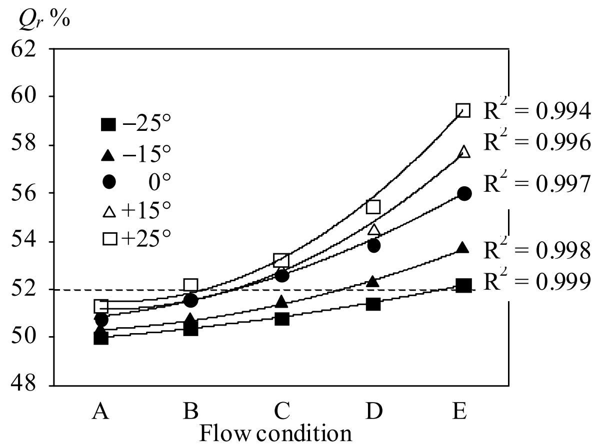

Figure 7 Flow perfusion % to right lung (Q_r) as a function of MPA flow for different SVC-RPA anastomosis angles

Table IV - 2D FE simulation results for different β parameter values (right lung pressure = 7,28 mm_{Hg}).

β parameter value	1.25	1.05	1	0,95	0.75
Left lung pressure [mm_{Hg}]	8,10	7,46	7,28	7,13	6,64
MPA pressure [mm_{Hg}]	9,41±0,07	8,96±0,07	8,86±0,07	0,07	8,56±0,06
SVC pressure [mm_{Hg}]	9,25±0,07	8,86±0,07	8,77±0,07	0,07	8,54±0,06
MPA-RS pressure drop [mm_{Hg}]	2,14	1,69	1,58	1,49	1,28
MPA-SVC pressure drop [mm_{Hg}]	0,17	0,11	0,09	0,07	0,02
Flow perfusion to left lung [%]	26.4	43.6	48.4	53.0	65.7
Flow perfusion to right lung [%]	73.6	56.4	51.2	47.0	34.3

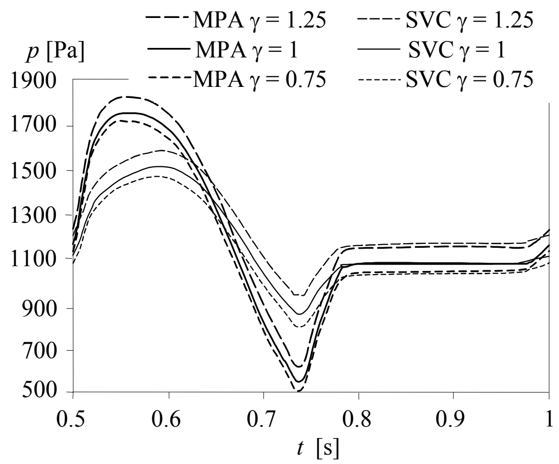

Figure 8 MPA and SVC pressure profiles for different values of γ parameter.

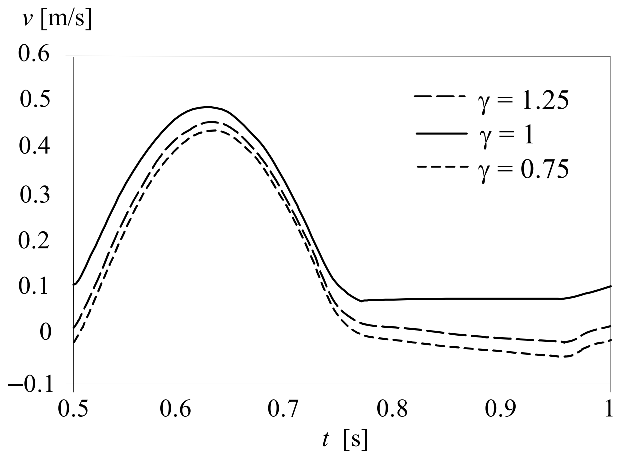

Figure 9 RPA velocity profiles for different values of γ parameter.

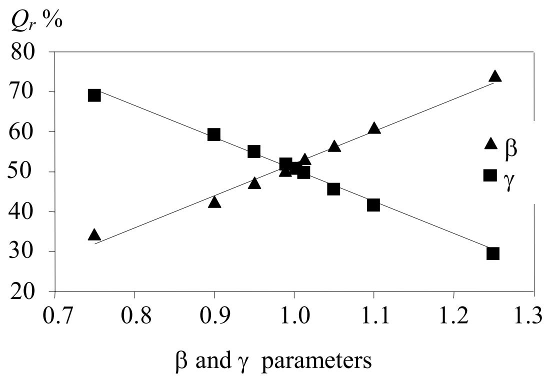

Figure 10 Flow perfusion % to right lung (Q_r) for different values of β and γ parameters and corresponding fitting straight lines.

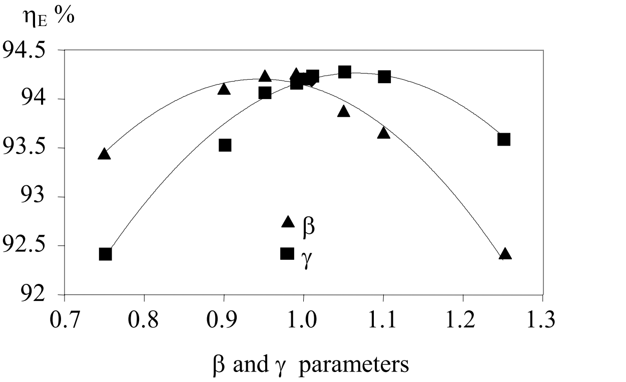

Figure 11 Model efficiency (η_E) for different values of β and γ parameters and corresponding fitting second order polynomials.

Numerical simulation results can be optimally fitted with second order curves (in worst case $R^2 = 0.994$, see Fig. 7). This result is of relevant practical interest because it allows to foresee, and then to correct, flow distribution between the lungs with few flow data, using a numerical model requiring very short computing time.

Results of parametric analysis on the effect of lung resistance variation are shown in Table IV. Rows 3 and 4 report the systole and diastole average pressure values in MPA and SVC (measured in sections indicated in Figure 1b), rows 5 and 6 the pressure difference between MPA and right lung (RS section) and between MPA and SVC mean values on the whole cardiac cycle, rows 7 and 8 the flow distribution to left and right lung. The results are also shown in Figures from 8 to 11.

In Figure 10 flow perfusions versus parameters β and γ are reported. It can be noted that numerical points can be optimally linearly fitted ($R^2 > 0.99$) by a straight line with the same (absolute value) angular coefficient in both cases.

In Figure 11, the efficiency η_E of the 2D FE model is reported as a function of the parameters β and γ, according to definition (2). It can be seen that the maximum values take place for lung resistance ratio different from 1 ($\beta = 1.05$ and $\gamma = 1.01$). Therefore β maximum is higher (0.1%) than γ maximum, that is when left lung resistance is higher than right lung resistance and when 55% flow is directed to the right lung, according to physiologic data.

Finally, it is possible to plot a 3D abacus, i.e. flow distribution to lungs versus anastomosis angle and flow in MPA (or SVC), as indicated in Figure 12.

The abacus can aid surgeons to evaluate surgical strategies before intervention and to lower post-surgery risks. For example, for a given flow in MPA and for a chosen distribution of the flow to the two lungs, the surface in Figure 12 allows to select the optimal SVC-RPA anastomosis angle.

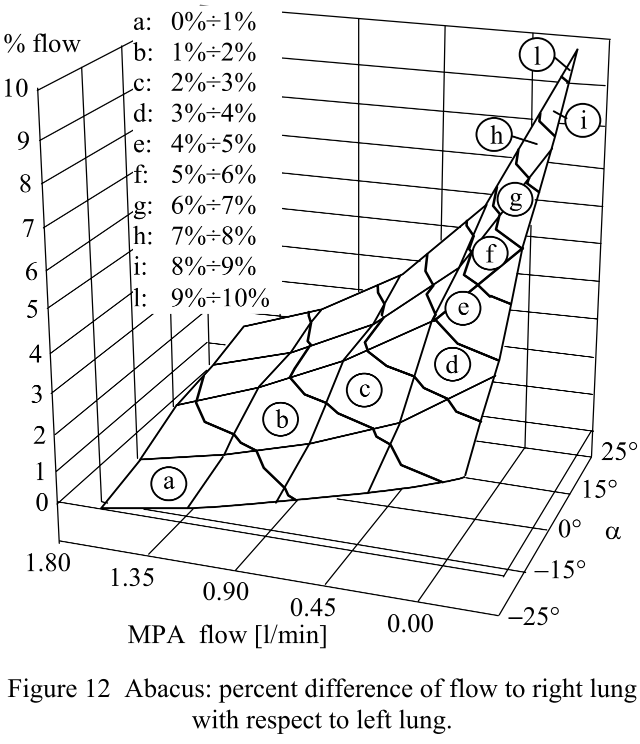

Figure 12 Abacus: percent difference of flow to right lung with respect to left lung.

4 CONCLUSIONS

The simulation results of the BCPA 3D FE model developed in the present paper are validated by bibliographic results obtained in the same conditions with a different software [18]; simulations with the 2D FE model show to agree with bibliographic and with the 3D model results.

The parametric analysis on 2D FE model of the SVC-RPA anastomosis angle and of the pulmonary resistance shows that these parameters are correlated to each other. Theya are also correlated to the flow coming from MPA and to the flow distribution to the right and the left lung.

Investigation on the influence of the pulmonary resistance on the pressure profiles and the flow distribution allows to follow up the system evolution under different conditions. Particularly, pulmonary circulation system sensitivity to minimal variation of pulmonary resistance has been pointed out together with global system stability, moreover the results of the 2D FE model parametric analysis agree with experimental physiologic behaviour.

It can thus be stated that multi purpose software ADINA well applies to this kind of simulations as the obtained results almost overlap the results obtained in [18] with a dedicated fluid dynamic software as FIDAP, both in terms of pressure values and of velocity profiles.

Finally the comparison between the 2D and the 3D FE simulation results allow to assess that the 2D model well adapts to study the evolution of flow phenomena related to pulmonary resistance, anastomosis angle and flow variations, with the advantages of briefer processing time and of easier developing models, allowing to customise and process models before surgical intervention.

ACKNOWLEDGMENTS

We thank Prof. Abbruzzese of the Cardiac Surgery Division of Ospedale Infantile Regina Margherita, Torino, Italy and Mr. Gandar of EnduraTECH R&D, Italy, for their precious contribution and help.

REFERENCES

[1] Migliavacca F., De Leval M. R., Dubini G, Pietrabissa R., Computational model of the fluid dynamics in systemic-to-pulmonary shunts, *J. Biomech*, vol 33, pp 549-557, 2000.

[2] Pietrabissa R., Mantero S., Marotta T., Menicanti L., A lumped parameter model to evaluate the fluid dynamics of different coronary bypasses, *Med. Eng. Phys*, Vol 18, N. 6, pp 477-484, 1996.

[3] Pennati G., Migliavacca F., Dubini G., Pietrabissa R., Fumero R., De Leval M. R., Use of mathematical model to predict hemodynamics in cavopulmonary anastomosis with persistent forward flow, *J of Surgical Research*, Vol. 89, pp 43-52, 2000.

[4] Migliavacca F., Pennati G., Pietrabissa R., De Leval M. R., Bove E. et al., Hemodynamics and hoxygens in the Nordwood circulation: a lumped parameter model, BED Bioengineering Conference, ASME, Vol. 50, pp 913-914, 2001.

[5] Low H.T., Chew T. C. et al. , Flow studies on atrio-pulmonary and Cavo-pulmonary connections of the Fontan operations for congenital heart defects, *J. Biomed. Eng*, Vol. 15, pp 303-307., 1992.

[6] Li C. W., Cheng H. D., A non-linear fluid model for pulmonary blood circulation, *J Biomechanics*; Vol. 26, pp 653-664, 1993.

[7] Bathe J., Zhang K. J., Wang M. H., Finite element analysis of incompressible and compressible fluid flows with free surfaces and structural interactions, *Computers and Structures*, Vol. 56, pp 193-213, 1995.

[8] Bathe K. J., Zhang and Wang, M. H., Simulation of structural and fluid flow response in engineering practice, *Computer modelling and simulation in engineering*, Vol. 1. pp 47-77, 1996.

[9] Migliavacca F., De Leval M. R., Dubini G., Pietrabissa R., A computational pulsatile model of the bi-directional cavopulmonary anastomosis: the influence of pulmonary forward flow, *J. Biomech. Eng*, Vol. 118, pp 520-528, 1996.

[10] Dubini G., De Leval M. R., Pietrabissa R., Montevecchi F., Fumero R., A numerical fluid mechanical study of repaired congenital heart defects. Application to the total cavo-pulmonary connection, *J. Biomechanics*, Vol. 29, pp 111-121, 1996.

[11] McDonald D. A., Nichols W. W., O'Rourke M. F., *Blood Flow in Arteries: Theoretic, Experimental and Clinical Principles*, Edward Arnold, Sydney, 1989.

[12] Rebergen S. A., Ottenkamp J., et al., Postoperative pulmonary flow dynamics after Fontan surgery: assessment with nuclear magnetic resonance velocity mapping, *J. Am. College Cardiology*, Vol. 21, N. 1, pp 123-131, 1993.

[13] Siviers.H., Gardes A., Kunze J., Pfister G., Superior hydrodynamics of a modified cavopulmonary connection for the Norwood operation, *Ann. Thorac. Surg*., Vol. 65, pp 1741-1745, 1998.

[14] Lardo A. C., Webber S. A., Friens I., del Nido P. J., Cape E. G., Fluid dynamic comparison of intra-atrial and extracardiac total cavopulmonary connections, The *J. of Thoracic and Cardiovascular Surgery*, Vol. 117, N. 4, pp 697-704, 1999.

[15] Lardo A. C., Webber S. A., Friens I., del Nido P. J., Cape E. G., Bidirectional superior cavopumonary anastomosis improves mechanical efficiency in dilated atripumonary connections, *The J. of Thoracic and Cardiovascular Surgery*, Vol. 118, N. 4, pp 682-691, 1999.

[16] Douglas W., Goldberg C., Mosca R., Bove L., Hemi-Fontan procedure for hypoplastic left heart syndrome: outcome and suitability for Fontan, *Ann. Thorac. Surg*., Vol. 68, pp 1361-1368, 1999.

[17] Magee G., Brian W., McCrindle D., Mawson J., Systemic venous collateral development after the bidirectional cavopulmonary anastomosis: prevalence and predictors, *J. Am. Coll. Cardiol*, Vol. 32, pp 502-508, 1999.

[18] Pennati G., Migliavacca F., Dubini G., Pietrabissa R., De Leval M. R., A mathematical model of circulation in the presence of the bi-directional cavo-pulmonary anastomosis (BCPA) in children with a univentricular heart, *Med. Eng. Phys*, Vol. 19, N. 3, pp 223-234, 1997.

[19] Migliavacca F., Dubini G., Pietrabissa R., De Leval M. R., Computational transient simulations with varying degree and shape of pulmonic stenosis in models of the bidirectional cavopulmonary anastomosis, *Med. Eng. Phys*, vol 19, n°4, pp 394-403, 1997.

[20] Migliavacca F., De Leval M. R., Dubini G., Pietrabissa R., Fumero R., Computational fluid dynamic simulations of cavopulmonary connections with an extracardiac lateral conduit, *Med. Eng. Phys*, Vol. 21, pp 187-193, 1999.

[21] Shew T. W., Tsai S. F., Hwang W. S., Chang T. M., A finite element study of the blood flow in total cavopulmonary connection, *Computers and fluids*, Vol. 28, pp 13-39, 1999.

[22] Migliavacca F., De Leval M. R., Dubini G., A computational fluid dynamics in paediatric cardiac surgery, Images Paediatr. *Cardiol*, Vol. 2, pp 7-19, 2000.

[23] Karlin V., Numerical algorithms for flows in the nodes of 2D models of pipe networks, *J of Computational Physics*, Vol. 132, pp 62-77, 1997.

[24] Migliavacca F., De Leval M. R., Dubini G., Pennati G., Pietrabissa R., Fumero R., Computational 3D models of systemic to pulmonary shunt for the surgical treatment of hypoplastic left heart syndrome, *XI Conf. Of the ESB*, Tolouse, France, 1998.

[25] Noordergraaf A. Development of an analog computer for the human systemic circulatory system' *Analog Computers*, pp 29-44, 1963.

ISSN 1590-8844
International Journal of Mechanics and Control, Vol. 06, No. 02, 2005

A 14 D.O.F. MODEL FOR THE EVALUATION OF VEHICLE'S DYNAMICS: NUMERICAL-EXPERIMENTAL COMPARISON

F. Cheli*, E. Leo*, S. Melzi*, F. Mancosu**

* Politecnico di Milano, Mechanical Department
** Pirelli Tyres

ABSTRACT

The use of 14 degrees of freedom models for numerical simulation of car vehicle dynamics provides a reliable prediction of the vehicle's response without introducing the complexity of a Multi-Body model: this simplicity leads to a simulation time faster than the real one making 14 d.o.f. models suitable for implementation as on-board status observer [1,2,3] or for hardware in the loop tests [4,5]. The Mechanical Department of Politecnico di Milano together with Pirelli Tyres developed a 14 d.o.f. model named VDSIM, acronym of Vehicle Dynamics SIMulator, in Matlab/Simulink environment aiming at providing a tool for fast and reliable simulations where vehicle's main characteristics could be easily modified to investigate their influence on dynamic response. The research activity was carried out inside the EC founded project VERTEC, acronym for VEhicle, Road, Tyre and Electronic Control systems interaction

This work provides a description of the basic equations of the model and of the modelling of suspensions, brake system and driveline; steering angle, brakes pressure, throttle position and gear are considered as manoeuvre's input and could be either imposed by the user in pre-processing phase (open-loop manoeuvre) or computed by a model of the driver while the simulation is running (closed loop manoeuvre). VDSIM implements MFTyre '96 formulation [6] for the evaluation of the contact forces. Results of typical handling manoeuvres simulated with VDSIM and relevant to two vehicles are compared with those provided by Multi-Body models developed with the commercial code ADAMS\Car. A comparison between the output of VDSIM simulation and experimental measurement obtained in outdoor tests is eventually presented.

Keywords: 14 d.o.f. vehicle model, real-time simulation, experimental validation

1 INTRODUCTION

Mechanical Department of Politecnico di Milano in cooperation with Pirelli Tyre System Department developed a numerical model named VDSIM, acronym for "Vehicle Dynamic SIMulator": this activity was carried out as a task of the EC founded VERTEC Project; the aim of this project is to improve the active vehicle safety developing an integrated model for the simulation of the road-tyre-vehicle-driver system in the most dangerous situations.

Contact author: Stefano Melzi

Via La Masa 34, 20158 Milano, Italy

VERTEC project puts together the knowledge of several Partners: vehicle manufacturers (Porsche, CRF, VOLVO), tyres manufacturers (Pirelli, Nokian), Universities (Università degli studi di Firenze, Helsinki University of Technology), control logic manufacturers (Lucas Varity GmbH), road maintenance experts (CETE), transport research organisations (TRL, VTI).

The purposed vehicle model was designed for the analysis of the dynamic behaviour of a car vehicle and of its interaction with active control systems. Considering this last application, the model was developed in MATLAB/Simulink, particularly suitable for the modelling of electronic components. Moreover the need of real-time simulation for HIL application ([4,5]) drove the choice towards a 14 d.o.f. model, this last offering the best compromise between precision and computational time. For

all this applications, the contribution of the VERTEC partners was essential: VDSIM model was developed to be compatible with ECS (Electronic Control Systems) (TRW) and with a road-tyre interaction model (UNIFI). Moreover, thanks to the huge amount of tests performed during the project (HUT, Nokian, CRF, TRL), the VDSIM reliability could be verified.
In a 14 d.o.f. model the vehicle is be schematically considered as composed by two subsystems: the sprung mass represented by the rigid chassis (indicated also with as vehicle's body) having 6 d.o.f., and the unsprung masses (four wheels) each one characterised by a rolling motion and a vertical travel relative to the chassis; the suspension system connects the two subsystems dictating both the path of relative motion and the exchanged forces. The forces transmitted between the chassis and unsprug masses are described by means of a quasi-static characterisation of the front and rear suspension: a vehicle models developed with ADAMS/CAR, were used to extract the front and rear suspension virtual test-rig thus allowing to determine the forces transmitted to the chassis for different combination of wheel travels, steering angles and lateral contact forces. Variation of toe angle, camber angle, vehicle's track and displacement were also taken into account, together with the position of the roll and pitch axis.
Considering the possible interface with active control devices, which usually act on the brakes (ABS, VDC) on the differential and/or on the engine (TCS), the braking system (pipes, callipers, discs) and the engine, together with the driveline, were also modelled.
The first section of this paper reports a detailed description of the model, paying particular attention to the motion equations and to modelling of suspensions, brake system and driveline. Several comparisons between the results provided by VDSIM with those obtained with more complex ADAMS models are then presented and a validation against experimental data is eventually shown.

2 THE VEHICLE MODEL

2.1 LIST OF SYMBOLS

A list of the principal symbols used for reference frames, geometrical entities, forces and inertial parameters, is reported

X_A-Y_A-Z_A	Absolute reference frame
X_L-Y_L-Z_L	Moving reference frame
X-Y-Z	Local reference frame fixed on the body and centered in the body's c.o.g.
h_{pc}	Vertical distance between pitch centre and longitudinal axis of the vehicle X
x_{pc}	Longitudinal distance measured on axis X between body's c.o.g. and pitch centre
h_{rc}	Vertical distance between roll centre and longitudinal axis of the vehicle X
h_{bi}	Vertical distance between the *i-th* suspension dome and the pitch centre
h_{ri}	Vertical distance between the *i-th* suspension dome and the roll centre
x_{pa}	Longitudinal distance measured on axis X between the centre of aerodynamic actions and pitch centre
a_i	longitudinal distance between body's c.o.g. and *i-th* suspension dome measured in X-Y-Z reference
c_i	lateral distance between body's c.o.g. and i-th suspension dome measured in X-Y-Z reference (half track).
δ_i	Steer angle of the *i-th* wheel
F_{si}	Vertical suspension force relevant to the *i-th* suspension dome
F_{drag}	Aerodynamic drag force
F_{lift}	Aerodynamic lift force
M_{aer}	Aerodynamic pitch moment
C_{Wi}	Driving/braking torque acting on the *i-th* tire
F_{xi}	Longitudinal contact force of the *i-th* tire in the tire reference frame
F_{yi}	Lateral contact force of the *i-th* tire in the tire reference frame
M_{yi}	Roll resistance moment on the *i-th* tyre
M_{zi}	Self aligning torque of the *i-th* tire
m_b	Vehicle's body mass
J_{xxb}	Principal moment of inertia of the vehicle's body around X axis
J_{yyb}	Principal moment of inertia of the vehicle's body around Y axis
J_{zzb}	Principal moment of inertia of the vehicle's body around Z axis
$m_{u,i}$	i-th unsprung mass
$J_{u,i}$	i-th wheel rolling moment of inertia
J_e	global moment of inertia of engine and transmission

2.2 INDEPENDENT VARIABLES

The proposed model describes the vehicle dynamics through the following 14 d.o.f.:

- 6 d.o.f. for the rigid chassis;
- 4 d.o.f. for the vertical displacement ($z_{u,i}$);
- 4 d.o.f. for the rotations of the wheels ($\omega_{u,i}$).

All the d.o.f. can be collected into two vectors, $\overline{q}_b$ and $\overline{q}_u$, respectively relevant to the sprung mass (i.e. vehicle's body) and to the unsprung masses:

$$\overline{q} = \begin{Bmatrix} \overline{q}_b \\ \overline{q}_u \end{Bmatrix} = \begin{Bmatrix} \begin{bmatrix} x_{A,RC} & y_{A,RC} & z & \rho & \beta & \sigma \end{bmatrix}^T \\ \begin{bmatrix} z_{u,1} & \theta_{u,1} & z_{u,2} & \theta_{u,2} & z_{u,3} & \theta_{u,3} & z_{u,4} & \theta_{u,4} \end{bmatrix}^T \end{Bmatrix} \quad (1)$$

where $x_{A,RC}$ and $y_{A,RC}$ respectively represent the absolute displacements of the vehicle roll centre in the horizontal plane, z is the absolute vertical displacement of the body's centre of gravity and are the rotations of the vehicle's body

around the tern X-Y-Z. Steer angle, brake pressure, throttle position and gear are all regarded as imposed inputs characterising a particular manoeuvre and they can be either introduced by the user in pre-processing phase or computed during the simulation by a driver model.
While the meaning of vector $\overline{q}_u$ is quite immediate, (it simply collects the absolute vertical displacement and the rotations along the local pitch axis of each wheel), the terms belonging to vector $\overline{q}_b$ need to be explained with more details.
As shown in Figure 1, an absolute reference, X_A-Y_A-Z_A is introduced: Z_A is assumed parallel to the direction of acceleration of gravity.
The large displacement of the body is described through a moving reference identified by the axes X_L-Y_L-Z_L; as presented in Figure 1, the origin of the moving reference is fixed in a point (RC) belonging to the roll axis placed below the body c.o.g. (point G). At present development stage the model assumes that the motion of local reference takes place in the plane X_A-Y_A, that is longitudinal or lateral slopes of the road are neglected.

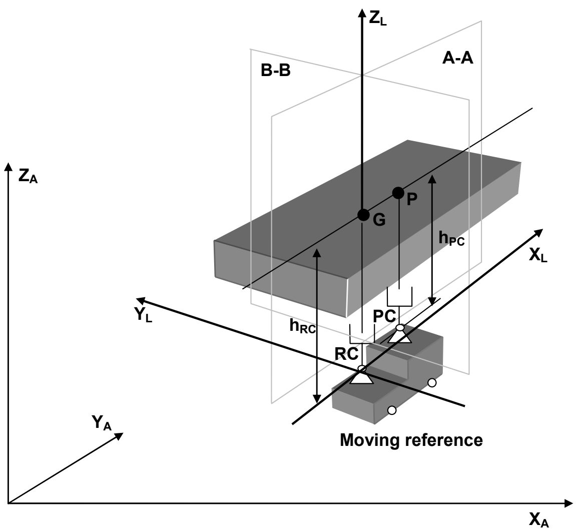

Figure 1 Reference frames adopted for vehicle motion description.

The moving reference can be considered as a sort of moving platform carrying the body's roll centre (RC) and the body's pitch centre (PC) whose height from the ground is assumed to be constant. The body is constrained to follow the absolute translations and the yaw angle of the moving platform in the horizontal plane (X_A-Y_A). The large displacement of the body is thus represented by the absolute translations of the vehicle roll centre in the horizontal plane ($X_{A,RC}$ and $Y_{A,RC}$) and by the moving reference yaw angle σ.
Small displacements of the body are assumed to take place with respect to the moving reference; the vertical motion of the body is taken into account through the coordinate z in vector $\overline{q}_b$: z represents the distance of point P of Figure 1 from the ground along the vertical axis. Rotations along the pitch centre (β, Figure 2) and the roll centre (ρ, Figure 3) are also considered; according to the previous description of the moving reference, roll rotations take place around X_L axis while pitch rotations take place around an axis parallel to Y_L and passing through the pitch centre PC.

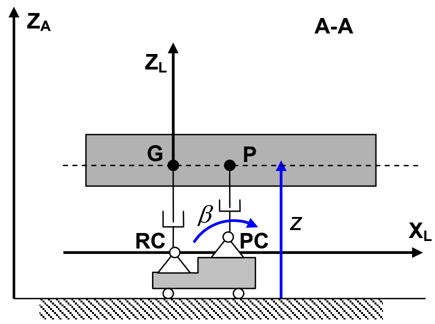

Figure 2 Degrees of freedom in the local longitudinal plane: P absolute vertical position z, and pitch angle β around pitch centre PC.

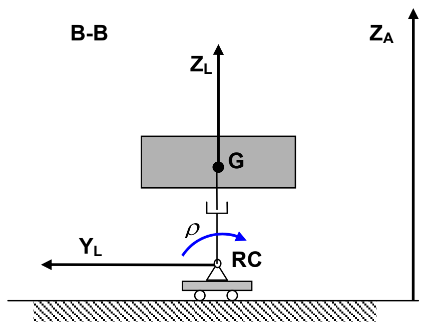

Figure 3 Degrees of freedom in the local longitudinal plane: roll angle ρ around roll centre RC.

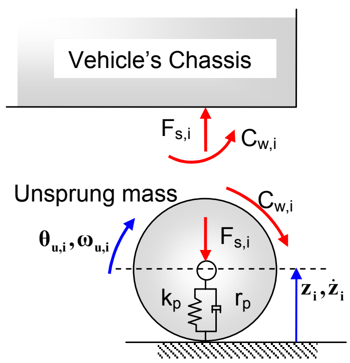

Figure 4 Interface between sprung and unsprung masses.

Vectors, $\overline{q}_b$ and $\overline{q}_u$ (equation (1)) collect the independent variables of the sprung and unsprung masses respectively; the motion equations for the two subsystems are reported in (2):

$$\begin{cases} [\mathbf{M}_b]\ddot{\overline{q}}_b = \overline{F}_{nlb} + \overline{F}_{sb} + \overline{C}_{wb} + \overline{F}_{db} \\ [\mathbf{M}_u]\ddot{\overline{q}}_u = \overline{F}_{nlu} + \overline{F}_{su} + \overline{C}_{wu} + \overline{F}_{du} \end{cases} . \qquad (2)$$

The term [$\mathbf{M}_b$] in the first equation, represents the mass matrix of the vehicle's body; vector $\overline{F}_{nlb}$ contains non linear inertial terms acting on the body. The term $\overline{F}_{sb}$ collects the generalised forces acting on the sprung mass generated by the suspensions travel. Actually the vehicle's chassis exchanges also longitudinal and lateral forces with the unsprung masses but the energy introduced by these components due to variation in vehicle's track and displacement is neglected, so these actions are considered as internal forces of a rigid body. $\overline{F}_{sb}$ is function of both the position of the chassis and of the unsprung masses (quasi-static characterisation of the suspensions) but also of their speeds, since the presence of dumpers is taken into account. The term $\overline{C}_{wb}$ is referred to the generalised force generated by the braking/driving torques applied at the vehicle's tyre. The term $\overline{F}_{db}$ collects the effect of aerodynamic forces, weight and of those tyre contact forces directly acting on the chassis d.o.f.; these terms are functions of tire slippages, slip angles, camber angles and thus they depend on the motion of the chassis and of the unsprung masses and on the values of steer angle which can be direct function of time.
In the second equation of (2) [$\mathbf{M}_u$] represents the mass-matrix for the unsprung masses; $\overline{F}_{nlu}$ is the vector containing the non linear inertial forces acting on the unsprung masses. $\overline{F}_{su}$ collects the generalised forces on the unsprung masses generated by suspensions' travel. Vector $\overline{C}_{wu}$ contains the generalised force relevant to the wheel's rotation due to the braking/driving torques applied at the vehicle's tyre. $\overline{F}_{du}$ collects the effect of those contact forces (rolling resistance torque, longitudinal contact force) which act on tyres' rotation, together with unsprung mass weight and the viscous-elastic force developed by the contact spring-damper element. The motion equations for the sprung and unsprung masses are derived according to Lagrange formulation:

$$\begin{aligned} \frac{d}{dt}\left(\frac{\partial T}{\partial \dot{\overline{q}}_b}\right) - \left(\frac{\partial T}{\partial \overline{q}_b}\right) = \overline{Q}_b \\ \frac{d}{dt}\left(\frac{\partial T}{\partial \dot{\overline{q}}_u}\right) - \left(\frac{\partial T}{\partial \overline{q}_u}\right) = \overline{Q}_u \end{aligned} \qquad (3)$$

where T represents the kinetic energy while $\overline{Q}_b$ and $\overline{Q}_u$ vectors collect the virtual work of the external forces acting respectively on the vehicle's body and on the unsprung masses. Motion equation of the system are derived according to the following hypothesis:

- the inertial matrix of the body is assumed to be diagonal in a reference system X-Y-Z fixed to the body and centered in the body's c.o.g. (Figure 5);
- roll and pitch angles of the chassis are supposed to be small enough to be considered independent one from the other;
- as a consequence the chassis motion is studied independently in the three different planes: X_L-Y_L plane (yaw angle); X_L-Z_L plane (pitch and c.o.g. longitudinal displacement); Y_L-Z_L plane roll and lateral c.o.g. displacement.

As far as the unsprung masses is concerned, the following hypothesis are made:

- kinetic energy associated with both camber rotation and steering angle is supposed to be negligible;
- gyroscopic effects on the wheels are neglected.

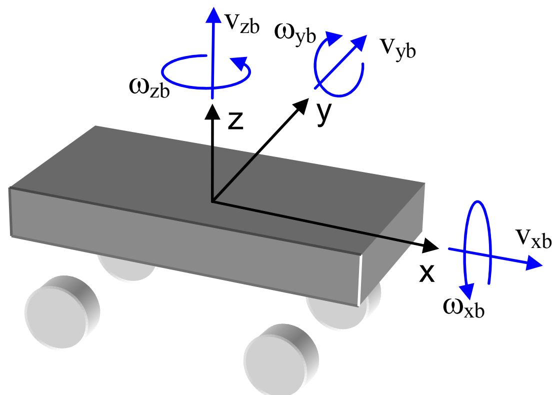

Figure 5 Local reference frame X-Y-Z.

3.1 KINETIC ENERGY OF THE SYSTEM

3.1.1 Chassis's kinetic energy

It should be noticed that vertical travel of the wheel is the unique relative displacement allowed between chassis and unsprung masses; this means that the longitudinal and lateral displacement of the unsprung mass in the X_L-Y_L plane (Figures 1, 2, 3) are supposed to take place as the unsprung mass was fixed to the chassis. According to this consideration, the kinetic energy of the sprung mass can be written down as follows:

$$T_b = \frac{1}{2}\begin{Bmatrix} V_{xb} \\ V_{yb} \\ V_{zb} \\ \omega_{xb} \\ \omega_{yb} \\ \omega_{zb} \end{Bmatrix}^T \begin{bmatrix} m_b & 0 & 0 & 0 & 0 & 0 \\ 0 & m_b & 0 & 0 & 0 & 0 \\ 0 & 0 & m_b & 0 & 0 & 0 \\ 0 & 0 & 0 & J_{xxb} & 0 & 0 \\ 0 & 0 & 0 & 0 & J_{yyb} & 0 \\ 0 & 0 & 0 & 0 & 0 & J_{zzb} \end{bmatrix} \begin{Bmatrix} V_{xb} \\ V_{yb} \\ V_{zb} \\ \omega_{xb} \\ \omega_{yb} \\ \omega_{zb} \end{Bmatrix} + \sum_{i=1}^{4} \frac{1}{2} \begin{Bmatrix} V_{xu} \\ V_{yu} \end{Bmatrix}^T \begin{bmatrix} m_{u,i} & 0 \\ 0 & m_{u,i} \end{bmatrix} \begin{Bmatrix} V_{xu} \\ V_{yu} \end{Bmatrix} \tag{4}$$

Equation (4) is referred to the kinetic energy expressed as function of the physical variables of the system: body's c.o.g. velocities and angular speeds and unsprung masses velocities in the X-Y-Z reference (Figure 5). The first term of (4) accounts for the kinetic energy of the chassis (both traslational and rotational) and the second is relevant to the traslation of the unsprung masses in the X-Y plane.
Kinetic energy should now be expressed as function of the system d.o.f.; for this purpose an auxiliary vector $\dot{\bar{x}}_b$ can be defined:

$$\dot{\bar{x}}_b = \begin{Bmatrix} \dot{x}_{L,RC} \\ \dot{y}_{L,RC} \\ \dot{z} \\ \dot{\rho} \\ \dot{\beta} \\ \dot{\sigma} \end{Bmatrix} = \begin{bmatrix} \cos\sigma & \sin\sigma & 0 & 0 & 0 & 0 \\ -\sin\sigma & \cos\sigma & 0 & 0 & 0 & 0 \\ 0 & 0 & 1 & 0 & 0 & 0 \\ 0 & 0 & 0 & 1 & 0 & 0 \\ 0 & 0 & 0 & 0 & 1 & 0 \\ 0 & 0 & 0 & 0 & 0 & 1 \end{bmatrix} \begin{Bmatrix} \dot{x}_{A,RC} \\ \dot{y}_{A,RC} \\ \dot{z} \\ \dot{\rho} \\ \dot{\beta} \\ \dot{\sigma} \end{Bmatrix} \tag{5}$$

In vector $\dot{\bar{x}}_b$ the RC absolute speeds are projected along the local reference X_L-Y_L; relation (5) can be rewritten as:

$$\dot{\bar{x}}_b = \left[\mathbf{h}_{\mathbf{A,L}}\right] \dot{\bar{q}}_b \,. \tag{6}$$

Assuming small pitch and roll rotations, the physical variables of the vehicle body (Figures 2, 3) can thus be expressed as function of vector $\dot{\bar{x}}_b$

$$\begin{Bmatrix} V_{xb} \\ V_{yb} \\ V_{zb} \\ \omega_{xb} \\ \omega_{yb} \\ \omega_{zb} \end{Bmatrix} = \begin{bmatrix} 1 & 0 & 0 & 0 & h_{PC} & 0 \\ 0 & 1 & 0 & -h_{RC} & 0 & 0 \\ 0 & 0 & 1 & 0 & x_{PC} & 0 \\ 0 & 0 & 0 & 1 & 0 & 0 \\ 0 & 0 & 0 & 0 & 1 & 0 \\ 0 & 0 & 0 & 0 & 0 & 1 \end{bmatrix} \begin{Bmatrix} \dot{x}_{L,RC} \\ \dot{y}_{L,RC} \\ \dot{z} \\ \dot{\rho} \\ \dot{\beta} \\ \dot{\sigma} \end{Bmatrix} = \left[\mathbf{\Lambda}_{\mathbf{xyb}}\right] \dot{\bar{x}}_b \tag{7}$$

$$\begin{Bmatrix} V_{xu,i} \\ V_{yu,i} \end{Bmatrix} = \begin{bmatrix} 1 & 0 & 0 & 0 & h_{bi} & -c_i \\ 0 & 1 & 0 & -h_{ri} & 0 & a_i \end{bmatrix} \begin{Bmatrix} \dot{x}_{L,RC} \\ \dot{y}_{L,RC} \\ \dot{z} \\ \dot{\rho} \\ \dot{\beta} \\ \dot{\sigma} \end{Bmatrix} = \left[\mathbf{\Lambda}_{\mathbf{xy}u,i}\right] \dot{\bar{\mathbf{x}}}_{\mathbf{b}} \tag{8}$$

Relations (7) and (8) link the physical variables (speed and angular velocities) to the vector $\dot{\bar{x}}_b$; combining equations (4), (6), (7) and (8), the kinetic energy can thus be expressed as function of the independent variables vector:

$$T_b = \frac{1}{2}\dot{\bar{q}}_b^T \left[\mathbf{h}_{\mathbf{A,L}}\right]^T \left[\mathbf{\Lambda}_{\mathbf{xyb}}\right]^T \begin{bmatrix} m_b & 0 & 0 & 0 & 0 & 0 \\ 0 & m_b & 0 & 0 & 0 & 0 \\ 0 & 0 & m_b & 0 & 0 & 0 \\ 0 & 0 & 0 & J_{xxb} & 0 & 0 \\ 0 & 0 & 0 & 0 & J_{yyb} & 0 \\ 0 & 0 & 0 & 0 & 0 & J_{zzb} \end{bmatrix} \left[\mathbf{\Lambda}_{\mathbf{xyb}}\right]\left[\mathbf{h}_{\mathbf{A,L}}\right]\dot{\bar{q}}_b + \sum_{i=1}^{4}\frac{1}{2}\dot{\bar{q}}_b^T \left[\mathbf{h}_{\mathbf{A,L}}\right]^T \left[\mathbf{\Lambda}_{\mathbf{xy}u,i}\right]^T \begin{bmatrix} m_{u,i} & 0 \\ 0 & m_{u,i} \end{bmatrix} \left[\mathbf{\Lambda}_{\mathbf{xy}u,i}\right]\left[\mathbf{h}_{\mathbf{A,L}}\right]\dot{\bar{q}}_b = \frac{1}{2}\dot{\bar{q}}_b^T \left[\mathbf{M}_b\left(\bar{q}_b, \bar{q}_u\right)\right]\dot{\bar{q}}_b \tag{9}$$

3.1.2 Wheel's kinetic energy
Another term should be considered in the total kinetic energy which is associated with the wheels' rotations and vertical translations (Figure 4); if gyroscopic effects are neglected the following expression can be adopted:

$$T_u = \frac{1}{2}\begin{Bmatrix} \omega_{u,1} \\ \omega_{u,2} \\ \omega_{u,3} \\ \omega_{u,4} \\ \omega_e \end{Bmatrix}^T \begin{bmatrix} J_{u,1} & 0 & 0 & 0 & 0 \\ 0 & J_{u,2} & 0 & 0 & 0 \\ 0 & 0 & J_{u,3} & 0 & 0 \\ 0 & 0 & 0 & J_{u,4} & 0 \\ 0 & 0 & 0 & 0 & J_e \end{bmatrix} \begin{Bmatrix} \omega_{u,1} \\ \omega_{u,2} \\ \omega_{u,3} \\ \omega_{u,4} \\ \omega_e \end{Bmatrix} + \frac{1}{2}\begin{Bmatrix} V_{zu,1} \\ V_{zu,2} \\ V_{zu,3} \\ V_{zu,4} \end{Bmatrix}^T \begin{bmatrix} m_{u,1} & 0 & 0 & 0 \\ 0 & m_{u,2} & 0 & 0 \\ 0 & 0 & m_{u,3} & 0 \\ 0 & 0 & 0 & m_{u,4} \end{bmatrix} \begin{Bmatrix} V_{zu,1} \\ V_{zu,2} \\ V_{zu,3} \\ V_{zu,4} \end{Bmatrix} \tag{10}$$

where $J_{u,i}$ and J_e respectively represent the moment of inertia of the *i-th* wheel along the rotation axis and the moment of inertia of the engine and transmission elements. When the clutch is engaged the engine angular speed is function of the angular velocity of the wheel through the transmission and differential ratio τ_t; the link between the physical variables and the d.o.f. can thus be expressed as:

$$\begin{Bmatrix} \omega_{u,1} \\ \omega_{u,2} \\ \omega_{u,3} \\ \omega_{u,4} \\ \omega_e \end{Bmatrix} = \begin{bmatrix} 1 & 0 & 0 & 0 \\ 0 & 1 & 0 & 0 \\ 0 & 0 & 1 & 0 \\ 0 & 0 & 0 & 1 \\ \frac{1}{2\tau_t} & \frac{1}{2\tau_t} & 0 & 0 \end{bmatrix} \begin{Bmatrix} \dot{\theta}_{u,1} \\ \dot{\theta}_{u,2} \\ \dot{\theta}_{u,3} \\ \dot{\theta}_{u,4} \end{Bmatrix} = \left[\Lambda_u\right] \begin{Bmatrix} \dot{\theta}_{u,1} \\ \dot{\theta}_{u,2} \\ \dot{\theta}_{u,3} \\ \dot{\theta}_{u,4} \end{Bmatrix}$$

$$\begin{Bmatrix} V_{zu,1} \\ V_{zu,2} \\ V_{zu,3} \\ V_{zu,4} \end{Bmatrix} = \left[I\right] \begin{Bmatrix} \dot{z}_{u,1} \\ \dot{z}_{u,2} \\ \dot{z}_{u,3} \\ \dot{z}_{u,4} \end{Bmatrix} \tag{11}$$

and the kinetic energy associated with the unsprung masses becomes:

$$T_u=\frac{1}{2}\begin{Bmatrix}\dot\theta_{u,1}\\ \dot\theta_{u,2}\\ \dot\theta_{u,3}\\ \dot\theta_{u,4}\end{Bmatrix}^T[\mathbf{\Lambda_u}]^T\begin{bmatrix}J_{u,1}&0&0&0&0\\0&J_{u,2}&0&0&0\\0&0&J_{u,3}&0&0\\0&0&0&J_{u,4}&0\\0&0&0&0&J_e\end{bmatrix}[\mathbf{\Lambda_u}]\begin{Bmatrix}\dot\theta_{u,1}\\ \dot\theta_{u,2}\\ \dot\theta_{u,3}\\ \dot\theta_{u,4}\end{Bmatrix}+$$
$$+\frac{1}{2}\begin{Bmatrix}\dot z_{u,1}\\ \dot z_{u,2}\\ \dot z_{u,3}\\ \dot z_{u,4}\end{Bmatrix}^T\begin{bmatrix}m_{u,1}&0&0&0\\0&m_{u,2}&0&0\\0&0&m_{u,3}&0\\0&0&0&m_{u,4}\end{bmatrix}\begin{Bmatrix}\dot z_{u,1}\\ \dot z_{u,2}\\ \dot z_{u,3}\\ \dot z_{u,4}\end{Bmatrix}=\frac{1}{2}\dot{\bar q}_u^T[\mathbf{M_u}]\dot{\bar q}_u \quad (12)$$

3.1.3 Mass Matrix

The mass matrix of the system can thus be obtained assembling the matrices $[\mathbf{M}_b]$ and $[\mathbf{M}_u]$ according to the order of the independent variables (see equation (1)):

$$T=\frac{1}{2}\dot{\bar q}^T[\mathbf{M}_s(\bar q_b,\bar q_u)]\dot{\bar q}=\frac{1}{2}\begin{Bmatrix}\dot{\bar q}_b\\ \dot{\bar q}_u\end{Bmatrix}^T\begin{bmatrix}[\mathbf{M}_b(\bar q_b,\bar q_u)]&0\\0&[\mathbf{M}_u]\end{bmatrix}\begin{Bmatrix}\dot{\bar q}_b\\ \dot{\bar q}_u\end{Bmatrix} \quad (13)$$

The mass matrix $[\mathbf{M}_b]$ contains terms depending upon the vehicle's track and displacement which are function of the suspensions' travel (i.e. the relative motion between the chassis and the unsprung masses), and other terms determined by h_{RC} and h_{PC} varying with the independent variable z; the mass matrix $[\mathbf{M}_u]$ collects only constant terms.

$$\frac{d}{dt}\left(\frac{\partial T}{\partial\dot{\bar q}_b}\right)-\frac{\partial T}{\partial\bar q_b}=[\mathbf{M}_b]\ddot{\bar q}_b+[\dot{\mathbf{M}}_b]\dot{\bar q}_b-\frac{1}{2}\dot{\bar q}_b^T\frac{\partial[\mathbf{M}_b]}{\partial\bar q_b}\dot{\bar q}_b=[\mathbf{M}_b]\ddot{\bar q}_b-\bar F_{nlb}$$
$$\frac{d}{dt}\left(\frac{\partial T}{\partial\dot{\bar q}_u}\right)-\frac{\partial T}{\partial\bar q_u}=[\mathbf{M}_u]\ddot{\bar q}_u-\frac{1}{2}\dot{\bar q}_b^T\frac{\partial[\mathbf{M}_b]}{\partial\bar q_u}\dot{\bar q}_b=[\mathbf{M}_u]\ddot{\bar q}_u-\bar F_{nlu} \quad (14)$$

3.2 VIRTUAL WORK OF EXTERNAL FORCES

3.2.1 Vehicle's body

Sprung and unsprung masses can be regarded as two subsystems coupled by the actions transmitted by suspensions and by the driving/braking torques applied at the tires.

Focusing the attention on vehicle's body, Figure 6 and Figure 7 put into evidence the external forces acting on this subsystem respectively in the X_L-Y_L plane and in X_L-Z_L plane; since roll and pitch angles are assumed to be small, these planes almost overlap with X-Y and X-Z. The virtual work of external forces acting on vehicle's body can be written as reported in (15) where the generic terms $\delta^* S_j$ and $\delta^*\varphi_j$ respectively represents the virtual displacement and the rotation of the application point of the *j-th* force. List of symbols reported in 0 together with Figure 6 and Figure 7 may help to understand the meaning of each term.

$$\delta^* L_b=\begin{Bmatrix}\{F_{xi}\cos\delta_i-F_{yi}\sin\delta_i\}_{i=1\div4}\\ \{F_{xi}\sin\delta_i+F_{yi}\cos\delta_i\}_{i=1\div4}\\ \{M_{zi}\}_{i=1\div4}\\ \{F_{si}\}_{i=1\div4}\\ -m_b g\\ -F_{drag}\\ F_{lift}\\ -M_{aer}\\ \{C_{wi}\sin\delta_i\}_{i=1\div4}\\ \{-C_{wi}\cos\delta_i\}_{i=1\div4}\end{Bmatrix}^T\cdot\begin{Bmatrix}\{\delta^* S_{Fx,i}\}_{i=1\div4}\\ \{\delta^* S_{Fy,i}\}_{i=1\div4}\\ \{\delta^*\varphi_{Mzi}\}_{i=1\div4}\\ \{\delta^* S_{Fs,i}\}_{i=1\div4}\\ \delta^* S_{mg}\\ \delta^* S_{Fdrag}\\ \delta^* S_{Flift}\\ \delta^*\varphi_{Maer}\\ \{\delta^*\varphi_{Cwxi}\}_{i=1\div4}\\ \{\delta^*\varphi_{Cwyi}\}_{i=1\div4}\end{Bmatrix}=\bar F_b^T\cdot\delta^*\bar S_b \quad (15)$$

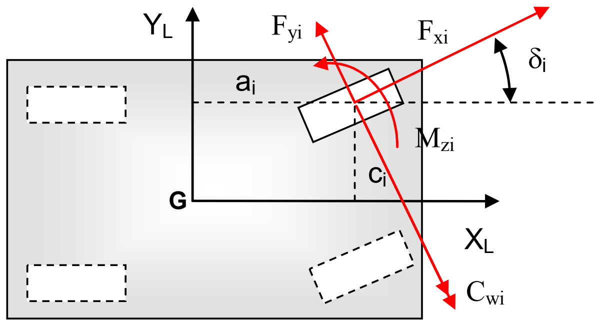

Figure 6 External forces transferred from the *i-th* tire to the vehicle's body in the X_L-Y_L plane.

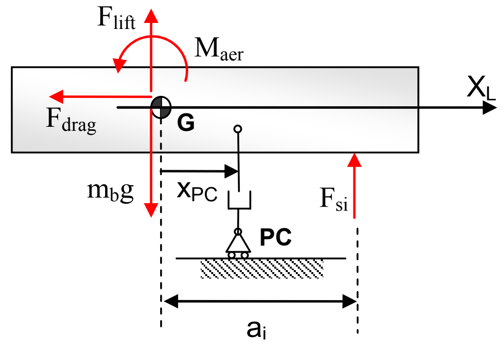

Figure 7 External forces acting on the vehicle's body in the X_L-Z_L plane.

Considering equation (5), an auxiliary vector $\delta^*\bar x_b$ can be profitably introduced:

$$\delta^*\bar x_b=[\mathbf{h}_{\mathbf{A,L}}]\delta^*\bar q_b \quad (16)$$

The following equation links the virtual displacements of the application points of external forces with the variables vector $\delta^*\bar x_b$:

$$\begin{Bmatrix} \{\delta^* S_{Fx,i}\}_{i=1\div4} \\ \{\delta^* S_{Fy,i}\}_{i=1\div4} \\ \{\delta^* \varphi_{Mz,i}\}_{i=1\div4} \\ \{\delta^* S_{Fs,i}\}_{i=1\div4} \\ \delta^* S_{mg} \\ \delta^* S_{Fdrag} \\ \delta^* S_{Flift} \\ \delta^* \varphi_{Maer} \\ \{\delta^* \varphi_{Cwx,i}\}_{i=1\div4} \\ \{\delta^* \varphi_{Cwy,i}\}_{i=1\div4} \end{Bmatrix} = \begin{bmatrix} [1] & 0 & 0 & 0 & \{h_{bi}\}_{i=1\div4} & \{-c_i\}_{i=1\div4} \\ 0 & [1] & 0 & \{-h_{ri}\}_{i=1\div4} & 0 & \{a_i\}_{i=1\div4} \\ 0 & 0 & 0 & 0 & 0 & [1] \\ 0 & 0 & [1] & \{c_i\}_{i=1\div4} & \{x_{PC}-a_i\}_{i=1\div4} & 0 \\ 0 & 0 & 1 & 0 & x_{PC} & 0 \\ 0 & 0 & 0 & 0 & h_{PC} & 0 \\ 1 & 0 & 1 & 0 & x_{PC} & 0 \\ 0 & 0 & 0 & 0 & 1 & 0 \\ 0 & 0 & 0 & [1] & 0 & 0 \\ 0 & 0 & 0 & 0 & [1] & 0 \end{bmatrix} \cdot \begin{Bmatrix} \delta x_{L,RC} \\ \delta y_{L,RC} \\ \delta z \\ \delta\rho \\ \delta\beta \\ \delta\sigma \end{Bmatrix} \quad (17)$$

Equation (17) should be written in a more compact form:

$$\delta^* \overline{S}_b = [\Lambda_{s,xb}] \delta^* \overline{x}_b \quad (18)$$

Combining (18) with (15) and (16), the virtual work of the external forces acting on the vehicle's body is expressed as follows:

$$\delta^* L_b = \overline{F}_b^T [\Lambda_{s,xb}] \cdot [\mathbf{h}_{\mathbf{A,L}}] \delta^* \overline{q}_b = \overline{Q}_b^T \delta^* \overline{q}_b \quad (19)$$

The explicit results of the matrix product allow to express the generalised forces vector $\overline{Q}_b$:

$$\overline{Q}_b = \begin{Bmatrix} 0 \\ 0 \\ \sum_{i=1}^{4} F_{si} \\ \sum_{i=1}^{4} F_{si} c_i \\ \sum_{i=1}^{4} F_{si}(x_{PC}-a_i) \\ 0 \end{Bmatrix} + \begin{Bmatrix} 0 \\ 0 \\ 0 \\ \sum_{i=1}^{4} C_{wi} \sin\delta_i \\ \sum_{i=1}^{4} -C_{wi}\cos\delta_i \\ 0 \end{Bmatrix} +$$

$$\begin{Bmatrix} \sum_{i=1}^{4}(F_{xi}\cos\delta_i - F_{yi}\sin\delta_i)\cdot\cos\sigma - \sum_{i=1}^{4}(F_{xi}\sin\delta_i + F_{yi}\cos\delta_i)\cdot\sin\sigma - F_{drag}\cos\sigma \\ \sum_{i=1}^{4}(F_{xi}\cos\delta_i - F_{yi}\sin\delta_i)\cdot\sin\sigma + \sum_{i=1}^{4}(F_{xi}\sin\delta_i + F_{yi}\cos\delta_i)\cdot\cos\sigma + F_{drag}\sin\sigma \\ -mg + F_{lift} \\ -\sum_{i=1}^{4}(F_{xi}\sin\delta_i + F_{yi}\cos\delta_i)\cdot h_{ri} \\ \sum_{i=1}^{4}(F_{xi}\cos\delta_i - F_{yi}\sin\delta_i)\cdot h_{bi} - mgx_{PC} + F_{lift}x_{PC} - F_{drag}h_{PC} \\ \sum_{i=1}^{4} M_{zi} - \sum_{i=1}^{4}(F_{xi}\sin\delta_i + F_{yi}\cos\delta_i)\cdot c_i + \sum_{i=1}^{4}(F_{xi}\sin\delta_i + F_{yi}\cos\delta_i)\cdot a_i \end{Bmatrix} \quad (20)$$

The previous expression can be written as:

$$\overline{Q}_b = \overline{F}_{sb} + \overline{C}_{wb} + \overline{F}_{db} \quad (21)$$

Equation (21) put into evidence the terms relevant to the suspension forces, the braking/drinving torques and the effect of aerodynamic forces, weight and of those tyre contact forces directly acting on the chassis d.o.f..

3.2.2 Unsprung mass

As far as the unsprung mass is concerned the situation is clearly reported in Figure 8: the torque C_{wi} directly acts on the wheel's rotation degree of freedom, exactly as the rolling resistance moment M_{yi}. The longitudinal contact force F_{xi} generates a torque on the same d.o.f.. The suspension force F_{si}, the unsprung mass weight $m_{u,i}g$ and the effect of the deformation of the spring-damper element that links the tire to the ground acts on the vertical displacement of the unsprung mass.

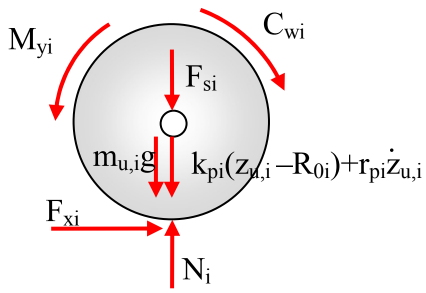

Figure 8 External forces acting on the unsprung mass.

The virtual work produced by these forces can be expressed as:

$$\delta^* L_{u,i} = \begin{Bmatrix} F_{xi} \\ M_{yi} \\ C_{wi} \\ -F_{si} \\ -m_{u,i}g \\ -k_{pi}(z_{u,i}-R_0) \\ -r_{pi}\dot{z}_{u,i} \end{Bmatrix} \cdot \begin{Bmatrix} \delta^* S_{Fx,i} \\ \delta^* \varphi_{Myi} \\ \delta^* \varphi_{Cwi} \\ \delta^* S_{Fsi} \\ \delta^* S_{mg,i} \\ \delta^* S_{k,i} \\ \delta^* S_{r,i} \end{Bmatrix} = \overline{F}_{u,i}^T \delta^* \overline{S}_{u,i} \quad (22)$$

where R_0 represents the unloaded radius while k_i and r_i are respectively the vertical stiffness and the vertical damping of the *i-th* tyre. The link between the displacements of the physical variables and the d.o.f. of a wheel is given by:

$$\delta^* S_{u,i} = \begin{Bmatrix} \delta^* S_{Fx,i} \\ \delta^* \varphi_{Myi} \\ \delta^* \varphi_{Cwi} \\ \delta^* S_{Fsi} \\ \delta^* S_{mg,i} \\ \delta^* S_{k,i} \\ \delta^* S_{r,i} \end{Bmatrix} = \begin{bmatrix} 0 & -z_{u,i} \\ 0 & 1 \\ 0 & 1 \\ 1 & 0 \\ 1 & 0 \\ 1 & 0 \\ 1 & 0 \end{bmatrix} \begin{Bmatrix} \delta^* z_{u,i} \\ \delta^* \theta_{u,i} \end{Bmatrix} = [\mathbf{\Lambda}_{\mathbf{\delta u.i}}] \delta^* \overline{q}_{u,i} \quad (23)$$

The generalised force vector $\overline{Q}_{ui}$ can be thus evaluated:

$$\delta^* L_{u,i} = \overline{F}_{u,i}^T [\Lambda_{\delta u,i}] \cdot \delta^* \overline{q}_{u,i} = \overline{Q}_{ui}^T \delta^* \overline{q}_{u,i} \quad (24)$$

$$\overline{Q}_{ui} = \begin{Bmatrix} -F_{si} \\ 0 \end{Bmatrix} + \begin{Bmatrix} 0 \\ C_{wi} \end{Bmatrix} + \begin{Bmatrix} k_i(R_0 - z_i) - r_i\dot{z}_i - m_i g \\ M_{yi} - F_{xi} z_i \end{Bmatrix} =$$

$$\overline{Q}_{u,i} = \overline{F}_{su,i} + \overline{C}_{wu,i} + \overline{F}_{du,i} \quad (25)$$

Equation (25) put into evidence the terms relevant to the suspension forces, the braking/drinving torques and the effect of contact forces directly acting on the *i-th* wheel.

3.3 SUSPENSION MODELLING

VDSIM model allows to take into account the presence of the suspension elements interposed between the sprung and unsprung masses. The forces developed by dampers are simply reproduced by considering the presence of shock absorbers, whose non-linear characteristics are introduced in the model, and computing at each integration step the relative speed between their extremities. A quasi-static characterisation of the suspension is adopted to describe the effect of the springs and of the related level-ratios produced by the suspension kinematics. The procedure to transfer the suspension characteristics to VDSIM was developed during the VERTEC project, using the fully validated Adams model for Lancia Lybra (task 5, *Development and validation of passenger car vehicle model*, Pirelli, Nokian, Porsche, CRF, TRW, HUT, UNIFI). This model was validated thanks to the tests performed during the project (task 3, *Reference tests with passenger cars + control systems*, Pirelli, Nokian, CRF, TRW, CETE, TRL, HUT).

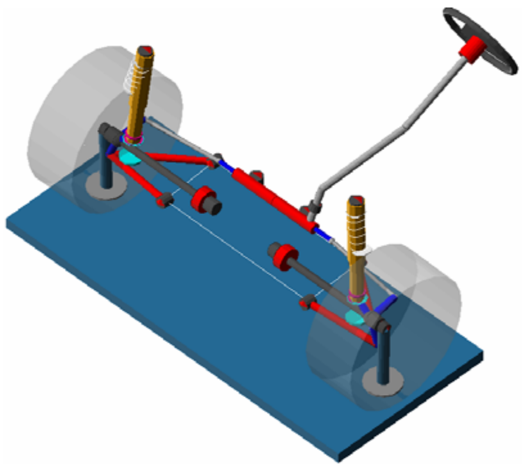

Figure 9 ADAMS Test-rig for the front suspension (Vertec, Development and validation of passenger car vehicle model).

ADAMS/Car virtual test-rig (Figure 9) was used to compute the forces transmitted from the suspensions to the chassis in quasi-static condition for several combinations of wheels vertical travels. In this "virtual" test-bench the vehicle's chassis is kept fixed to the ground, while it is possible to impose a vertical travel of each single wheel; the vertical force required to produce the movement of the wheel is computed thus allowing to obtain a quasi-static characterisation of the suspension. Front and rear suspensions where characterised independently: keeping fixed one of the two wheels (i.e. the one on the right side of the vehicle) and moving the other one in quasi-static condition two tables were generated, allowing to estimate the vertical force transmitted to the chassis by the left and right suspension for a generic shaking condition. The adopted approach allows to consider the presence of anti-roll bar or dependent suspensions systems. The effect of the steering angle was included in the characterisation of the front axis, so that the table relevant to the front axis presents three inputs (left and right wheel vertical travel and steering position).

Camber and toe angle also depend on the suspension's shaking, forces and torques acting on the hub; hence, the test-rig was used also to obtain two tables for each wheel providing the toe angle and the camber angle variations produced by the longitudinal and lateral contact force, overturning moment, suspension's shaking and steering angle. In this case the mutual reliance between the left and right suspension is neglected, in order to avoid the excessive increase of computational time.

3.4 ENGINE AND BRAKING SYSTEMS MODELS

In order to simulate a generic manoeuvre VDSIM requires as inputs the time histories of: steering angle, throttle position, brakes pressure, gear and clutch. According to this approach models of the driveline, (i.e. engine, clutch, gear box and differential), and of the braking system were implemented.

The engine was modelled by simply considering two torque curves, both depending on the engine angular speed and experimentally determined for steady state condition: they are respectively relevant to the throttle valve fully opened (T_{MAX}) and to the throttle valve completely closed (T_{MIN}). Assuming that the engine is always operating nearly a steady state condition, the engine torque for a given angular speed and a throttle valve position is obtained through linear interpolation. The current engine rotational speed is derived from the wheel rotational speed considering the gear (τ_{GEAR}) and differential (τ_{DIFF}) ratio. The engine torque is thus determined:

$$T_{MOT} = \frac{(T_{MAX} - T_{MIN}) \cdot f + T_{MIN}}{\tau_{GEAR} \cdot \tau_{DIFF}} \cdot \eta \tag{26}$$

where *f*, represents the position of the throttle valve, η the efficiency of both the gear-box and of the differential. The engine torque is applied at each wheel depending on the differential mounted on the vehicle.

As far as the braking system is concerned, brake pressure demand required at the tandem master cylinder is considered as an input for the model; the pressure build-up time, due to fluid compressibility, brakes response delay, brakes pad deformation, is introduced by means of a second order transfer function:

$$\frac{\overline{p_f}(s)}{p_f(s)} = \frac{1}{\tau_1^2 s^2 + \tau_2 s + 1} \tag{27}$$

where p_f is the pressure required by the tandem master cylinder (a manoeuvre input) while $\overline{p_f}(s)$ represents the pressure acting in the front brakes callipers and τ_1, τ_2 are two time constants of the brake system. The pressure acting on the rear wheels is obtained by scaling $\overline{p_f}(s)$ according to the rear-to-front weight shift curve. The brake torque acting on each single wheel can thus be computed according to a simplified formulation:

$$\overline{p_f} = \frac{T_b}{2 \cdot \mu \cdot A \cdot R} \tag{28}$$

where μ is the friction coefficient between brake disc and brake pad; R is the of the brake disk and A is the equivalent area of the brake piston.

4 ADAMS CAR-VDSIM COMPARISON

A first check of the precision of VDSIM in reproducing the vehicle's response was obtained through a comparison with the results provided by the ADAMS/Car reference model. Two models developed in ADAMS/Car were used: the first one is relevant to a segment C car; the second is relevant to a segment D car (VERTEC project, Task 5). Both the models describe the car dynamics with about 100 d.o.f., mainly distributed among the suspensions' arms. The comparison between VDSIM and ADAMS/Car was carried out considering a series of standard open loop manoeuvres: step steer, swept sine steer, double lane change. The time histories of the steer angle and of the throttle position were imposed to VDSIM and ADAMS/Car model.

Results presented in Figures 10-13 are referred to a swept sine steer manoeuvre carried out with the segment C car at a speed of 70 km/h with a steering amplitude of 45° with the steering frequency increasing from 0 to 2 H.

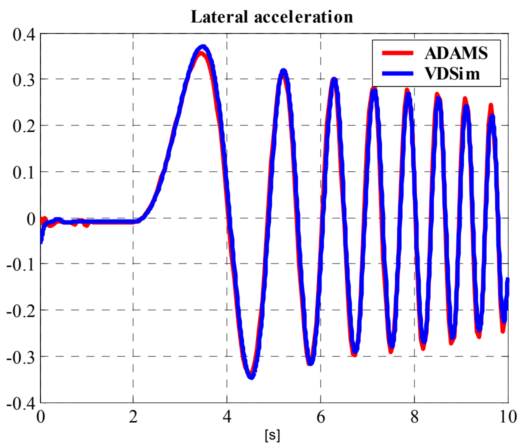

Figure 10 VDSIM VS ADAMS: lateral acceleration in a swept-sine steer steer manoeuvre carried out with segment C car.

This manoeuvre allows to evaluate the model response in the linear range; Figure 10 is relevant to the lateral acceleration obtained with the two simulation codes: the results present a negligible relative error exactly as the ones referred to the yaw rate reported in Figure 11.

Figure 12 presents the time histories of the normal contact forces, showing again a with a slight overestimation of the amplitude at low frequencies (1 Hz) and a slight underestimation at about 2 Hz.

The comparison between the front lateral contact forces obtained with ADAMS and VDSIM, reported in Figure 13 appears instead very satisfying for all the frequencies.

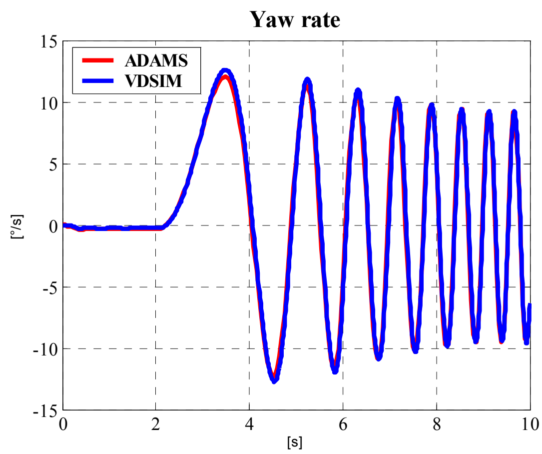

Figure 11 VDSIM VS ADAMS: lateral acceleration in a swept-sine steer steer manoeuvre carried out with segment C car.

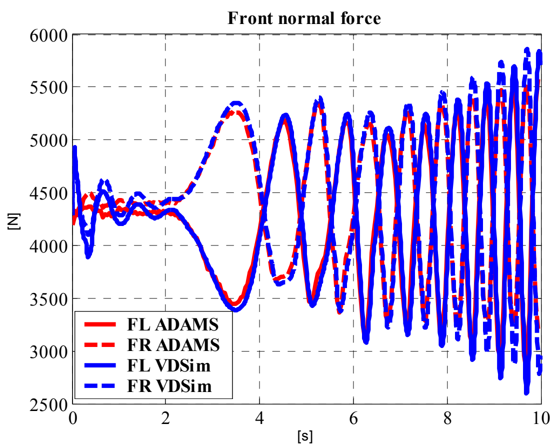

Figure 12 VDSIM VS ADAMS: normal contact forces on the front tyres in a swept-sine steer manoeuvre carried out with segment C car

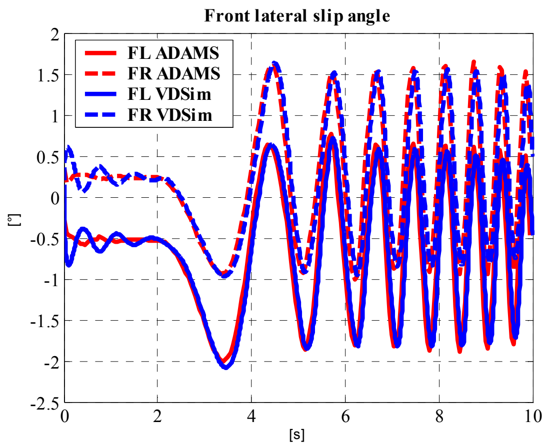

Figure 13 VDSIM VS ADAMS: slip angles on the front tyres in a swept-sine steer manoeuvre carried out with segment C car.

Figures 14-17 are relevant to 90-degree step steer manoeuvre carried out at 80 km/h with the segment D car. Figure 14 presents the time history of the lateral acceleration which reaches a value of 0.65 g; as can be noticed the curves obtained with ADAMS and VDSIM almost overlap.

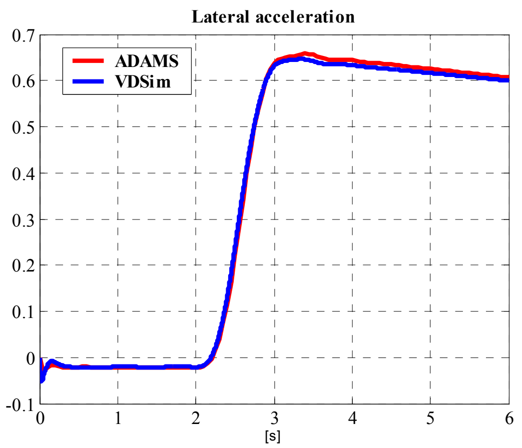

Figure 14 VDSIM VS ADAMS: lateral acceleration in a step-steer manoeuvre carried out with segment D car (VERTEC)

Figure 15 is referred to the yaw rate: again the values are very similar with a maximum difference of about 0.2 °/s.
Figure 16
Figure 16 reports the lateral forces on the front wheel resulting from the step-steer manoeuvre simulated with the two models; the time histories show a underestimation for the right wheel and a overestimation for the left wheel. The maximum error is around 7%. As last, Figure 17 shows the lateral force registered on the rear wheels with the two models.

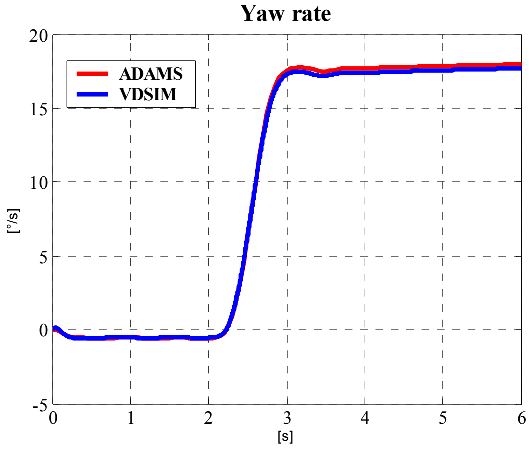

Figure 15 VDSIM VS ADAMS: yaw speed in a step-steer manoeuvre carried out with segment D car (VERTEC)

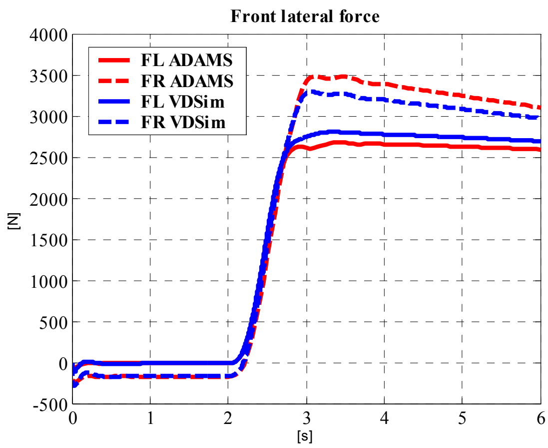

Figure 16 VDSIM VS ADAMS: lateral contact forces on the front tyres in a step steer with segment D car (VERTEC)

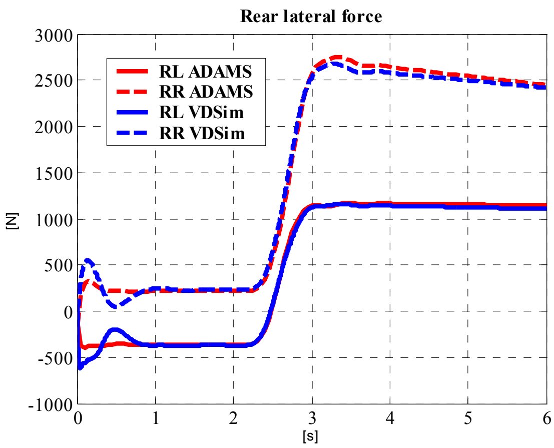

Figure 17 VDSIM-ADAMS: lateral contact forces on the rear tyres in a step steer manoeuvre carried out with segment D car (VERTEC)

5 EXPERIMENTATION-VDSIM COMPARISON

In order to get a full validation of VDSIM model, a comparison with the data collected during an experimental campaign on the segment D car, is presented. Several manoeuvres were carried out on Pirelli's test track in Vizzola Ticino for VERTEC project. The validation of the model was performed during the VERTEC project, thanks to several tests performed by the partners in very several conditions: dry asphalt, wet asphalt, ice ad snow.
The car was instrumented with the following measuring devices:

- An inertial platform was mounted in proximity of the vehicle's c.o.g. allowing to measure the 3 components of accelerations along the longitudinal, lateral and vertical axis, together with the 3 components of angular speed;
- Four inductive wheel speed sensor (used by ABS);
- Steering angle Hall IC sensor (used by VDC).

Signals used by VDC and ABS control systems were acquired by accessing to the CAN bus system. The collected data allowed to measure reference quantities (lateral acceleration, yaw speed) for the model validation together with input data (steering angle time histories) necessary to reproduce the same manoeuvres with VDSIM. Since no data concerning throttle position were available the manoeuvres were carried out in two conditions: in the first one the throttle position was kept fixed by the driver; in the second one the accelerator was released during the manoeuvre execution. VDSIM is able to compute the throttle position required to reach and maintain the vehicle's speed in the first part of the manoeuvre; then during the manoeuvre's execution the throttle position can be kept fixed or the accelerator can be released. This feature allowed to numerically reproduce the experimental manoeuvre in open loop even if the throttle position was not acquired during the tests.
The manoeuvres were carried out with the vehicle mounting *Pirelli P7 195/65 R15* tyres; MFTyre '96 parameters for these tyres were identified through a test session on an MTS flat track machine.
As example Figures 18-20 report comparisons between the model results and the experimental ones, relevant to a double lane change manoeuvre executed according to the ISO 3833 specifications. The manoeuvre is carried out at a speed of 90 km/h on dry asphalt.
Figure 18 shows the experimental lateral acceleration superposed to the one produced by VDSIM simulation the comparison put into evidence a good reproduction of the experimental data (maximum error 0.6 m/s^2).

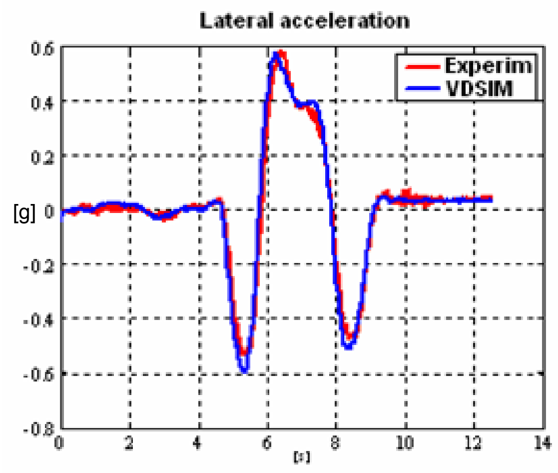

Figure 18 VDSIM VS Experimental: lateral acceleration in double lane change manoeuvre carried out with segment D car (VERTEC)

Also the results obtained for the yaw speed (Figure 19) put into evidence a good reproduction of the vehicle's dynamic behaviour with a maximum deviation from the measured signal of about 2.5 °/s registered in the central phase of the manoeuvre.

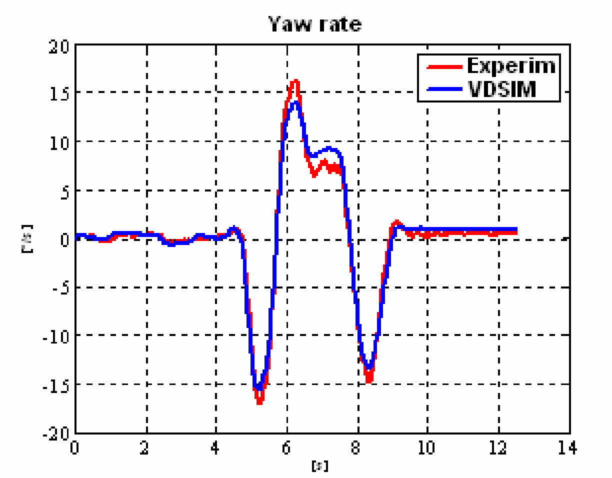

Figure 19 VDSIM VS Experimental: yaw speed in double lane change manoeuvre carried out with segment D car (VERTEC).

As last, Figure 20 reports the comparisons relevant to the roll speed: the results can be considered again satisfying; the higher harmonic content presents in the measured signal is due to the irregularity of the road surface which was not included at present development stage of the model.

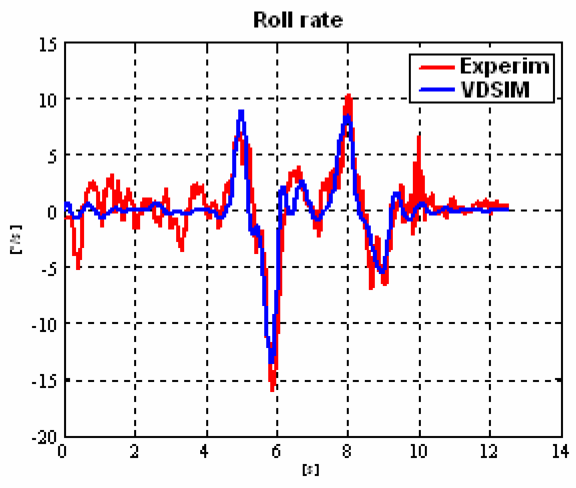

Figure 20 VDSIM-Experimental: roll speed in double lane change manoeuvre carried out with segment D car (VERTEC).

CONCLUSIONS

Politecnico di Milano and Pirelli Tyres cooperated in the development of a 14 d.o.f. model for car vehicles named VDSIM. The activity was carried out with important contributions from all the partners of EC founded VERTEC project (Nokian, Porsche, CRF, Volvo, CETE, VTI, TRL, UNIFI, HUT, TRW). The task of the vehicle model is to combine a precise prediction of the vehicle's dynamic response with a fast simulation time thus allowing to introduce the model in HIL test-rigs ([4,5]) or to use VDSIM as an on-board status observer ([1,2,3]). The need of interface with electronic devices pushed to develop VDSIM in Matalab/Simulink environment which is particularly suitable for the modelling of electronic components.

In this paper the motion equations of VDSIM were revealed and a detailed description for the modelling of suspensions, engine, driveline and brake system was provided. Two car vehicles were modelled with VDSIM and the numerical results relevant to open-loop manoeuvres were compared with those provided by two ADAMS models of the same vehicles, each one using about 100 d.o.f.. The comparison showed that VDSIM is able to reproduce in a very satisfying way the behaviour of a more complex MB model in terms of lateral acceleration, yaw speed, contact forces and slip angles. The final comparison with experimental data collected in outdoor tests revealed how VDSIM model provides a precise prediction of the vehicle's response.

ACKNOWLEDGEMENTS

The authors would greatly acknowledge the European Community for having founded this research and all the other partners of the VERTEC project (VEhicle, Road, Tyre and Electronic Control systems interaction) Nokian, Porsche, CRF, Volvo, HUT, UNIFI, TRW, CETE, VTI, TRL

REFERENCES

[1] Best M.C., Gordon T.J., Dixon P.J., An Extended Adaptive Kalman Filter for Real-time State Estimation of Vehicle Handling Dynamics. *Vehicle System Dynamics*, 34, pp. 57-75, 2000.

[2] Kiencke U., Daiß A. Observation of Lateral Vehicle Dynamics. *Control Eng. Practice*, Vol. 5, No. 8, pp. 1145-1150, 1999.

[3] Fukada Y., Estimation of Vehicle Slip-angle with Combination Method of Model Observer and Direct Integration. *Proceedings of AVEC'98*, pp. 201-206, 1998.

[4] Cheli F., Giangiulio E., Mauri M., A mechatronic test bench for ABS control system. *Symposium on Power Electronics, Electrical Drives, Automation & Motion SPEEDAM2004*, Capri, Italy, June 16-18, 2004.

[5] Castignani L., Cheli F., Giangiulio E., Mauri M., A hil approach for ABS performance evaluation. *International Conference on Integrated Chassis Control*, Naples, Italy, November 10-12, 2004.

[6] Pacejka H.B., Besselink I.J., *MF-Tyre User Manual. A Design and Analysis Tool for Modelling and Simulation of Tyre Behaviour*. DELFT Tyre, 1996.

ISSN 1590-8844
International Journal of Mechanics and Control, Vol. 06, No. 02, 2005

FRACTAL RULES OF MIXTURE FOR MULTI-SCALE FRAGMENTATION OF HETEROGENEOUS MATERIALS

Alberto Carpinteri, Nicola Pugno

Department of Structural Engineering, Politecnico di Torino
Corso Duca degli Abruzzi 24, 10129 Torino, Italy

ABSTRACT

We propose a new approach to study the fragmentation of heterogeneous materials. It extends the fragmentation laws, deduced for homogeneous materials, to mixtures. As a practical application, we focus our attention onto artificial fragmentation by drilling of reinforced concrete in different re-bar configurations.

Keywords: fractal, fragmentation, rules of mixture, drilling, cutting

1 INTRODUCTION

Fragmentation and comminution theories have been extensively used to describe a variety of phenomena in different scientific areas [1-4]. The complexity involved in the process, due to multi-cracking interaction and propagation at different length scales, forces us to follow the process from a statistical point of view. The main parameter describing fragmentation from a global point of view can be considered the energy dissipated in the process. This statistical and energy approach has permitted to obtain universal laws for the evaluation of energy dissipation in multi-scale fragmentation due to impact or explosion [1]. The present paper extends the mentioned approach to heterogeneous materials.

Fragmentation and comminution [5] play an important role both in natural and man-made processes. Star explosion and meteor impact are examples of natural phenomena producing fragmented ejecta. Although fragmentation is of considerable importance and many experimental, numerical and theoretical studies have been carried out, relatively little progress has been made till now in developing related comprehensive theories. Fragmentation involves the interaction between fractures over a wide range of scales and a fractal fragment size distribution is expected [6].

Fractals are hierarchical, self-similar and in some cases highly irregular objects [7, 8]. As a result, no matter how complex a particular spatial pattern might be, the statistical properties of this pattern can be reproduced at different length scales. Such scale-invariant systems offer new opportunities for modelling the propagation of multiple fractures at different length scales.

Because of their complexity at any given scale, they are applicable to multiscale heterogeneous materials.

Fragmentation can occur as a result of dynamic crack propagation during compressive/tensile loading (dynamic fragmentation) or due to stress waves and their reflections during impact loading (ballistic fragmentation). These processes have been reviewed in [9-12]. Many models have been proposed to link fractals to fracture and fragmentation [13-39].

In the present paper, we propose a new approach to study the fragmentation of heterogeneous materials. It extends the fragmentation laws [1, 2], deduced for homogeneous materials and unifying the three well-known comminution theories [40-42], to mixtures. As a practical application, we have focused our attention onto artificial fragmentation by drilling of reinforced concrete. Substantially, the paper represents the conclusion of the drilling analysis proposed in [2].

2 FRACTAL FRAGMENTATION OF HETEROGENEOUS MATERIALS

The power dissipation $\dot{W}$, during the multi-scale fragmentation of a volume per unit time $\dot{V}$, for a homogeneous material can be described as [1-4]:

$$\dot{W} = \Gamma \dot{V}^{\gamma}, \qquad (1)$$

where Γ is the so-called fractal fragmentation strength (a size-independent parameter) and γ the fractal exponent, comprised between 2/3 and 1.

Contact authors: Alberto Carpinteri and Nicola Pugno,

alberto.carpinteri@polito.it

nicola.pugno@polito.it

For a heterogeneous material, the power dissipation for each phase *i* can be obtained from eq. (1):

$$\dot{W}_i = \Gamma_i \dot{V}_i^{\gamma_i} \, . \tag{2}$$

Since γ_i should be only slightly depending on the phase *i*, we can assume $\gamma_i \approx \gamma, \quad \forall i$, so that:

$$\dot{W}_i = \Gamma_i \dot{V}_i^{\gamma} \, . \tag{3}$$

The last hypothesis is necessary to homogenise the mixture.

3 CLASSICAL RULES OF MIXTURE

A classical fragmentation process is described by eq. (3) for $\gamma = 1$. In this case, the energy dissipation occurs in a volume. The fractal drilling strength Γ becomes the usual drilling strength $S \equiv \Gamma(\gamma = 1)$, that assumes the physical meaning of power dissipated per unit fragmented volume.

Heterogeneous structures are characterized by volume fractions, properties of the different phases, type of microstructure and load acting on their boundaries. For the derivation of their behaviour, a sequential (in series) or a simultaneous (in parallel) arrangement of microstructural components at the interface between the body inducing the fragmentation and the base materials are assumed. These are represented by the cases shown in Figures 1, 2.

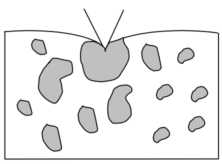

Figure 1 Two-phase heterogeneous material loaded with a punch smaller than the characteristic aggregate size.

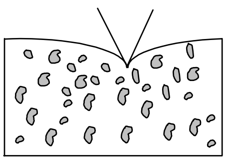

Figure 2 Two-phase heterogeneous material loaded with a punch larger than the characteristic aggregate size.

In the case of Figure 1, fragmentation occurs simply by the sequential removal of the individual components of volumetric fraction v_i and partial fragmentation strength S_i. The inverse of the macroscopic fragmentation strength *S,* should satisfy the following relation [43]:

$$S^{-1} = \sum_{i=1}^{N} S_i^{-1} v_i \, . \tag{4}$$

Eq. (4) represents the *inverse rule of mixture*.
On the other hand, assuming that the fragmentation strength may be determined by the *direct rule of mixture*, the following relation may be written [43]:

$$S = \sum_{i=1}^{N} S_i \, v_i \, . \tag{5}$$

This relation has been found for several heterogeneous materials, e.g., abrasion of fine dispersion of hard phase in soft matrix. Prerequisites are a width of the abrasive groove much larger than the particle size and spacing and a perfect bonding between the phases (Figure 2).
A third classical rule of mixture, intermediate between eqs. (4) and (5), was introduced to obtain, in some cases, a better description of the experimental data [44]:

$$S = \sum_{i=1}^{N} S_i \, v_i^2 \, . \tag{6}$$

The three rules of mixture of eqs. (4), (5) and (6) are shown in the diagram of Figure 3.

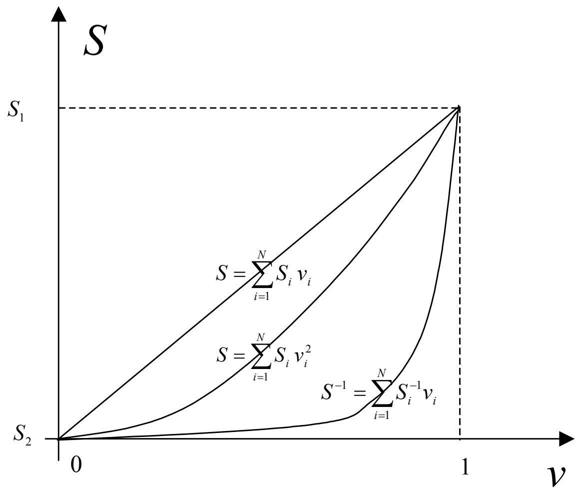

Figure 3 Rules of mixture for a two-phase material. Fragmentation strength *S* vs. volumetric fraction $v = v_1 = 1 - v_2$.

4 FRACTAL RULES OF MIXTURE

To determine the fractal rules of mixture for multi-scale fragmentation of heterogeneous materials, we should assume that all the phases are simultaneously fragmented. The power balance permits to obtain the power dissipation

$\dot{W}$ as the sum of the powers dissipated to crush each of the N phases:

$$\dot{W} = \sum_{i=1}^{N} \dot{W}_i = \sum_{i=1}^{N} \Gamma_i \dot{V}_i^{\gamma} . \tag{7}$$

The homogenisation of the mixture can be obtained as:

$$\dot{W} = \sum_{i=1}^{N} \Gamma_i \dot{V}_i^{\gamma} = \Gamma_{eq} \dot{V}^{\gamma} , \tag{8}$$

where Γ_{eq} is the equivalent fractal fragmentation strength:

$$\Gamma_{eq} = \sum_{i=1}^{N} \Gamma_i v_i^{\gamma} , \tag{9}$$

and the volume fractions $v_i = \frac{V_i}{V}$ satisfy the normalization rule:

$$\sum_{i=1}^{N} v_i = 1 . \tag{10}$$

Eq. (9) represents the fractal rule of mixture and, with eq. (8), describes the volume removed per unit time, $\dot{V}$, during the fragmentation of an heterogeneous material, as a function of the power $\dot{W}$ dissipated in the process:

$$\dot{V} = \left(\frac{\dot{W}}{\Gamma_{eq}} \right)^{\frac{1}{\gamma}} . \tag{11}$$

For the fragmentation of two- $(1/2 \le \gamma \le 1)$ or one-dimensional $(0 \le \gamma \le 1)$ heterogeneous bodies, eq. (1) becomes respectively [1]:

$$\dot{W} = \Gamma_{eq} \dot{\Omega}^{\gamma} , \tag{12}$$

$$\dot{W} = \Gamma_{eq} \dot{L}^{\gamma} , \tag{13}$$

where $\dot{\Omega}$ and $\dot{L}$ are respectively the area or length removed per unit time. The fractal rule of mixture (9) is still valid if v_i is considered respectively the area $v_i = \frac{\Omega_i}{\Omega}$ or the length $v_i = \frac{L_i}{L}$ fraction.

Note that due to the non-linearity of eq. (9), the case of an homogeneous material is recovered only for the limit case of $\gamma = 1$.

5 DRILLING COMMINUTION

We focus our attention on drilling comminution [2]. In this case, the homogenisation of the mixture is depending on the process (power consumption $\dot{W}$ or drilling velocity $\dot{\delta}$ controlled) and on the distribution of the aggregates (vertical or horizontal layers). Obviously, the first distribution in Figure 4, is the more realistic, since all the phases are distributed in vertical layers (parallel) and are simultaneously fragmented. The power consumption or drilling velocity controls coincide in this steady state process and we obtain exactly the rule of mixture of eq. (9).

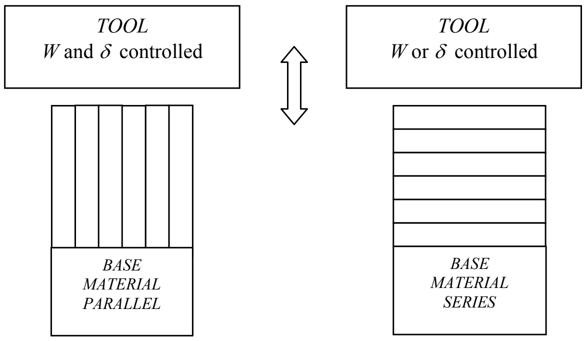

Figure 4 In parallel and in series drilling fragmentation.

On the other hand, if we assume a phase distribution in horizontal layers (in series arrangement) and a drilling velocity control ($\dot{\delta} = const$), we have:

$$\dot{W}_i = \Gamma_i \left(A\dot{\delta} \right)^{\gamma} , \tag{14}$$

A being the cross-section area of the hole and, via the energy balance:

$$W = \sum_{i=1}^{N} W_i = \sum_{i=1}^{N} \Gamma_i \left(A\dot{\delta} \right)^{\gamma} t_i , \tag{15}$$

where $t_i = \frac{h_i}{\dot{\delta}}$ is the time spent to drill the layer i of thickness h_i. The rule of mixture can be obtained comparing eq. (15) with the homogenised one:

$$W = \Gamma_{eq} \left(A\dot{\delta} \right)^{\gamma} t , \tag{16}$$

where $t = \sum_{i=1}^{N} t_i$ and being $\frac{t_i}{t} = \frac{h_i}{\sum_{i=1}^{N} h_i} = \frac{h_i}{h} = \frac{V_i}{V} = v_i$:

$$\Gamma_{eq} = \sum_{i=1}^{N} \Gamma_i v_i . \tag{17}$$

If we assume a power control ($\dot{W} = const$) and a phase distribution in horizontal layers, we have:

$$\dot{W} = \Gamma_i \left(A\dot{\delta}_i\right)^{\gamma} = \Gamma_{eq}\left(A\dot{\delta}\right)^{\gamma}, \tag{18}$$

where $\dot{\delta}$ is the mean value of the drilling velocities.
In addition, we have:

$$h = \sum_{i=1}^{N} h_i = \sum_{i=1}^{N} \dot{\delta}_i t_i \ . \tag{19}$$

Noting that:

$$h = \dot{\delta}\, t, \tag{20}$$

and being

$$t_i = \frac{h_i}{\dot{\delta}_i} = h_i \Gamma_i^{1/\gamma} \frac{A}{\dot{W}^{1/\gamma}}, \tag{21a}$$

$$t = \frac{h}{\dot{\delta}} = h\Gamma_{eq}^{1/\gamma} \frac{A}{\dot{W}^{1/\gamma}}, \tag{21b}$$

the rule of mixture can be obtained as:

$$\Gamma_{eq}^{1/\gamma} = \sum_{i=1}^{N} \Gamma_i^{1/\gamma} v_i \ . \tag{22}$$

To verify the obtained fractal rules of mixture, we can consider the classical (nonfractal) approach as their limit case. In this hypothesis, we have $\gamma = 1$ and $\Gamma \equiv S$, so that eq. (11) and the rules of mixture of eqs. (9), (17) and (22) become:

$$V = \frac{W}{S_{eq}}, \tag{23}$$

$$S_{eq} = \sum_{i=1}^{N} S_i v_i \ . \tag{24}$$

It is worth noting that eq. (23) represents the basic assumption to study the drilling process [45], and eq. (24) represents a direct rule of mixture [43].
Recently, Carpinteri and Pugno [2] have shown that a fractal approach for drilling comminution is more predictive than the traditional one. A multifractal extension has been also proposed by the same authors [46]. The developed fractal rules of mixture can be applied to fragmentation and comminution of heterogeneous materials. A practical application will be given in section 7.

6 GRINDABILITY

The grindability index [47] is defined as the ratio between the energy consumption in a material chosen as reference standard and the energy consumption in the tested material, when grinding the same volume to the same degree of fineness:

$$g = \frac{\dot{W}_{ref}}{\dot{W}} = \frac{\Gamma_{ref}\dot{V}^{\gamma}}{\Gamma_{eq}\dot{V}^{\gamma}} = \frac{\Gamma_{ref}}{\Gamma_{eq}} \ . \tag{25}$$

Since the grindability index g is inversely proportional to the (fractal) drilling strength, the inverse of the last one can be defined as the *grindability* of the mixture:

$$G_{eq} = \Gamma_{eq}^{-1}, \tag{26}$$

and depends on the rules of mixture of eqs. (9), (17) and (22).
Supposing $N = 2$ (binary mixtures) with $v_2 = v$ ($v_1 = 1 - v$) the rules of mixtures of eqs. (9), (17) and (22) can be plotted as reported in Figures 5. Eqs. (17) and (22) are substantially coincident and, by varying γ, always predict a worse grindability of the mixture than that of its separate phases. On the other hand, varying γ (around the unity), the more realistic rule of mixture of eq. (9) can be successfully used to model the grindability of a mixture grounds *better* ($\gamma > 1$) or *worse* ($\gamma < 1$) than that of its separate phases (Figures 5).

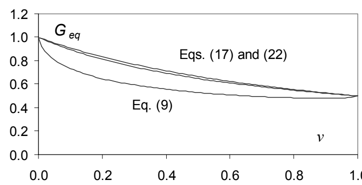

Figure 5a Grindability from the rules of mixture of eqs. (9), (17) and (22). Eqs. (17) and (22) are substantially coincident ($\Gamma_1 = 1, \Gamma_2 = 2, \gamma = 2/3$).

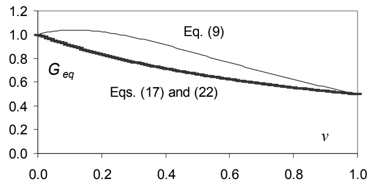

Figure 5b Grindability from the rules of mixture of eqs. (9), (17) and (22). Eqs. (17) and (22) are substantially coincident ($\Gamma_1 = 1, \Gamma_2 = 2, \gamma = 4/3$ (virtual)).

ISSN 1590-8844
International Journal of Mechanics and Control, Vol. 06, No. 02, 2005

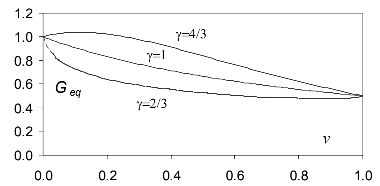

Figure 5c Grindability from the rule of mixture of eq. (9) ($\Gamma_1 = 1, \Gamma_2 = 2, \gamma = 2/3, 1, 4/3$ (virtual)).

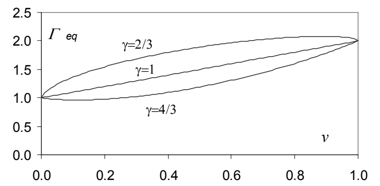

Figure 5d Fractal drilling strength (inverse of grindability) from the rule of mixture of eq. (9) ($\Gamma_1 = 1, \Gamma_2 = 2, \gamma = 2/3, 1, 4/3$ (virtual)).

Experiments show $\gamma < 1$, so that the values of $\gamma > 1$ can be considered only as virtual cases.

7 PRACTICAL EXAMPLE: DRILLING OF REINFORCED CONCRETE

We can focus our attention on the proposed fractal rule of mixture of eq. (9). For a two-phase material, it becomes:

$$\Gamma_{eq} = \Gamma_1 \nu_1^{2/3} + \Gamma_2 \nu_2^{2/3} . \tag{27}$$

$2/3$ being the fractal exponent for drilling comminution [2].

Some experiments are presented to validate the theoretical fractal rule of mixture of eq. (27). We have considered a special two-phase concrete, i.e., a mixture of mortar and limestone. Surprisingly, the fractal drilling strength of the two phases, mortar and limestone, is approximately the same and, therefore, of the same order of magnitude as that of the corresponding two-phase composite ($\Gamma_1 \cong \Gamma_2 \cong 15 \mathrm{MNm^{-1}s^{-1/3}}$). Eq. (27) results trivially verified.

On the other hand, the fractal drilling strength of steel is about two orders of magnitude larger than that of concrete and can be easily measured ($\Gamma_s \cong 105 \mathrm{MNm^{-1}s^{-1/3}}$). We can verify eq. (27) for reinforced concrete in different configurations, like the so-called *central cut* and *banana cut*, as represented in Figure 6. The aim of this section is to predict, via the proposed rule of mixture (9), the fractal drilling strength of the corresponding mixture (reinforced concrete = concrete + re-bar).

If we consider a reinforced concrete with fractal drilling strength Γ_{rc} ($\Gamma \cong 14 \mathrm{MNm^{-1}s^{-1/3}}$ is the fractal drilling strength for plain concrete), the power being experimentally constant before, during and after cutting the re-bar (power controlled tests), we have:

$$\begin{aligned} &\dot{W} \approx \Gamma\left(A\dot{\delta}\right)^{2/3} \approx \Gamma_{rc}\left(A\dot{\delta}_{rc}\right)^{2/3} \quad \Rightarrow \\ &\frac{\Gamma_{rc}}{\Gamma} \approx \left(\frac{\dot{\delta}}{\dot{\delta}_{rc}}\right)_{\exp}^{2/3} \approx 5^{2/3} \approx 3 \quad \Rightarrow \quad , \\ &\Gamma_{rc} \approx 3\Gamma \approx 45 \mathrm{MNm^{-1}s^{-1/3}} \end{aligned} \tag{28}$$

the ratio of the drilling velocity in concrete (before and after cutting the re-bar) to that in reinforced concrete (during cutting the re-bar), $\dot{\delta}/\dot{\delta}_{rc}$, an experimentally measured quantity.

The experimental value of Γ_{rc} appears in agreement with the prediction of the rule of mixture (27). In fact, if v represents the volumetric fraction of steel in concrete (see Figure 6), the fractal drilling strength of the mixture can be evaluated as:

$$\Gamma_{rc} = \Gamma(1-\nu)^{2/3} + \Gamma_s \nu^{2/3} . \tag{29}$$

For the *central cut*, the volumetric fraction of steel can be estimated as (Figure 6):

$$v \approx \frac{2d}{\pi D} = 0.17 , \tag{30}$$

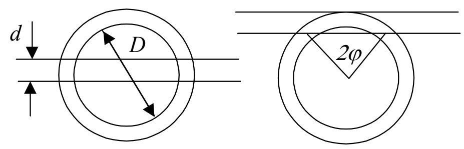

Figure 6 Central cut and banana cut configurations for reinforced concrete drilling.

where d is the diameter of the re-bar and D is the diameter of the tool.

Being $\Gamma_s \cong 105 \mathrm{MNm^{-1}s^{-1/3}}$, from the rule of mixture (29), we obtain:

$$\Gamma_{rc} = \Gamma(1-\nu)^{2/3} + \Gamma_s \nu^{2/3} \approx 44 \mathrm{MNm^{-1}s^{-1/3}} , \tag{31}$$

in agreement with the experimental result of eq. (28).

The same agreement can be found for the more critical *banana cut* configuration. In this case, the ratio between the drilling velocities, out of and in the re-bar zone, experimentally results to be twice than in the case of *central cut*:

$$\dot{W} \approx \Gamma\left(A\dot{\delta}\right)^{2/3} \approx \Gamma_{rc}\left(A\dot{\delta}_{rc}\right)^{2/3} \quad \Rightarrow$$
$$\frac{\Gamma_{rc}}{\Gamma} \approx \left(\frac{\dot{\delta}}{\dot{\delta}_{rc}}\right)_{\exp}^{2/3} \approx 10^{2/3} \approx 4.5 \quad \Rightarrow \tag{32}$$
$$\Gamma_{rc} \approx 4.5\Gamma \approx 63\mathrm{MNm^{-1}s^{-1/3}}$$

It means that the fractal drilling strength for the banana cut configuration experimentally results to be around 1.5 times larger than the fractal drilling strength for the *central cut* configuration.
For the banana cut configuration, if ϕ is the angular overlapping between re-bar and tool (Figure 6), we have:

$$\cos\phi \approx 1-\frac{2d}{D}, \tag{33}$$

so that:

$$\nu \approx \frac{\phi}{\pi} = 0.35\,. \tag{34}$$

From the rule of mixture of eq. (29), we have:

$$\Gamma_{rc} = \Gamma(1-\nu)^{2/3} + \Gamma_s \nu^{2/3} \approx 62\mathrm{MNm^{-1}s^{-1/3}}, \tag{35}$$

in good agreement with the experimental result of eq. (32). The experimental and theoretical results presented in this section are summarized in Table I.

Table I - Experimental and theoretical values of fractal drilling strength [$\mathrm{MNm^{-1}s^{-1/3}}$].

Concrete (Exp.)	Steel (Exp.)	RC (Exp.) Central-cut	RC (Exp.) Banana-cut	RC (Theor.) Central-cut	RC (Theor.) Banana-cut
14	105	45	44	63	62

8 CONCLUSIONS

In this paper we have proposed a new approach to study the fragmentation of mixtures. It extends the fragmentation universal laws [1] for energy dissipation in homogeneous materials to heterogeneous ones. As a practical application, we have focused our attention on artificial fragmentation by drilling of reinforced concrete (mixture of concrete and re-bar) in different configurations, like the so called *central* and *banana cut*. Theory and experiments agree satisfactorily.

REFERENCES

[1] Carpinteri A. and Pugno N., One-, two- and three-dimensional universal laws for fragmentation due to impact and explosion. *Journal of Applied Mechanics*, Vol. 69, pp. 854-856, 2002.

[2] Carpinteri A. and Pugno N., A fractal comminution approach to evaluate the drilling energy dissipation. *Int. J. of Numerical and Analytical Methods in Geomechanics*, Vol. 26, pp. 499-513, 2002.

[3] Carpinteri A. and Pugno N., Friction and specimen slenderness influences on dissipated energy density of quasi-brittle materials in compression: an explanation based on fractal fragmentation theory. *Int. Conf. on Fracture Mechanics of Concrete Structures-4*, May 28 – June 2, Cachan, France, pp. 665-668, 2001.

[4] Carpinteri A. and Pugno N., Multi-scale energy dissipation during impact and explosion fragmentation of quasi-brittle materials. *Int. Conf. on New Challenges in Mesomechanics*, August 26-30, Aalborg Univeristy, Denmark, pp. 97-103, 2002.

[5] Béla Beke D., *Principles of Comminution*. Publishing House of the Hungarian Academic of Sciences, 90-92, 1964.

[6] Turcotte D.L., *Fractals and Chaos in Geology and Geophysics*. Cambridge University Press, 20-32, 1992.

[7] Mandelbrot B.B., *The Fractal Geometry of Nature*. Freeman, New York, 1982.

[8] Feder J., *Fractals*. Plenum Publishing Corporation, New York, 1988.

[9] Grady D. E. and Kipp M. E., Geometric statistics and dynamic fragmentation. *J. Appl. Phys.*, Vol. 58, pp. 569-583, 1985.

[10] Redner S. Fragmentation. In Hermann H.J., Roux S. (Eds.), *Statistical Models for the Fracture of Disordered Media*. Elsevier, Amsterdam, 21-348, 1990a.

[11] Redner S., Statistical theory of fragmentation. In Hermann H. J., Roux S., Guyon F. (Eds.), *Disorder and Fracture*. Plenum Press, NY, 31-48, 1990b.

[12] Perfect E., Fractal models for the fragmentation of rocks and soils: a review. *Engineering Geology*, Vol. 48, pp. 85-198, 1997.

[13] Carpinteri A., Scaling laws and renormalization groups for strength and toughness of disordered materials. *Int. J. Solids and Structures*, Vol. 31, pp. 291-302, 1994.

[14] Carpinteri A. and Chiaia B., Multifractal scaling laws in the breaking behaviour of disordered materials. *Chaos, Solitons and Fractals,* Vol. 8, pp. 135-150, 1997.

[15] Carpinteri A., Ferro G. and Monetto I. Scale effects in uniaxially compressed concrete specimens. *Magazine of concrete research*, Vol. 51, pp. 217-225, 1999.

[16] Engleman R., Rivier N. and Jaeger Z. Size distribution in sudden breakage by the use of entropy maximization. *J. Appl. Phys.*, Vol. 63, pp. 4766-4768, 1988.

[17] Nagahama H., Fractal fragment size distribution for brittle rocks. *Int. J. Rock Miner Sci. Geomech. Abstr.*; Vol. 30, pp. 469-471, 1993.

[18] Yong Z. and Hanson M.T., A rotational source of plane fractals and its application to fragmentation analysis of thin plates. *Chaos, Solitons and Fractals*, Vol. 7, pp. 31-40, 1996.

[19] Aharony A., Levi A., Englman R., and Jaeger Z., Percolation model calculations of fragment properties. *Ann. Israel Phys. Soc.* Vol. 8, pp. 112-119, 1986.

[20] Matsushita M., Fractal viewpoint of fracture and accretion. *J. Phys. Soc. Jap.*, Vol. 54, pp. 857-860, 1985.

[21] Turcotte D.L., Fractal and fragmentation. *J. Geophys. Res.*, Vol. 91, pp. 1921-1926, 1986.

[22] Turcotte D.L., Fractals in geology and geophysics. *Pure Appl. Geoph.*, Vol. 131, pp. 171-196, 1989.

[23] Rieu M. and Sposito G., Fractal fragmentation, soil porosity and soil water properties: I. Theory. *Soil Sci. Soc. Am. J.*, Vol. 55, pp. 1231-1238, 1991.

[24] Crawford J.W., Sleeman B.D. and Young J.M., On the relation between number size distributions and the fractal dimension of aggregates. *J. Soil Sci.*, Vol. 44, pp. 555-565, 1993.

[25] Ching E.S.C., Multifractality of mass distribution in fragmentation. *Physica A.* Vol. 288, pp. 402-408, 2000.

[26] Sotolongo-Costa O., Rodriguez A.H. and Rodgers G.J., Dimensional crossover in fragmentation. *Physica A,* Vol. 286, pp. 638-642, 2000.

[27] Ben-Naim E. and Krapivsky P.L., Fragmentation with a steady source. *Physics Letters A.,* Vol. 275, pp. 48-53, 2000.

[28] Sammis C.G., Fractal fragmentation and frictional stability in granular materials. *IUTAM Symposium on Mechanics of Granular and Porous Materials*. Kluwer Academic Publisher, the Netherlands, pp. 23-34, 1997.

[29] Hyslip P. and Vallejo L.E., Fractal analysis of the roughness and size distribution of granular materials. *Enginnering Geology,* Vol. 48, pp. 231-244, 1997.

[30] Hecht C.A., Appolonian Packing and fractal shape of grains improving geomechanical properties in engineering geology. *Pure Appl. Geophys.*, Vol. 157, pp. 487-504, 2000.

[31] Momber A.W., The fragmentation of standard concrete cylinders under compression: the role of the secondary fracture debris. *Engineering Fracture Mechanics,* Vol. 67, pp. 445-459, 2000.

[32] McDowell G. R., Bolton M. D. and Robertson D., The fractal crushing of granular materials. *J. Mech. Phys. Solids,*; Vol. 44, pp. 2079-2102, 1996.

[33] Schocke D., Arastoopour H. and Bernstein B., Pulverization of rubber under high compression and shear. *Powder Technology,* Vol. 102, pp. 207-214, 1999.

[34] Salman A.D. and Gorham D.A., The fracture of glass spheres. *Powder Technology*, Vol. 107, pp. 179-185, 2000.

[35] Belingardi G., Gugliotta A., and Vadori A., Numerical simulation of fragmentation of composite material plates due to impact. *Int. J. Impact Eng.*, Vol. 21, pp. 335-347, 1998.

[36] Ching E.S.C., Lui S.L., Ke-Qing Xia., Energy dependence of impact fragmentation of long glass rods. *Physica A*, Vol. 287, pp. 83-90, 2000.

[37] Tomas J., Schreier M., Gröger T. and Ehlers S., Impact crushing of concrete for liberation and recycling. *Powder Technology*, Vol. 105, pp. 39-51, 1999.

[38] Larsson I. and Kristensen H.G., Comminution of a brittle/ductile material in a Micros Ring Mill. *Powder Technology*, Vol. 107, pp. 175-178, 2000.

[39] Cleary P., Modelling comminution devices using DEM. *Int. J. for Numerical and Analytical Methods in Geomechanics*, Vol. 25, pp. 83-105, 2001.

[40] Rittinger P.R., *Lehrbuch der Aufbereitungskunde*. Berlin, 1867.

[41] Kick F., Das Gesetz der Proportionalen Widerstände. Leipzig, 1885.

[42] Bond F.C., The third theory of comminution. *Mining Engineering*, Vol. 193, pp. 484-494, 1952.

[43] Hornbogen E., *Friction and Wear of Polymer Composites*. Composite Materials Series, 1. Edited by Klaus Friedrich, Elsevier, pp. 61-88, 1986.

[44] Zum-Gahr K.H., *Microstructure and Wear of Materials*. Tribology Series, Elsevier. Vol. 10, 1987.

[45] Paone J. and Bruce W.E., *Drillability Studies – Diamond Drilling*. USBM-RI 6324, 1963.

[46] Carpinteri A., Pugno N., A multifractal comminution approach for drilling scaling laws. *Powder Technology*, Vol. 131, pp. 93-98, 2003.

[47] Remenyi K., *The Theory of Grindability and the Comminution of Binary Mixtures*. Akademiai Kiado, Budapest, 1974.

ISSN 1590-8844
International Journal of Mechanics and Control, Vol. 06, No. 02, 2005

REACHING LAW MODIFICATION OF TIME SUB-OPTIMAL VARIABLE STRUCTURE CONTROL

Jan Kardos

Faculty of Electrical Engineering and Information Technology
Slovak University of Technology, Bratislava, Slovak Republic

ABSTRACT

To eliminate chattering in time sub-optimal variable structure control, a reaching law approach is applied. The paper presents a chattering-free modification of the robust fixed target position control system with parametric disturbance comparable with a time-optimal control of deterministic SISO systems. The theoretical background of the control algorithm is provided with a system of theorems. Despite the parameter uncertainty, simulation results show both the fast and robust overshoot-free responses.

Keywords: time sub-optimal control, sliding mode control, reaching law, chattering-free

1 INTRODUCTION

Basically, there are known two groups of time sub-optimal or near time-optimal variable structure systems. In the first one, a modified time-optimal trajectory (dynamically reduced) in a role of switching function ensures the sliding mode existence [3], [14], [22]. In the second one, the plant is forced to trace a near time-optimal command in sliding mode using particularly a linear switching function [1], [8], [15], [21], [23]. In both groups, the robustness is achieved in sliding mode due to reserve in actuator output. Consequently, the dilemma is the original time-optimal performance reduction. Time sub-optimal control (TSC) presented in [10], [11] belongs to the class of fast non-linear robust control algorithms with driving level commutation. It has been derived using the geometrical approach in position control systems with parameter uncertainty as an application of variable structure systems theory to the deterministic time-optimal control (TOC) algorithm. TSC has the advantage of keeping (preserving) the time-optimality for the essential part of the control process. Both TOC and TSC have the property of fast dynamics but in presence of parametric disturbance, only the latter ensures the transient quality without an overshoot. Variable structure control uses the sliding mode to trace a switching function. In real motion control systems, due to parasitic nonlinearities and unmodelled dynamics influence the sliding mode vanishes and an undesirable chattering appears [7], [16]. To deal with the chattering phenomenon the boundary layer [9], the saturation nonlinearity [13], [19] or a continuous element of the control algorithm [7], [18] are often introduced. These may, however, result in steady state error and robustness decay. The dither injection, presented in [10], belongs to the special linearisation techniques and gives good results in particular control schemes of discrete nature. The application of higher order sliding modes - the modern way of the chattering elimination - to position control systems may deal with the problem of the plant's state vector acquisition, particularly of the higher order elements [2], [4], [6], [12]. The sophisticated techniques with a state observer or with an integral sliding mode application [17], [18], [20] give very good results in chattering reduction (quenching the sliding mode in an auxiliary bypass loop) at the expense of the control structure simplicity. A handy way of chattering elimination seems to be the reaching law utilisation [5]. Thus, the control in the close vicinity of the switching manifold is similar to the continuous equivalent control, i.e. the mean value of the original VSC, without any high-frequency oscillations.

In this paper a reaching law application to the time sub-optimal control algorithm is presented. The main contributions of this work are the development and the design of a chattering-free time sub-optimal controller and the establishment of condition under which the best transient can be reached such that the robustness in the presence of parameter uncertainty is achieved.

Contact author: Jan Kardos

Slovak University of Technology,

Faculty of El. Engineering and Information Technology,

Ilkovicova 3,

812 19 Bratislava, Slovak Republic

2 TIME SUB-OPTIMAL CONTROL

In this chapter we provide a brief summary of the original *time sub-optimal control* [10] without the chattering elimination. It has been derived for a single link of a rigid manipulator considering one dominant variable time constant as an influence of moment of inertia variation.
Let the position control system's plant be described in the error vector space by the phase canonical form

$$\frac{d\mathbf{e}}{dt} = \left[\dot{e}, -\frac{1}{T}\left(Ku + \dot{e}\right)\right]^T \tag{1}$$

where $\mathbf{e} \in R^2$ is the error vector $\left[e, \dot{e}\right]^T$, K is for gain, u is the scalar control action input and T is for time constant affected by disturbances. Let the variable parameter T obey

$$T \in \left\langle T_{\min}, T_{\max} \right\rangle \tag{2}$$

The goals of the time sub-optimal control have been formulated similarly to those in the time-optimal control framework [11] and are as follows

i) the response should be free of overshoot despite the uncertainty (2),
ii) the dynamics of the closed loop system should be time-optimal for at least one value of T from (2) and
iii) the switching function should be linear.

This control strategy can be viewed as a robustification of the time-optimal control. The structure of a time sub-optimal position control system is in Figure 1 and as can be seen it is very simple and identical to the time-optimal one. In this figure, $\mathbf{w} = [w, 0]^T$ $\left(w = \text{cons.}\right)$ represents the closed loop system's reference vector, M is for driving level of the relay element and $\mathbf{x}$ is the plant's phase vector. $F\left(\mathbf{e}\right) \in R$ defines the switching surface and is to be designed.

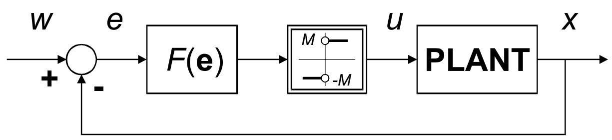

Figure 1 Principal structure of time sub-optimal position control system.

In accordance with the theory of VSC with driving level commutation, the control law formula

$$u = M\,\mathrm{sgn}(F) \tag{3}$$

is discontinuous and therefore the system's behaviour has an oscillating character. If in the close neighbourhood of the switching manifold the following condition is satisfied

$$F\left(\mathbf{e}\right)\frac{dF\left(\mathbf{e}\right)}{dt} < 0 \tag{4}$$

the system is in a *sliding mode* [16] and is insensitive to parameter variations. The condition (4) is known as the sliding mode existence condition or the *reaching condition* for the whole state space [7].
To fulfil the time sub-optimal control goals the geometric approach has been applied. The switching function is expressed as a linear combination of the error vector elements

$$F\left(\mathbf{e}\right) = \dot{e} + \alpha e = 0 \tag{5}$$

where α is a positive constant and it is the slope of the switching line (5) in $\left(e, \dot{e}\right)$ plane. Parameter α is chosen so that for any T from (2) the system's state doesn't encroach on the region limited by the $\dot{e}$-axis and the worst system's time-optimal rundown (deceleration) trajectory, i.e. the trajectory for $T_{\max}$. To meet this requirement, the switching line should cross the intersection point of the phase portrait asymptote $\dot{e} = \pm KM$ and the above-mentioned trajectory (cf. Figure 3). Thus, the end result of the time sub-optimal control synthesis corresponds to the following α value

$$\alpha = \frac{1}{T_{\max}\left(1 - \ln 2\right)} \tag{6}$$

In time sub-optimal control, the major part of the system's trajectory (the whole trajectory for both $T = T_{\max}$ and the limit case of $\dot{e} = \pm KM$) is identical to the time-optimal one, the robustness of sliding mode is exploited only in the final part of a rundown phase.
In conclusion we can say, that for the linear switching function (5) gives the solution (6) the best possible system's dynamics for any arbitrary frequency spectra of the parametric disturbance (2) and for arbitrary command w. Moreover, no form of on-line parameter identification should be considered.

3 EQUIVALENT CONTROL

The plant's behaviour in the time domain is described by the set of differential equations (1). To cope with the description of the system's behaviour in sliding mode where the right-hand side of the system's differential equation is discontinuous (non-analytic), it is inevitable to get the unique solution of the system's trajectory tangential velocity vector, i.e. to perform the so called regularisation. There were introduced many methods of regularisation but the solutions for a common non-linear system differ, thus the description is not accurate in general [16]. In this chapter we shall prove the uniqueness of the sliding mode description of the controllable canonical form via any

regularisation method and give the brief description of the equivalent control approach.
Let the plant be described by the controllable canonical form in the error space

$$\frac{d\mathbf{e}}{dt} = \left[\dot{e}, \cdots, e^{(n-1)}, f(\mathbf{e}, u)\right]^T \tag{7}$$

where $\mathbf{e} \in R^n$ stands for the control error vector and f denotes the scalar function (linear or non-linear). Note that the position control system's plant (1) belongs to this category and (7) represents the system's trajectory tangential velocity vector **t** in the error space.
The sliding mode existence necessary and sufficient condition (4) at the point $A \in R^n$ on the switching surface

$$F(\mathbf{e}) = 0 \tag{8}$$

with the control (3) of the plant (7) can be rewritten in the form of the following theorem [10]. Denote $\mathbf{n}_A$ the normal vector to the switching surface (8) at A.

Theorem 1: Let for the negative value of control input u be φ_{1A} the convex angle between the normal vector $\mathbf{n}_A$ and the tangential velocity vector $\mathbf{t}_A$ and similarly be the angle φ_{2A} for the opposite value of u. The system (7) will be in sliding mode at a point A on the switching surface (8) if and only if

$$\mathrm{sgn}(\cos(\varphi_{1A})) = -\mathrm{sgn}(\cos(\varphi_{2A})) > 0 \tag{9}$$

Proof: See reference [10].

Directly from Theorem 1 follows the next lemma.

Lemma 1: The controlled plant (7) doesn't fulfil the condition (9) of the Theorem 1 on any part of the switching surface (8) that is parallel to the $e^{(n-1)}$ axis of the error space.

Proof: We can get any of values of $\cos(\varphi_A)$ as the normalised inner product of the normal vector $\mathbf{n}_A$ and tangential velocity vector $\mathbf{t}_A$. These vectors are defined as follows

$$\mathbf{n}_A = \left(\frac{\partial F(\mathbf{e})}{\partial \mathbf{e}}\right)_A \tag{10}$$

and

$$\mathbf{t}_A = \left(\frac{d\mathbf{e}}{dt}\right)_{A,u} \tag{11}$$

For both opposite values of u, from (7), it is obvious that the only possibility to change the sign of the $\cos(\varphi_A)$ has the nth element of the $\mathbf{t}_A$ vector. For the nth element of the normal vector $\mathbf{n}_A$ on the switching surface's part parallel to the $e^{(n-1)}$ axis holds

$$\left(\frac{\partial F(\mathbf{e})}{\partial e^{(n-1)}}\right)_A = 0 \tag{12}$$

Therefore the $\cos(\varphi_A)$ can't change the sign and this completes the proof.

Now we are ready to prove the uniqueness of the plant's (7) sliding mode description.

Theorem 2: Any of the regularisation methods of the controllable canonical form (7) gives the unique description of the plant's sliding mode behaviour.

Proof: Let $T_A(\mathbf{e}) = 0$ denote the tangential hyperplane to the switching surface (8) at a point A. Let the system (7) be in sliding mode at a point A, i.e. the system's trajectory traces the switching surface (8) and the plant's velocity vector lies in the tangential hyperplane. The first (n-1) coordinates of the tangential velocity vector are uniquely described by the first (n-1) elements of the system (7), regardless of the regularisation method. According to Lemma 1, for these (n-1) coordinates there exists only one nth coordinate of the plant's velocity vector in the sliding mode, uniquely associated with the hyperplane $T_A(\mathbf{e}) = 0$. Thus, there exists only one possible tangential velocity vector describing the system's sliding mode behaviour. This completes the proof.

The *equivalent control* represents the continuous equivalent of the discontinuous sliding mode control algorithm with the identical behaviour, i.e. the equivalent control forces the plant's trajectory to follow the switching surface. The aim is to find the control u_{equ} equivalent to the mean value of the high-frequency control action input u in sliding mode. To keep the system's trajectory on the switching surface (8), the following condition should be satisfied

$$\left.\frac{dF(\mathbf{e})}{dt}\right|_{u=u_{equ}} = 0 \tag{13}$$

for the initial condition

$$F(\mathbf{e}(0)) = 0 \tag{14}$$

Solving (13) for u, assuming (7), yields the equivalent control u_{equ}, provided that there exists the explicit solution u of

$$\frac{de^{(n-1)}}{dt} = f(\mathbf{e}, u) \tag{15}$$

According to (3), u_{equ} satisfies the conditions

$$\min(u) \le u_{equ} \le \max(u) \tag{16}$$

The analytical description of the sliding mode behaviour using the equivalent control approach is summarised in the next theorem.

Theorem 3: The sliding mode behaviour of the *n*th-order system (7) is described by the reduced differential equation (8) of order (*n*-1) of the switching manifold for the initial condition (14).

Proof: Applying (13) to (7) and (8) gives

$$\left.\frac{dF(\mathbf{e})}{dt}\right|_{u=u_{equ}} = \left(\frac{\partial F(\mathbf{e})}{\partial \mathbf{e}}\right)^T \left.\frac{d\mathbf{e}}{dt}\right|_{u=u_{equ}} =$$

$$= \frac{\partial F}{\partial e}\frac{de}{dt} + \cdots + \frac{\partial F}{\partial e^{(n-2)}}\frac{de^{(n-2)}}{dt} + \frac{\partial F}{\partial e^{(n-1)}} f\left(\mathbf{e}, u_{equ}\right) = 0 \tag{17}$$

Hence by Lemma 1, without necessity of solving the equation (17) with respect to u_{equ}, substituting (17) to (7), the differential equation of the sliding mode is found

$$\frac{de^{(n-1)}}{dt} = -\frac{1}{\dfrac{\partial F}{\partial e^{(n-1)}}}\left(\frac{\partial F}{\partial e}\frac{de}{dt} + \cdots + \frac{\partial F}{\partial e^{(n-2)}}\frac{de^{(n-2)}}{dt}\right) \tag{18}$$

Integrating the implicit form of equation (18) for the initial condition (14) yields

$$F(\mathbf{e}) = 0 \tag{19}$$

which is identical to the switching surface (8) and represents the differential equation of order (*n*-1) for the control error. This completes the proof.

Theorem 3 gives the solution of the robustness problem via sliding mode control – the system in sliding mode is described by the switching function differential equation and it is completely insensitive to plant's parametric and external disturbances.
Let us focus our attention on the sliding mode description of the time sub-optimal position control system. Applying (13) to (1) and (5) gives

$$u_{equ} = \frac{1}{K}(\alpha T - 1)\dot{e} \tag{20}$$

which corresponds to the D-regulator output. Control (20) keeps the system's trajectory on the switching surface (8) only if the initial condition

$$\dot{e}(0) = -\alpha e(0) \tag{21}$$

is fulfilled.
According to Theorem 3, the system's trajectory in sliding mode is described by the differential equation

$$\frac{de}{dt} + \alpha e = 0 \tag{22}$$

for the initial condition (21). The solution of (21) and (22) gives the exponential decay of the control error in the time domain

$$e(t) = e(0)\exp(-\alpha t) \tag{23}$$

In general, the steeper is the slope α of the switching line (5) the faster is the transient response in sliding mode.

4 EQUIVALENT TIME SUB-OPTIMAL CONTROL

The sliding mode control in real systems suffers from a significant drawback - the chattering. This stands for the high-frequency oscillation excited by the discontinuous control law (3) due to presence of parasitic dynamics and nonlinearities. In this chapter, we introduce a chattering-free continuous modification of the time sub-optimal control preserving its robustness and dynamism.
We formulate the requirements for the control law as follows:

i) the quality of the control should be comparable to the time sub-optimal one (cf. goals in Chapter 2),
ii) the control should be continuous and chattering-free.

The continuous equivalent control (20) keeps the system's trajectory on the switching surface (8), provided that the plant's parameters are constant and the error vector initial condition satisfies (14). In case of parametric uncertainty (2) and out of the switching manifold (8) the equivalent control algorithm fails. This is the consequence of the fact, that except for the switching surface (8) the equivalent control doesn't fulfil the condition (4).
Let us define the switching function $F(\mathbf{e})$ behaviour by the differential equation

$$\frac{dF(\mathbf{e})}{dt} = -kF(\mathbf{e}) \tag{24}$$

where k is a positive constant.
From (13) and (24), it can be seen that the control guaranteeing the fulfilment of (24) is on the switching surface, i.e. for $F(\mathbf{e}) = 0$, identical to the equivalent control. Moreover, according to (24), the condition (4) holds for the whole state space. This ensures that at any point of the state space the plant's trajectory tends towards the sliding manifold. In other words, the differential equation (24) represents the *sliding mode reaching condition* or so-called *reaching law* [7]. From (24), it is

evident that the switching function $F(\mathbf{e})$ exponentially decays in the time domain with the time constant $1/k$.
Similarly to time sub-optimal control, let the equivalent control u_{EQU} be the control of plant (1) and (2) satisfying (5), (6) and also the reaching condition (24). Substituting (1) and (5) into (24) yields

$$u_{EQU} = \frac{1}{K}\left[(\alpha T_u - 1)\dot{e} + kT_u(\dot{e} + \alpha e)\right] \tag{25}$$

where $T_u > 0$ denotes for the moment unknown time constant originating from the plant's parameter uncertainty (2). Note that on the switching surface (5), expression (25), except for T_u, equals to (20) as mentioned earlier. It can be seen from (25) that the continuous control u_{EQU} consists of two typical components – the proportional part with the gain

$$K_P = \frac{\alpha k T_u}{K} \tag{26}$$

and the derivative one with the corresponding gain

$$K_D = \frac{(\alpha + k)T_u - 1}{K} \tag{27}$$

Now, let us focus our attention on restrictions imposed on the equivalent control parameters T_u and k.

Theorem 4: For the equivalent control (25) of the system (1), (2), (5) and (6), the sufficient condition to ensure the non-oscillating character of the transient is

$$T_u \geq T_{\max} \tag{28}$$

Proof: Substituting (25) in (1) gives the second order differential equation of the system's closed-loop dynamics

$$\frac{d^2 e}{dt^2} + \frac{T_u}{T}(\alpha + k)\frac{de}{dt} + \frac{T_u}{T}\alpha k e = 0 \tag{29}$$

with damping ratio

$$b = \frac{1}{2}\frac{\alpha + k}{\alpha k}\sqrt{\frac{T_u}{T}\alpha k} \tag{30}$$

For non-oscillating behaviour of the control error e it is necessary to keep the damping ratio b greater or equal to unity, i.e. to fulfil the condition

$$\sqrt{\frac{T_u}{T}}(\alpha + k) \geq 2\sqrt{\alpha k} \tag{31}$$

Note that α and k are positive constants. It is trivial, after some algebra, to prove (31) for $T_u = T$. Evidently, (31) is also valid for all $T_u > T$. According to the above and to parameter uncertainty (2), the expression (28) represents the sufficient condition of the non-oscillating behaviour of the dynamics (29). This completes the proof.

In order to meet the requirements set on the desired control, it is necessary to reach the fast development of the switching function (5). This corresponds, according to (24), with the high value of the control parameter k and implies the possible control action constraint in a real system. In agreement with the original TSC, we should limit the value of the new control action to M as follows

$$u_{ETSC} = \begin{cases} u_{EQU} & \text{for } \operatorname{abs}(u_{EQU}) < M \\ M\operatorname{sgn}(u_{EQU}) & \text{for } \operatorname{abs}(u_{EQU}) \geq M \end{cases} \tag{32}$$

where u_{ETSC} stands for the proposed *equivalent time sub-optimal control*.
The block diagram of the equivalent time sub-optimal control system is presented in Figure 2. The difference between this control structure and the original TSC structure is minimal, as seen in Figures 1 and 2. In both structures, the linear part of control algorithm represents a PD-regulator. As for the non-linear part, a limiter in equivalent time sub-optimal control structure substitutes the relay element in TSC.

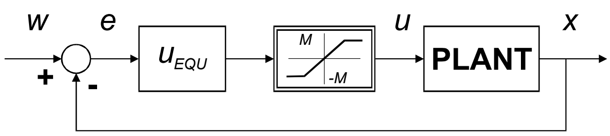

Figure 2 Equivalent time sub-optimal position control system.

The continuous control u_{ETSC} is within the region of the constraint M identical to the original time sub-optimal control. The linear control u_{EQU} is active only in a particular area of the $(e, \dot{e})$ plane in the vicinity of the switching manifold (5). Let us specify the boundaries of this control area. Comparing (25) with $\pm M$ yields

$$\begin{gathered} \frac{1}{\alpha k T_u}\left[-KM - ((\alpha + k)T_u - 1)\dot{e}\right] \leq e \\ e \leq \frac{1}{\alpha k T_u}\left[KM - ((\alpha + k)T_u - 1)\dot{e}\right] \end{gathered} \tag{33}$$

The following interpretation of the expression (33) is more illustrative. The linear phase u_{EQU} of the equivalent time sub-optimal control is concentrated in a zone of the width (in the direction of the e-coordinate)

$$\pm\frac{KM}{\alpha k T_u} \tag{34}$$

around the line of the zero control action

$$\dot{e} = -\frac{\alpha k T_u}{(\alpha + k)T_u - 1} e \tag{35}$$

The relevant parts of the system's phase portrait are given in Figure 3. In this figure, line (35) is labelled $u = 0$ and similarly are the boundaries $u = M$ and $u = -M$. $F(\mathbf{e}) = 0$ denotes the original time sub-optimal switching line (5). Trajectory marked T_{max} is one of the plant's time-optimal rundown trajectories.

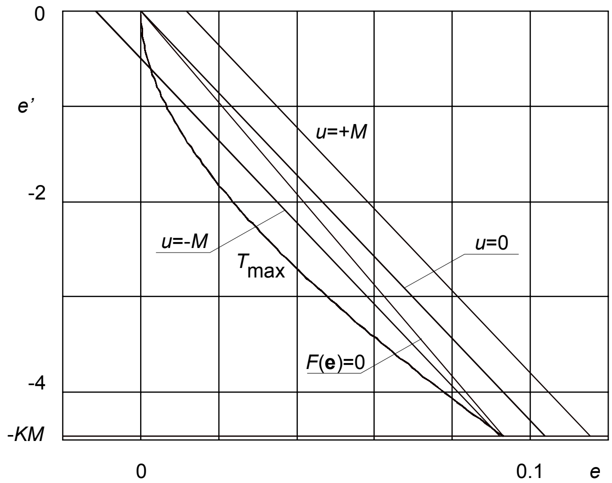

Figure 3 Phase portrait of the position control system.

Although the line (35) seems to play a role of a new switching line, it should be emphasised that the fulfilment of the reaching condition (24) with respect to the switching line (5) is ensured at any time instant of the transient within the linearity zone (34), (35). As can be seen from (34) and (35), to keep the line (35) close to the switching line (5), i.e. to reach the convergence of both the equivalent time sub-optimal control and the TSC dynamics, it is important to satisfy the condition

$$k >> 1 \tag{36}$$

which corresponds to the requirement of the fast switching function dynamics (24).
The condition (36) ensures both the width (34) of the linearity zone reduction and the coincidence of the slope of line (35) with the parameter α of the switching line (5), particularly if the condition

$$k >> \alpha \tag{37}$$

is fulfilled.
As can be seen from (32), the reaching condition (24) is not explicitly fulfilled out of the linearity zone (34) and (35). The system's trajectory can leave this zone, provided that the variable parameter T exceeds the critical value T_{crit} corresponding to the sliding mode decay. Despite this fact we can prove that the system's (1) trajectory returns to the switching manifold (5). Joining the expressions (1), (5) and (9) we obtain

$$T_{crit} = \frac{2}{\alpha} \tag{38}$$

For the control action $u = \pm M$, the switching function evolution contains a global extreme. Setting the first derivative of (5) equal to zero gives the $\dot{e}$ coordinate of this extreme

$$\dot{e} = \frac{Ku}{\alpha T - 1} \tag{39}$$

Substituting (39) to the second derivative of (5) yields

$$\frac{d^2 F}{dt^2} = -\frac{\alpha K u}{T} \tag{40}$$

According to (40), the switching function reaches for $u = -M$ its global minimum (or for $u = M$ the global maximum) and then returns to the zero value, i.e. the system's trajectory returns to the switching manifold.
Note that the condition (28) in Theorem 4 prevents any doubt about an overshoot of the plant's (1) response in the presented control. From the phase portrait in Figure 3, it can be seen that to solve the problem of the possible overshoot, the switching line (5) should be steeper than the line (35). Comparing (6) and (35) yields

$$T_u > (1 - \ln 2)T_{max} \tag{41}$$

Similarly, the intersection point of the phase portrait asymptote $\dot{e} = -KM$ with the switching line (5) should be closer to the $\dot{e}$-axis than the one with the line (35). Comparing the e-coordinates of these two points (cf. (5), (6) and (35)) yields

$$T_u > 2(1 - \ln 2)T_{max} \tag{42}$$

Theorem 4 meets both of the last conditions.
The properties of the equivalent time sub-optimal control can be summarised as follows. The control algorithm is described by expression (25) and (32) with the parameter values (6), (28), (36) and (37). We expect that despite the parameter uncertainty (2) the response will be both chattering and overshoot free with the dynamics close to the time-optimal one. Note that only the boundary values of the

disturbance (2), without the time behaviour of the variable parameter, are assumed to be known.

5 SIMULATION RESULTS

The proposed equivalent time sub-optimal control algorithm has been applied to a position control model (1) with parameters corresponding to a real electro-mechanical chain (PWM converter - DC motor - harmonic drive HD – incremental position/velocity sensor). The parametric disturbance represents the variation of the reduced moment of inertia at the motor shaft. The values of parameters have been as follows: the chain total gain $K = 0.0883$, the boundaries of parametric uncertainty (2) $T_{\min} = 0.018\,\mathrm{s}$ and $T_{\max} = 0.068\,\mathrm{s}$. The reference input $w = 0.2$ is equivalent to the HD's output shaft angle position 51°. To fulfil conditions (28), (36) and (37), the control parameters were chosen as follows

$$T_u = T_{\max}$$

and

$$k = 1000 \tag{43}$$

which represents the α to k ratio $1:20$.
To simulate the influence of parasitic dynamics presence, the ratio of its equivalent time constant T_P to plant's time constant $T_{\max}$ was chosen also $1:20$.

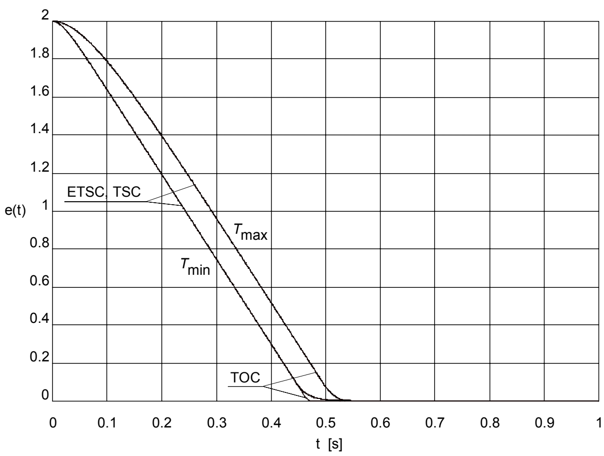

Figure 4 Control error evolution for $T_{\min}$ and $T_{\max}$ for three types of control algorithm.

Note that we should focus our attention on the rundown phase of the transient, because this is the only phase where the equivalent time sub-optimal control differs from TSC.

Moreover, the main part of the control process, particularly the start-up (acceleration) phase, is identical to that of the time-optimal one, as mentioned earlier. Only Figure 4 illustrates the whole transient in time domain. In this figure, three control algorithms for both boundary values $T_{\min}$ and $T_{\max}$ of the parametric uncertainty are compared: TOC is for time-optimal control, TSC for time sub-optimal control and ETSC for equivalent time sub-optimal one. The plots show the high quality of the ETSC process – no overshoot and fast dynamics close to TOC. It can be seen that at this resolution all three responses for $T_{\max}$ value coincide. For time constant $T_{\min}$ only TOC slightly differs. The short delay of TSC and ETSC is the price paid for the system robustness in sliding mode. This figure shows the fulfilment of both the time sub-optimal control goals (Chapter 2) and the requirement i) for the equivalent time sub-optimal control law (Chapter 4).
Following pictures show only the detailed plots within the time interval of the rundown phase.
The first group of figures (see Figures 5 – 7 in the left column on the next page) depicts the responses for $T = T_{\min}$ with the whole rundown phase in sliding mode (cf. sliding mode existence condition (4)). The control error plot in Figure 5 has an exponential character due to the linear switching function (5). As a result of the high value of parameter k, the linearity zone (34) is very narrow and the difference between ETSC and TSC is minimal.
The resulting plots of the control action chattering for TSC and the smooth evolution of u for ETSC are given in Figure 6 and 7 respectively. These figures clearly show the advantage of the chattering-free equivalent time sub-optimal algorithm (32) over the discontinuous TSC (3).
Similarly to the first group of figures, the second group (see Figures 8 – 10 in the right column) depicts the responses for the time constant $T = T_{\max}$. According to time sub-optimal control goals (Chapter 2), in this case is the system's trajectory for TSC identical to the time-optimal one and the sliding in rundown phase is not present. Figure 8 shows the control error plot of both the TSC and ETSC transients. Evidently, no response can be faster than that of TSC. The short delay of the ETSC control error occurs due to the linearity zone (34). Nevertheless, the dynamics of the equivalent time sub-optimal control is comparable to the time sub-optimal one.
Figures 9 and 10 show the control action behaviour for TSC and ETSC respectively. It can be seen that in the rundown period neither TSC nor ETSC suffers from a chattering. This appears only in the steady state of the time sub-optimal control (see Figure 9). There is again no doubt about the quality of the proposed equivalent time sub-optimal control (Figure 10). The control action plot proves the time-optimal behaviour of the ETSC transient, except for the narrow linearity zone (34).

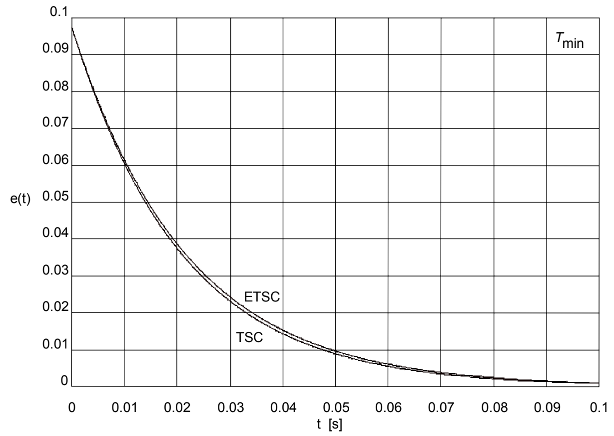

Figure 5 Rundown phase of control error for TSC and ETSC and for T_{min}.

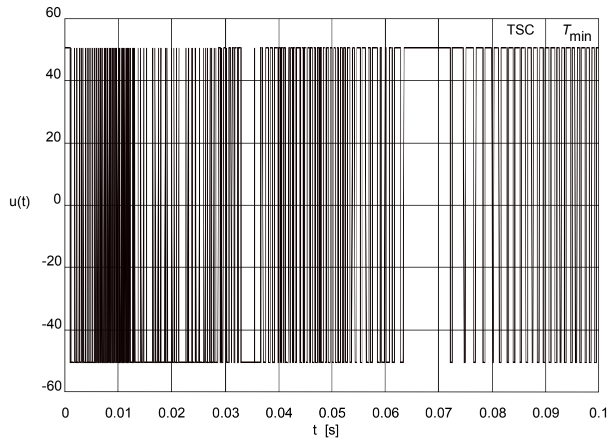

Figure 6 Control action chattering for TSC and T_{min}.

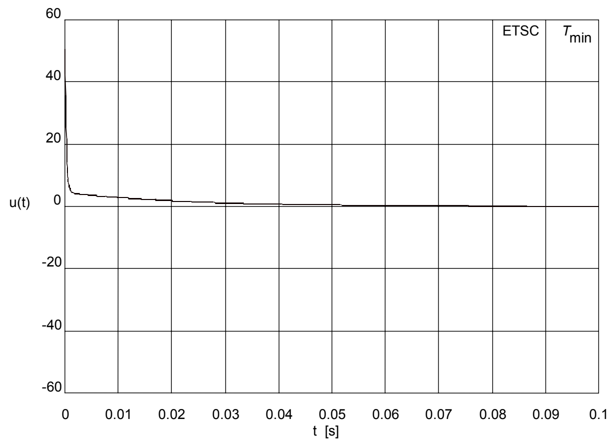

Figure 7 Control action plot for ETSC and T_{min}.

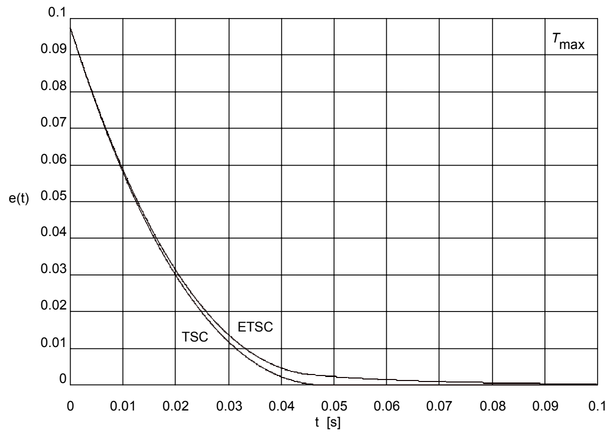

Figure 8 Rundown phase of control error for TSC and ETSC and for T_{max}.

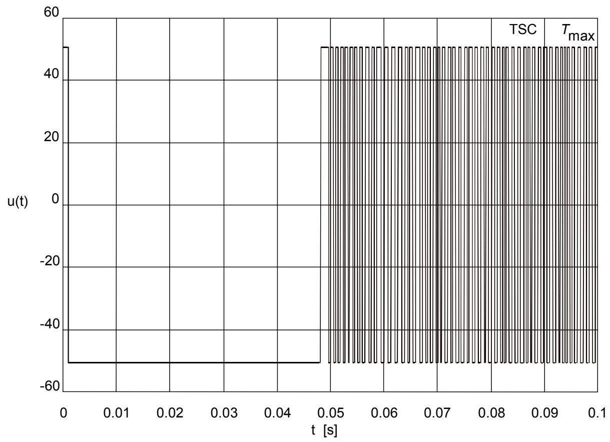

Figure 9 Control action chattering for TSC and T_{max}.

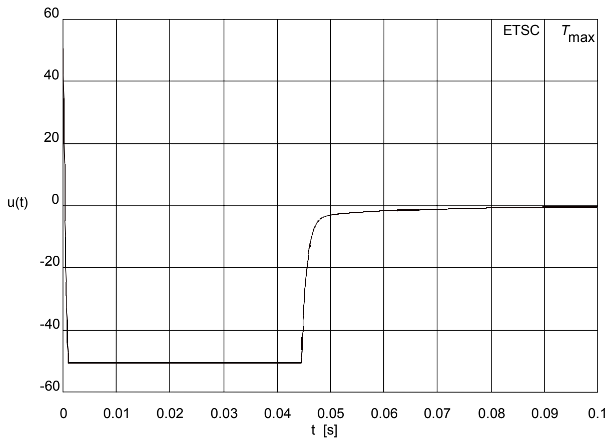

Figure 10 Control action plot for ETSC and T_{max}.

Note that according to (13) and (24), the u_{ETSC} plot may be viewed as a mean value of the u_{TSC} chattering. To prove this statement, the evolution of the switching function during the rundown period has been depicted (see Figure 11 for $T = T_{\min}$). Both the values of the switching function (5) for TSC and ETSC are close to zero. Thus, the u_{ETSC} plot represents the approximate solution of (24) on the switching surface (8) for the initial condition (14), i.e. the equivalent control u_{equ} (20). From Figure 11, it can be seen the monotonous exponential decay of the switching function evolution for ETSC in agreement with the differential equation (24) within the linearity zone (34).

According to the time-optimality of the main part of the ETSC transient for $T = T_{\max}$, the switching function evolution is very similar to the TSC one, as can be seen in Figure 12. The time constant $T_{\max}$ is greater than the critical value T_{crit} (38). The consequence is that the switching function evolution curve contains a global minimum, as mentioned in Chapter 4 (see (39) and (40)). Only in the close vicinity of the zero value – within the linearity zone (34) and (35) – is the switching function behaviour of ETSC described by the reaching condition (24), the rest of the plot corresponds to the time-optimal behaviour.

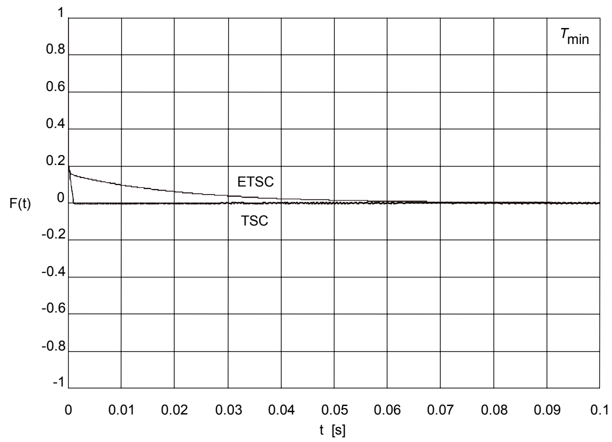

Figure 11 Switching function evolution for TSC and ETSC and for T_{min}.

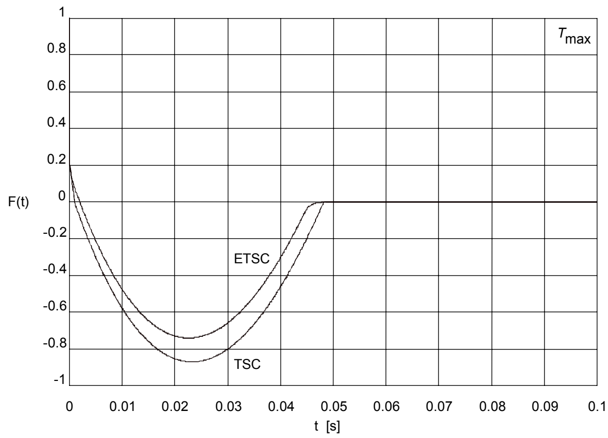

Figure 12 Switching function evolution for TSC and ETSC and for T_{max}.

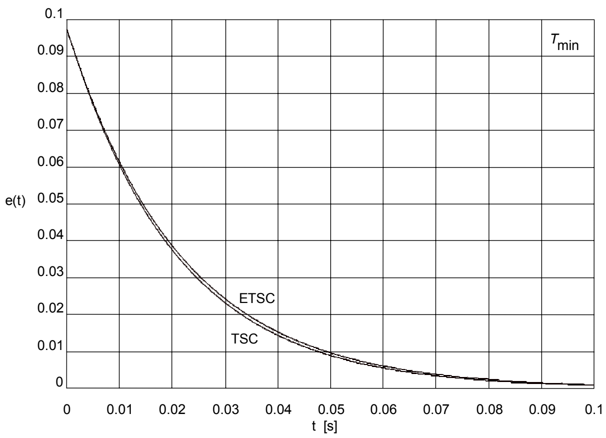

Figure 13 Rundown phase of control error for TSC and ETSC and for T_{min} in the presence of parasitic dynamics.

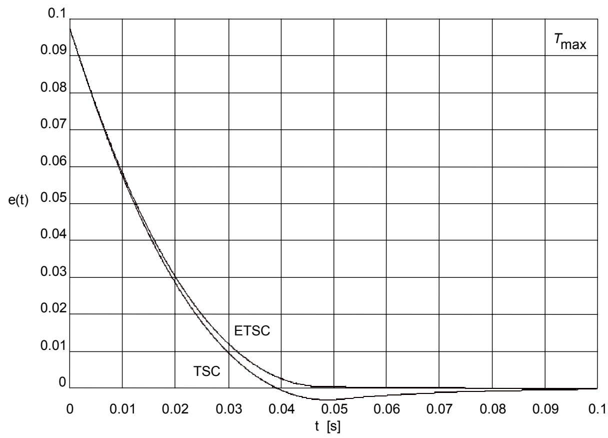

Figure 14 Rundown phase of control error for TSC and ETSC and for T_{max} in the presence of parasitic dynamics.

The robustness of the time sub-optimal type algorithms against the parasitic dynamics presence in a real plant can be seen in Figure 13 and 14 for $T_{\min}$ and $T_{\max}$ respectively. It should be reminded that the ratio of parasitic dynamics equivalent time constant T_P to plant's time constant $T_{\max}$ equals to $1:20$. Comparing Figures 13 and 5 we see that for $T = T_{\min}$ there is no difference between the quality for both TSC and ETSC with or without the parasitic dynamics presence. On the other hand, Figure 14 with $T = T_{\max}$ clearly demonstrates the advantage of the ETSC law over the TSC one. The parasitic dynamics presence results in an overshoot of the error response in TSC but no in ETSC. As for the response time, it is practically identical to that in Figure 8. It can be concluded that the proposed equivalent time sub-optimal control meets the requirement of robustness against the parametric disturbance (2) preserving the fast dynamics without both the overshoot and chattering despite the parasitic dynamics presence, as formulated in Chapter 4.

6 CONCLUSION

In this paper a chattering-free modification of time sub-optimal control has been proposed including a brief summary of the original TSC theory and the equivalent control approach. The uniqueness of the sliding mode description for the controllable canonical form has been formulated and proved in two theorems. The discontinuous sliding mode typical for variable structure systems has been replaced by a smooth equivalent control algorithm satisfying the reaching law. After a thorough discussion, the conditions for the control parameters have been determined. The efficiency of the proposed approach has been demonstrated through numerical simulation of a position control system. It has been shown that the control law is robust against parameter variations and parasitic dynamics presence. The results showed the ideal control action behaviour and consequently offered low energy consumption in comparison with the time sub-optimal control law results.

REFERENCES

[1] Bartolini G., Sanna S. and Usai E., Robust Near-Optimal Control Via Unchattering Sliding Mode Control. *American Institute of Physics (AIP) Conference Proceedings on Computing Anticipatory Systems (CASYS '97)*, Liege, Belgium, Vol. 437, pp 269-283, 1998.

[2] Bartolini G., Ferrara A., Levant A. and Usai E., On Second Order Sliding Mode Controllers. *Young K.D. and Ozguner U. (eds.): Variable Structure Systems, Sliding Mode and Nonlinear Control*, Springer Verlag, London, pp 329-350, 1999.

[3] Bartolini G., Pillosu S., Pisano A. and Usai E., Time-Optimal Stabilisation for a Third-Order Integrator: a Robust State-Feedback Implementation. *Online publ.: http://link.springer-ny.com/link/ service /series/ 0642/papers/2273/22730131.pdf*, Springer Verlag, 2002.

[4] Bartolini G., Pisano A., Punta E. and Usai E., A survey of applications of second-order sliding mode control to mechanical systems. *International Journal of Control*, Vol. 76, No. 9/10, pp 875-892, 2002.

[5] Bartoszewitz A., Discrete-time quasi-sliding-mode control strategies. *IEEE Transactions on Industrial Electronics*, Vol. 45, No. 4, pp 633-637, 1998.

[6] Fridman L. and Levant A., Higher-Order Sliding Modes. *Perquetti W. and Barbot J.P. (eds.): Sliding Mode Control in Engineering*, Marcel Dekker, New York, pp 53-101, 2002.

[7] Hung J.Y., Gao W. and Hung J.C., Variable Structure Control: A Survey. *IEEE Transactions on Industrial Electronics*, Vol. 40, No. 1, pp 2-22, 1993.

[8] Jalili N. and Olgac N., Time-optimal/sliding mode control implementation for robust tracking of uncertain flexible structures. *Mechatronics*, Vol. 8, No. 2, pp 121-142, 1998.

[9] Kachroo P., Existence of Solutions to a Class of Nonlinear Convergent Chattering-free Sliding Mode Control Systems. *IEEE Transactions on Automatic Control*, Vol. 44, No. 8, pp 1620-1624, 1999.

[10] Kardos J., Variable Structure Motion Control Systems. *Frankovic B. (editor): Trends in Control Theory and Applications*, Veda Publishing House, Bratislava, pp 132-158, 1998.

[11] Kardos J. and Kalas D., Near-to-minimum Time VSS with Application to Position Control. *Journal of Electrical Engineering*, Vol. 45, No. 12, pp 441-452, 1994.

[12] Levant A., Higher-order sliding modes, differentiation and output-feedback control. *International Journal of Control*, Vol. 76, No. 9-10, pp 924-941, 2003.

[13] Moallem M., Khorasani K. and Patel R.V., Inversion-based Sliding Control of a Flexible-link Manipulator. *International Journal of Control*, Vol. 71, No. 3, pp 477-490, 1998.

[14] Newman W.S., Robust Near Time-Optimal Control. *IEEE Transactions on Automatic Control*, Vol. 35, No. 7, pp 841-844, 1990.

[15] Salinas R., Barbieri E. and Drakunov S., Time Sub-Optimal/Sliding Mode Controller for a Flexible Structure. *Proceedings of the 28th Southeastern Symposium on System Theory (SSST'96)*, Baton Rouge, Louisiana, USA, pp 253-257, 1996.

[16] Utkin V.I., *Sliding Modes and their Applications in Variable Structure Systems*. Mir Publishers, Moscow, 1978.

[17] Utkin V.I., Guldner J. and Dhi J., *Sliding Mode Control in Electromechanical Systems*. Taylor & Francis, London, 1999.

[18] Utkin V. I., First Stage of VSS: People and Events. *Yu X. and Xu J.X. (eds.): Variable Structure Systems:*

Towards the 21st Century. Springer Verlag, Berlin, pp 1-32, 2002.

[19] Vittek J. and Dodds S.J., Analysis of Preliminary Experimental Results of a New Induction Motor Position Control System. *Proceedings of the EDPE'01 Conference on Electrical Drives and Power Electronics*, Kosice, Slovakia, pp 41-47, 2001.

[20] Young K.D., Utkin V.I. and Ozguner U., A Control Engineer's Guide to Sliding Mode Control. *IEEE Transactions on Control Systems Technology*, Vol. 7, No. 3, pp 328-342, 1999.

[21] Xu J.X. and Zhang J., On quasi-optimal variable structure control approaches. *Yu X. and Xu J.X. (eds.): Variable Structure Systems: Towards the 21st Century*, Springer Verlag, Berlin, pp 175-200, 2002.

[22] Zanasi R., Guarino Lo Bianco C. and Tonielli A., Nonlinear filters for the generation of smooth trajectories. *Automatica*, Vol. 36, No. 3, pp 439-448, 2000.

[23] Zhou J., Zhou R., Wang Y. and Guo G., Improved proximate time-optimal sliding-mode control of hard disk drives. *IEE Proceedings - Control Theory and Applications*, Vol. 148, No. 6, pp 516-522, 2001.

TEMPLATE FOR PREPARING PAPERS FOR PUBLISHING IN INTERNATIONAL JOURNAL OF MECHANICS AND CONTROL

Author1* Author2**

* affiliation Author1

** affiliation Author2

ABSTRACT

This is a brief guide to prepare papers in a better style for publishing in International Journal of Mechanics and Control (JoMaC). It gives details of the preferred style in a template format to ease paper presentation. The abstract must be able to indicate the principal authors' contribution to the argument containing the chosen method and the obtained results.

Keywords: keywords list (max 5 words)

1 TITLE OF SECTION (E.G. INTRODUCTION)

This sample article is to show you how to prepare papers in a standard style for publishing in International Journal of Mechanics and Control.
It offers you a template for paper layout, and describes points you should notice before you submit your papers.

2 PREPARATION OF PAPERS

2.1 SUBMISSION OF PAPERS

The papers should be submitted in the form of an electronic document, either in Microsoft Word format (Word'97 version or earlier).
In addition to the electronic version a hardcopy of the complete paper including diagrams with annotations must be supplied. The final format of the papers will be A4 page size with a two column layout. The text will be Times New Roman font size 10.

Contact author: author1[1], author2[2]

[1]Address of author1.

[2]Address of author2 if different from author1's address.

2.2 DETAILS OF PAPER LAYOUT

2.2.1 Style of Writing

The language is English and with UK/European spelling. The papers should be written in the third person. Related work conducted elsewhere may be criticised but not the individuals conducting the work. The paper should be comprehensible both to specialists in the appropriate field and to those with a general understanding of the subject.
Company names or advertising, direct or indirect, is not permitted and product names will only be included at the discretion of the editor. Abbreviations should be spelt out in full the first time they appear and their abbreviated form included in brackets immediately after. Words used in a special context should appear in inverted single quotation mark the first time they appear. Papers are accepted also on the basis that they may be edited for style and language.

2.2.2 Paper length

Paper length is free, but should normally not exceed 10000 words and twenty illustrations.

2.2.3 Diagrams and figures

Figures and Tables will either be entered in one column or two columns and should be 80 mm or 160 mm wide respectively. A minimum line width of 1 point is required at actual size. Captions and annotations should be in 10 point with the first letter only capitalised *at actual size* (see Figure 1 and Table VII).

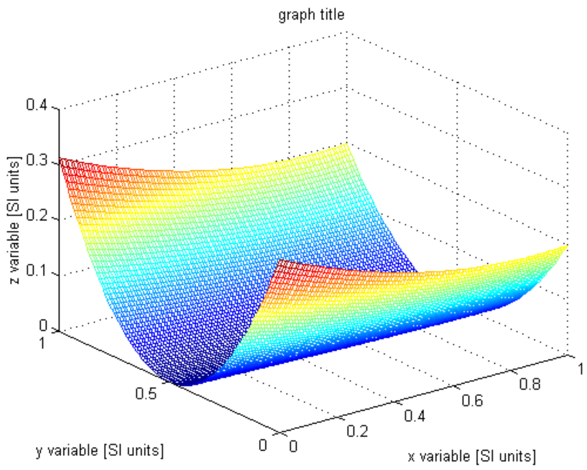

Figure 1 Simple chart.

Table VII - Experimental values

Robot Arm Velocity (rad/s)	Motor Torque (Nm)
0.123	10.123
1.456	20.234
2.789	30.345
3.012	40.456

2.2.4 Photographs and illustrations

Authors could wish to publish in full colour photographs and illustrations. Photographs and illustrations should be included in the electronic document and a copy of their original sent. Illustrations in full colour …

2.2.5 Equations

Each equation should occur on a new line with uniform spacing from adjacent text as indicated in this template. The equations, where they are referred to in the text, should be numbered sequentially and their identifier enclosed in parenthesis, right justified. The symbols, where referred to in the text, should be italicised.

- point 1
  - point 2
    - point 3

1. numbered point 1
   2. numbered point 2
      3. numbered point 3

$$W(d) = G(A_0, \sigma, d) = \frac{1}{T}\int_0^{+\infty} A_0 \cdot e^{-\frac{d^2}{2\sigma^2}} dt \qquad (1)$$

3 COPYRIGHT

Authors will be asked to sign a copyright transfer form prior to JoMaC publishing of their paper. Reproduction of any part of the publication is not allowed elsewhere without permission from JoMaC whose prior publication must be cited. The understanding is that they have been neither previously published nor submitted concurrently to any other publisher.

4 PEER REVIEW

Papers for publication in JoMaC will first undergo review by anonymous, impartial specialists in the appropriate field. Based on the comments of the referees the Editor will decide on acceptance, revision or rejection. The authors will be provided with copies of the reviewers' remarks to aid in revision and improvement where appropriate.

5 REFERENCES (DESCRIPTION)

The papers in the reference list must be cited in the text. In the text the citation should appear in square brackets [ ], as in, for example, "the red fox has been shown to jump the black cat [3] but not when...". In the Reference list the font should be Times New Roman with 10 point size. Author's first names should be terminated by a 'full stop'. The reference number should be enclosed in brackets.

The book titles should be in *italics*, followed by a 'full stop'. Proceedings or journal titles should be in *italics*. For instance:

REFERENCES (EXAMPLE)

[1] Smith J., Jones A.B. and Brown J., *The title of the book*. 1st edition, Publisher, 2001.

[2] Smith J., Jones A.B. and Brown J., The title of the paper. *Proc. of* Conference *Name*, where it took place, Vol. 1, paper number, pp. 1-11, 2001.

[3] Smith J., Jones A.B. and Brown J., The title of the paper. *Journal Name*, Vol. 1, No. 1, pp. 1-11, 2001.

[4] Smith J., Jones A.B. and Brown J., *Patent title*, U.S. Patent number, 2001.

International Journal of Mechanics and Control – JoMaC
Published by Levrotto&Bella
TRANSFER OF COPYRIGHT AGREEMENT

NOTE: Authors/copyright holders are asked to complete this form signing section A, B or C and mail it to the editor office with the manuscript or as soon afterwards as possible.	*Editor's office address:* Andrea Manuello Bertetto Elvio Bonisoli *Dept. of Mechanics* *Technical University-Politecnico di Torino* ***C.so Duca degli Abruzzi, 24. 10129 Torino – Italy*** e_mail: jomac@polito.it fax n.: +39.011.564.6999

The article title:

By:____

To be Published in ***International Journal of Mechanics and Control JoMaC***
Official legal Turin court registration Number 5320 (5 May 2000) - reg. Tribunale di Torino N. 5390 del 5 maggio 2000

A Copyright to the above article is hereby transferred to the JoMaC, effective upon acceptance for publication. However the following rights are reserved by the author(s)/copyright holder(s):
1. All proprietary rights other than copyright, such as patent rights;
2. The right to use, free or charge, all or part of this article in future works of their own, such as books and lectures;
3. The right to reproduce the article for their own purposes provided the copies are not offered for sale.

To be signed below by all authors or, if signed by only one author on behalf of all co-authors, the statement A2 below must be signed.

A1. All authors:

SIGNATURE______________________________DATE__________ SIGNATURE______________________________DATE__________

PRINTED NAME____________________________________ PRINTED NAME____________________________________

SIGNATURE______________________________DATE__________ SIGNATURE______________________________DATE__________

PRINTED NAME____________________________________ PRINTED NAME____________________________________

A2. One author on behalf of all co-authors:
"I represent and warrant that I am authorised to execute this transfer of copyright on behalf of all the authors of the article referred to above"

PRINTED NAME____________________________________

SIGNATURE______________________________ TITLE______________________________ DATE______________

B. The above article was written as part of duties as an employee or otherwise as a work made for hire. As an authorised representative of the employer or other proprietor. I hereby transfer copyright to the above article to Editel-Pozzo Gros Monti effective upon publication. However, the following rights are reserved:
1. All proprietary rights other than copyright, such as patent rights;
2. The right to use, free or charge, all or part of this article in future works of their own, such as books and lectures;
3. The right to reproduce the article for their own purposes provided the copies are not offered for sale.

PRINTED NAME____________________________________

SIGNATURE______________________________ TITLE______________________________ DATE______________

C. I certify that the above article has been written in the course of employment by the United States Government so that no copyright exists, or by the United Kingdom Government (Crown Copyright), thus there is no transfer of copyright.

PRINTED NAME____________________________________

SIGNATURE______________________________ TITLE______________________________ DATE______________

CONTENTS

next number scheduled titles:

MEMS Inertial Guidance Systems for Low Cost Vehicles
P. Maggiore, M. Velardocchia

Mathematical Model for Simulation Analysis of a Remotely-Piloted lighter-than-air Platform
M. Battipede, P. Gili, M. Lando

Design Parameters Sensitivity Analysis of a New Diesel Locomotive
P. Belforte, F. Cheli, A. Collina, L. Prone, G. Tomasini

Tribological Behaviour of the Tool-Workpiece Kinematic Pair in Machining of Impregnated Sintered Materials
P. Buonadonna, G. Dionoro

Nonlinear Elastic Characteristic of Magnetic Suspensions through Hilbert Transform
E. Bonisoli